NTNU
Norwegian University of
Science and Technology

An Experimental Study on the Wave-Induced Hydroelastic Response of a Floating Solar Island

Jonathan Winsvold

Marine Technology
Submission date: June 2018
Supervisor: Trygve Kristiansen, IMT
Co-supervisor: Odd Magnus Faltinsen, IMT

Norwegian University of Science and Technology
Department of Marine Technology

Preface

This Master's Thesis is the concluding part of my Master of Science degree in Hydrodynamics in Naval Architecture at the Department of Marine Technology (IMT) at the Norwegian University of Science and Technology (NTNU) in Trondheim, Norway. The work was carried out in the spring semester of 2018.

The Thesis investigates the hydroelastic response of a floating solar island in different sea-conditions using an experimental method. The concept of a floating solar island originated from Professor Bruce Patterson at the University of Zürich who suggested producing methanol from CO_2 in sea water using solar power. The design of the island is proposed by Professor Trygve Kristiansen at the Department of Marin Hydrodynamics, who also suggested this as a research topic.

The reader of this thesis should have some prior knowledge of naval architecture and hydrodynamics.

Trondheim, 15.06.2018

Jonathan Winsvold

Acknowledgment

First and foremost, I would like to express my sincere gratitude to my supervisor Professor Trygve Kristiansen whose unequivocal support, relentless enthusiasm and knowledgeable guidance have been essential to the success and final outcome of this master thesis. I could not have imagined having a better advisor and mentor. I would also like to thank my co-supervisor Professor Odd Magnus Faltinsen for his valuable advice, interesting conversations and important input to this work. A special thanks also to Terje Røsten and Torgeir Whal for their patient and helpful contributions during the experiment.

J.W.

Abstract

Future energy demand are expected to increase substantially in the next decades, and there is a real need to consider new ways of supplying the energy market with cost-efficient, dependable and green sources of energy. The ocean is vast and large proportions of it are continually exposed to sunlight. Floating solar islands that are capable of carrying photovoltaic solar panels in offshore sea conditions could supply solar power directly onto power grids or could be used in an electrochemical process that produces liquid methanol from CO_2 in sea water, an energy source that can be stored for later use.

A few designs of floating solar islands exists already, but none that can operate in offshore sea conditions. There are considerable challenges in designing such a structure, and this thesis investigates the potential of a large floating structure consisting of multiple slender floating tori elastically connected. For this purpose, an experimental study into the governing behavior and response of the proposed structure have been performed. The deck has been omitted, and the structure in this study consists of five elastic tori enclosing each other that are connected through trusses. The trusses are elastic, creating motions that are hard to predict but that avoids snap loads and jerky motions, and enables the structure to move with the waves.

Previous theoretical and experimental studies involving a single semi-submerged slender torus have been used as a basis for this study. A model with multiple tori and one with a single torus have therefore been built and tested in scale 1:50. The testing was conducted at the Small Towing Tank at the Centre of Marine Technology at NTNU. During the experiments the structures were moored to the walls of the tank and the wave elevation, mooring-line tensions and the vertical and horizontal responses were measured. The models were tested in regular waves with full scale wave period varying from $2.0-14s$ and wave steepness varying from $1/100-1/10$. The multi-torus was tested in irregular waves as well, with peak wave periods of $8-12s$ and significant wave heights of $2-5m$.

The experimental results from the multi-torus were compared to those from the single-torus in addition to a low-frequency linear slender-body theory for vertical radiation loads on an elastic semi-submerged torus and a zero-frequency theory. The experiments with the single-torus showed good agreement with the theoretically predicted linear responses. The experiments with the multi-torus also approximated the theoretical response for very long wave periods. However, for smaller wave periods the vertical motion was lower relative to the wave amplitude than predicted by the theoretical response for a single-torus. This was expected as a results of the trusses that are connecting the tori. The mass and added mass of each torus will affect the motion of the tori in question in addition to all the other tori. These interacting forces seems to be larger relative to the wave force for smaller waves, than when the waves are large.

Overtopping waves were identified as the main concern for the structure and the solar panels, threatening the integrity of both. Overtopping in regular waves occurred predominantly at the aft of the outermost tori for longer wave periods with relatively low wave steepness, and at the fore for high wave steepnesses and shorter wave periods. In irregular waves, overtopping waves occured at random locations on the multi-torus, with a tendency of occuring more often at the fore of the structure and on the two outer tori. However, it did not follow the pattern observed for regular waves, where there was a clear tendency for where overtopping would occur. Overtopping was registered at relatively low peak wave periods and significant wave heights compared to regular waves.

The results from the multi-torus shows potential, but more work and research are needed for further development of a functioning floating solar island.

Sammendrag

Framtidig energietterspørsel forventes å øke betraktelig de neste tiårene, og det er et reelt behov for å vurdere nye måter å forsyne energimarkedet med kostnadseffektive, pålitelige og grønne energikilder. Havet er stort og store deler av det er kontinuerlig eksponert for sollys. Flytende soløyer som er i stand til å bære fotovoltaiske solceller i offshore sjøforhold kan levere solenergi direkte til kraftnett eller kan benyttes i en elektrokjemisk prosess som produserer flytende metanol fra CO_2 i sjøvann, en energikilde som kan bli lagret for senere bruk.

Noen få modeller av flytende soløyer eksisterer allerede, men ingen som kan operere i offshore sjøforhold. Det er store utfordringer i utformingen av en slik struktur, og denne oppgaven undersøker potensialet til en stor flytende struktur som består av flere slanke flytende toruser som er elastisk knyttet sammen. Med dette som formål har det blitt utført en eksperimentell undersøkelse av den styrende bevegelsen og responsen til den foreslåtte strukturen. Dekket har vært utelatt, og strukturen i dette studiet består av fem elastiske toruser som omslutter hverandre og som er koblet sammen med tau. Tauene er elastiske, og skaper bevegelser som er vanskelig å forutsi, men som unngår snap loads og rykkete bevegelser og gjør at strukturen beveger seg med bølgene.

Tidligere teoretiske og eksperimentelle studier som involverer én enkelt semi-nedsenket slank torus har blitt brukt som grunnlag for denne studien. En modell med flere toruser og en med én enkelt torus ble derfor bygget og testet i skala 1:50. Testene ble utført i Lilletanken på Marinteknisk Senter ved NTNU. Under forsøkene ble konstruksjonene fortøyd til tankens vegger, og bølgehøyde, fortøyningsline-krefter og de vertikale og horisontale responsene ble målt. Modellene ble testet i vanlige bølger med fullskala bølgeperiode varierende fra $2,0 - 14s$ og bølgesteilhet varierende fra $1/100 - 1/10$. Multi-torusen ble også testet i uregelmessige bølger, med topp bølgeperioder på $8 - 12s$ og signifikante bølgehøyder på $2 - 5m$.

De eksperimentelle resultatene fra multi-torusen ble sammenlignet med de fra den enkle torusen, i tillegg til en lav-frekvens lineært slank-legeme teori for vertikale radiation loads på en elastisk semi-nedsenket torus, og med en null-frekvens teori. Forsøkene med singel-torusen viste tilfredstillende og sammenlignbare resultater med de teoretisk forutsette lineære responsene. Resultatene fra forsøkene med multi-torusen var også tilnærmet like den teoretiske responsen for svært lange bølgeperioder. For mindre bølgeperioder var imidlertid den vertikale bevegelsen lavere i forhold til bølgeamplituden enn antatt av den teoretiske responsen for en singel-torus. Dette var forventet som et resultat av tauene som forbinder torusene. Massen og tilleggsmassen av hver torus vil påvirke bevegelsen av både seg selv og de andre torusene. Denne kraften mellom torusene ser ut til å ha større

effekt i forhold til bølgekraften for mindre bølger, enn når bølgene er store.

Overtoppende bølger ble identifisert som hovedproblemet for strukturen og solpanelene, og kan potensielt true integriteten til begge. Overtopping i regulære bølger oppsto hovedsakelig i akter av den ytterste torusen for lengre bølgeperioder med forholdsvis lav bølgesteilhet, og i forkant av torusen for høye bølgesteilheter og kortere bølgeperioder. I irregulære bølger, oppsto overtoppende bølger på tilfeldige steder på multi-torusen, med en tendens til å forekomme oftere i forkant av strukturen og på de to ytre torusene. Det fulgte imidlertid ikke mønsteret som ble observert for regulære bølger, der det var en klar tendens til hvor overtopping ville oppstå. Overtopping ble registrert ved relativt lave topp bølgeperioder og signifikante bølgehøyder sammenlignet med regulære bølger.

Resultatene fra multi-torus viser potensiale, men mer arbeid og forskning er nødvendig for å videreutvikle designet til å bli en fungerende flytende soløy.

Nomenclature

Greek Letters

β_n	Radial Position of Accelerometer
$\ddot{\eta}_3$	Heave Acceleration [m/s^2]
δ	Deflection
$\dot{\eta}_3$	Heave Velocity [m/s]
η	Wave Elevation [m]
η_3	Heave Motion [m]
λ	Wave Length [m]
μ	Dynamic Viscosity [kg/(m$\cdot s$)]
ω	Rotational Frequency [rad/s]
ρ	Density [kg/m^3]
ρ_F	Density of full scale model
ρ_M	Density of model scale model
ζ_a	Incident Wave Amplitude [m]

Roman Letters

$\mathbf{s}_k$	Tangential unit vector of truss k
$\mathbf{x}$	End of truss-node
a_n	Accelerometer Position n [-]
a_n	Generalized coordinate of vertical motion of mode n [-]
b_n	Generalized coordinate of radial motion of mode n [-]
c	Radius of cross-section of the torus
D	Diameter
EI	Bending Stiffness [Mpa]
F	Full Scale [-]
f	Frequency [1/s]
$f_j^{(n)}$	Force acting on node
g	Gravitational Constant [m/s^2]
H	Wave Height [m]
h	Water Depth [m]

$H(\omega)$	Transfer Function
H_S	Significant Wave Height [m]
k	Wave Number [-]
$l_k^{(n)}$	Truss length
M	Model Scale [-]
m	Mass [kg]
$S(\omega)$	Power Spectral Density
$S_j(\omega)$	Power Spectral Density of the JONSWAP Spectrum
$S_{yy}(\omega)$	Power Spectral Density of Input
$S_{yy}(\omega)$	Power Spectral Density of Response
T	Wave Period [s]
T_P	Peak Wave Period [s]
w	Vertical Motion
k_s	Mooring-line Spring Stiffness
k_t	Truss Spring Stiffness

Abbreviations

2D	Two-dimensional
3D	Three-dimensional
CFD	Computational Fluid Dynamics
FFT	Fast Fourier Transform
FPS	Frames per second
LST	Low-frequency slender-body theory
RAO	Response Amplitude Operator
ZFT	Zero-frequency theory

Contents

Chapter 1

Introduction

Energy is what drives human societies forward. We, as a species, have always been limited by our physical strength when it comes to energy production, which in prehistoric times lead us to start burning wood, taming animals and building sail boats, enabling us to keep warm, produce more food and travel longer distances. Over the course of thousands of years, our rising population and ever increasing demand for necessities and luxuries have lead us to start burning oil, taming rivers and building nuclear power plants instead.

The *International Energy Outlook 2017* (IEO2017) published by the *U.S. Energy Information Administration* EIA (2017) projects that the world energy consumption will rise from 19.2 TW in 2015 to 24.6 TW in 2040, a total increase of 28%. The Three Gorges Dam in China, the world's largest dam, produced 0.011 TW in 2017 GBtimes (2017), and the nuclear power plant with the highest energy production in the world, Bruce in Canada, produced 0.0054 TW in 2015 BPS (2017). To put this projected increase in energy consumption in perspective, a new dam of this size would have to be opened every 19 days, or a nuclear power plant of this capacity built every 9 days until 2040 to keep up with the world's energy needs.

There is a growing international consensus that it is not possible to satisfy this growing appetite for energy through traditional energy sources alone. There are not enough oil, gas, rivers, or uranium on earth to meet the demand in the future, and perhaps more importantly, it would not be possible without wreaking havoc on the planet and its inhabitants, including ourselves. In other words, it is necessary, and desirable, to consider other energy sources.

1.1 Solar Energy

By 2050 renewable energy is predicted to make up nearly half of global energy supply DNVGL (2017). In 2016, renewable energy accounted for two-thirds of new power added to the world's power grids, with solar power being the fastest-growing source of new energy, even overtaking the net growth of coal, previously the biggest new source of power generation IEA (2017). The cost of solar power are set to decrease by 18% per the doubling of capacity and the current energy efficiency of the photovoltaic cells is at around 22% DNVGL (2017) and is expected to keep rising. This indicates a future where solar power is going to take a prominent place as a source of energy.

Figure 1.1: Example of Photovoltaic (PV) panels.

The promising aspects of solar power; predictability, limitlessness, cost and relative ease by which solar energy can be harvested, makes this power source highly competitive with the other energy sources, but there are still considerable challenges that needs to be overcome for it to take the role as the foremost power source in human society, the biggest of which are storage and distribution of the energy produced. Fossil fuels have high energy density, are easy to store, can be transported long distances efficiently, can be utilized for all purposes, are relatively safe, predictable and most importantly, cheap. There are, as of now, no other energy source which can compete with fossil fuels when it comes to versatility, safety and cost. However, technological advances may hold the key to unlocking the potential of renewable energy sources and dethrone fossil fuels as the king of energy.

1.2 PV panels, electrochemical storage and methanol

Photovoltaic cells produce electricity, a power source that traditionally have been supplied directly to a power grid and through that transferred to wherever it is needed. There are several ways of storing electrical power for later use, the main alternatives include mechanical storage and electrochemical storage, where the latter includes batteries which has been the most prevalent solution of storage up until now. The problems with storing electrical power in batteries are the limitations of battery capacity compared to their size and weight, the recharge time, ageing and cost. These limitations make batteries unsuitable as an energy source when large amounts of energy are needed or when reliability is important. This means that current batteries are unable to become a real alternative to liquid carbon-based energy carriers, especially when it comes to the ship and airplane industries.

An alternative to batteries is to use electricity to drive an electrochemical process of creating liquid methanol, which can be utilized as an energy source at convenience and can be implemented in current infrastructure as an alternative to fossil fuels. Methanol fuel is comparable to diesel fuel, but with half the energy density. In order to keep the production of methanol CO_2-neutral it has been suggested to create methanol from the CO_2 contained in ocean water. This technology is already in place for creating methanol from CO_2 in air, but as the concentration of CO_2 is 120 times higher in water, the potential for large scale production is much larger using the ocean. However, this chemical process would require large amounts of energy, preferably harnessed cheaply in the ocean which will be the source of the CO_2. A solution can be to generate power with floating islands of photovoltaic systems that transforms the sun's energy into electricity, which then gets stored as methanol, available for usage at any time.

1.3 Floating Solar Islands

In this regard, it has been suggested that the photovoltaic systems must float above water far offshore, where the currents create a steady supply of CO_2. Such a structure must therefore withstand certain oceanic conditions, including strong winds, waves and currents. At the same time, this construction would need to be practical and affordable to make the methanol production competitive with the rest of the market. One type of a large stable platform that has been proposed is a marine structure, consisting of concentric elastic floating tori supporting a membrane type of deck to support the solar panels. A torus is a doughnut-shaped surface generated by a circle rotated about an axis in its plane that does not intersect the circle, tori is the plural form of torus and concentric means that they have a common center Merriam-Webster. A multitude of these platform can then be connected to create an array of solar islands moored together that would occupy much less space than an offshore wind park, as seen in Figure 1.2. Placing the PV panels on water will also increase the power generated, as light reflecting from the ocean will increase the amount of light hitting the PV panels, it will also simplify any rotation of the structure with the sun's azimuth, increasing the efficiency of the PV panels. In addition, the potential of such a structure is not only limited to the creation of methanol far offshore, but can be positioned in close proximity to over-crowded cities supplying electricity through traditional cables, or function as recharge stations for electrically driven ships.

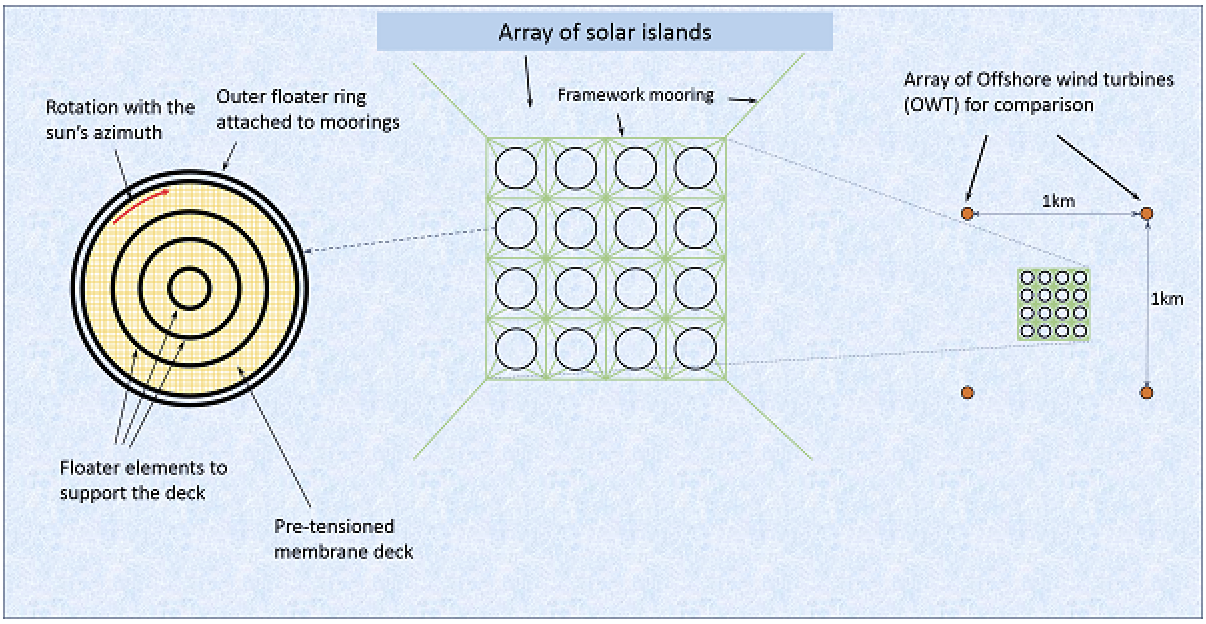

Figure 1.2: Depiction of the floating solar island concept. The illustration to the left shows the proposed design of a multi-torus, where multiple slender tori supports a membrane deck. The middle illustration shows a potential mooring-arrangement of an array of floating solar islands. The illustration to the right shows the area occupied by an array of solar islands compared to the area occupied by four offshore wind turbines, approximately producing the same amount of energy.

1.4 Challenges

Challenges related to designing a floating solar platform can mostly be attributed to wave loads and their effect on the structure. In order to build a reliable platform capable of withstanding realistic wave conditions, the different effects of waves on mooring-lines and the general motion of the structure needs to be investigated. As the platform is large, it is desirable that the structure moves flexibly in motion with the waves rather than working against them as this will alleviate the forces acting on the structure. In order to achieve this, it is important to consider the elasticity of the rings, how they are connected to one another and how they are moored in the sea. If mooring-lines are exposed to large forces they may break, therefore it is important that they are flexible with relatively low stiffness, enabling the structure to move in phase with the waves, but at the same time avoiding strong resonance.

Overtopping is also a considerable challenge, if parts of the structure is unable to move in phase with larger waves they might become submerged or waves can crash over the deck, exposing the area to large forces for short periods of time, potentially causing large amounts of damage to both the structure but also the PV panels on deck. A platform consisting of several concentric rings carrying a deck means that parts of the structure is out of water and that parts of the structure will potentially be lifted out of water during certain wave conditions. The air-pockets between the deck and the ocean surface and parts being lifted out of water can lead to the structure and waves slamming in to one another, an effect knows as slamming. This can lead to fatigue damage and potentially cause fracture of the deck, rings or PV panels. The number of suitable locations for a floating platform will increase if it can withstand larger wave forces, thus the design of the platform must be tested in a wide range of waves to find potential limits of the structure. Figure 1.3 shows the wide range of potential locations for a floating solar island if it is able to withstand 100 year significant wave height $< 7m$, and that satisfies other criteria, such as water depth $< 600m$, enough exposure to sunlight and no tropical storms.

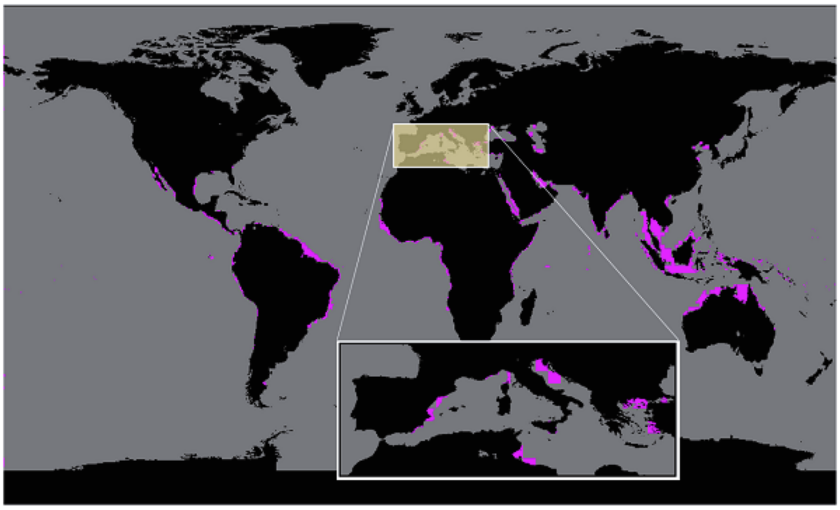

Figure 1.3: Illustration of potential locations of floating solar islands that is exposed to enough sunlight, where there are no tropical storms, with 100 year significant wave height $< 7m$ and a water depth $< 600m$

1.5 Previous studies on tori and Solar Islands

There are a number of studies on floating tori and their motions in different wave conditions, and most of them are concerned with a semi-submerged single slender torus. A broad description of the main studies and theories is presented to give an overview over the development on this topic and the background for the present study.

Newman (1977) investigated the motions of a floating slender torus in incident waves by using slender-body theory for the case where the incident wavelength is comparable to the radius of the body section and small compared with the larger radius of the torus. He also used matched asymptotic expansion between a far field and near field description of the torus, and he used it to describe the oscillating motions in heave, surge and pitch.

Faltinsen (2011) considered the hydroelasticity of a single torus and derived a slender-body theory by using the limiting case where the forcing frequency $\omega \to 0$ based on a rigid free-surface condition. In order to take 3D effects into account, he also used asymptotic matching between a far field and near field description of the torus.

Li and Faltinsen (2012) derived a low-frequency slender-body theory for the vertical added mass, damping and wave excitation loads on an elastic semi-submerged single torus by matched asymptotic expansions with a near-field and far-field solution. This was valid for the classical free-surface condition. The results showed that 3D effects caused important frequency-dependent hydrodynamic interaction on the scale of the torus diameter, and the limitations of a strip-theory approach to wave-induced loads on tori.

Li et al. (2014) used numerical simulations and experiments on a moored elastic single torus in regular deep-water waves of different steepnesses and periods without current to measure the vertical accelerations in different conditions. From their comparison against the measurements, a strong 3D and frequency dependency effects as well as flexible floater motions was shown to matter.

Li (2017) described and compared the low-frequency linear slender-body theory for vertical radiation loads on an elastic semi-submerged torus based on matched asymptotic expansions with results from WAMIT. He found reasonable agreement between experiments and theoretically predicted linear response, but the agreement between numerical methods and experiments were generally deemed unsatisfactory for the nonlinear response.

Borvik (2017) investigated the dynamical behavior of a floating solar island in waves and currents. The solar island consisted of a torus covered with a membrane posing as a deck that was upheld by applying air-pressure between the deck and the water, creating an uplifting force. This solution was found to be unsuitable for its purpose, and he recommended investigating other ways of carrying the weight of a deck of solar panels. This suggestion lead to the present study with multiple tori supporting the deck.

1.6 Objective and Scope

This master thesis explores the governing hydroelastic response of a structure consisting of five elastic concentric circular cylinders attached to each another by flexible ropes in different wave conditions, including both regular and irregular waves. Hydroelasticity is a term that describes the mutual interaction between inertial, hydrodynamic and elastic forces Heller and Abramson (1959) and Bishop et al. (1979). The proposed structure will in this study be referred to as a *multi-torus*, compared to a single elastic concentric cylinder that will be referred to as a *single-torus*. Due to the many studies on the response of a single-torus, it has also been a goal in this study to understand how results and theory for a single-torus compares to the behavior of a multi-torus, and to identify the main challenges such a structure will face in different wave conditions. The vertical and the horizontal RAO in different modes will be investigated, in addition to the forces acting in the mooring-lines. Both accelerometers and a motion capture system will be used to measure the vertical motions of the multi-torus. A motion capture system have not been used to measure the response of a structure in the Small Towing Tank before. Thus, the results from these will be compared to find the advantages and limitations of using a motion capture system for experiments on a floating solar island. The work is a continuation of a preliminary study performed from August to December 2017. The main objectives of this Master's thesis can be summarized as:

1. Design and build a physical model of a multi-torus and a single-torus that withstands offshore-conditions
2. Perform an experimental study on a model of a single-torus and a multi-torus in regular and irregular waves whilst measuring important structure-wave interactions.
3. Investigate the potential for overtopping
4. Compare results between the two different models, and compare this to existing theory for slender circular cylinder structures in waves.
5. Compare results from accelerometers and a motion capture system.
6. Further analyze the results in order to identify and discuss the governing behaviour of the structure in different wave-conditions.

1.7 Outline of Master Thesis

Chapter 2 describes the main theories and equations regarding regular waves, irregular waves, , response-theory, modal analysis, truss-forces and overtopping.

Chapter 3 outlines the experiments with the models in the wave tank and the methods used to acquire the relevant data.

Chapter 4 presents and discusses the results from the experiment with regular waves and compares it with theory described in *Chapter* 2 and *Appendix* A.

Chapter 5 presents and discusses the results from the experiment with irregular waves and compares it with theory described in *Chapter* 2.

Chapter 6 draws conclusions from the study and gives suggestions for further work and research topics.

Chapter 2

Theory

This chapter presents the general theories and assumptions utilized for performing the study on the multi-torus. They have all been derived by others, and have been essential to the different stages of the experiment.

2.1 Regular Waves

When describing wave-induced motions and loads on floating structures, it will often suffice to utilize linear theory Faltinsen (1993). Since it is possible to obtain results in irregular seas by linearly superposing results from regular wave components, it is also sufficient from a hydrodynamical point of view to analyze a structure in incident regular sinusoidal waves of small wave steepness. In severe sea states, non-linear effects becomes important, but as this study considers non-breaking regular waves of relatively low wave steepness, linear theory will be utilized for parts of the study. For a multi-torus structure in incident regular waves of amplitude ζ_a, where the wave steepness is small, linear theory means that the wave-induced motion and load amplitudes are linearly proportional to ζ_a. Also, a steady state condition is assumed, which means that there are no transient effects present due to initial conditions. It implies that the linear dynamic motions and loads on the structure are harmonically oscillating with the same frequency as the wave loads that excite the structure.

Figure 2.1 illustrates the shape and main parameters of a regular sinusoidal wave, where $T = 2\pi/\omega$ is the time dependent wave period, $\lambda = 2\pi/k$ is the time dependent wavelength, H is the wave height, and H/λ is the wave steepness.

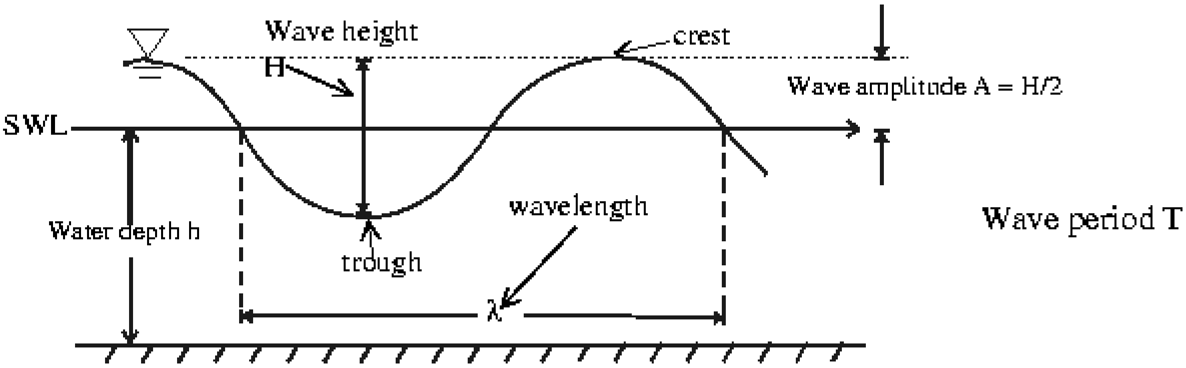

Figure 2.1: Illustration of the shape and main parameters of a regular sinusoidal wave. T is the wave period, H is the wave height, λ is the wavelength and H/λ is the wave steepness.

2.1.1 Experimental RAO for Regular Waves

Based on the aforementioned assumption it is possible to use regular wave tests to acquire the RAOs (Response Amplitude Operators) of motions and loads. The waves generated must then be close to sinusoidal and at the same time stable and stationary for a long enough time to obtain steady-state structure motions. The RAO is defined as the ratio between the fundamental component of the measured response amplitude $a_{n,a}$ and the input wave amplitude ζ_a, $RAO = |a_{n,a}/\zeta_a|$ Steen and Aarsnes (2014).

2.1.2 Theoretical RAO for Regular Waves

Two possible ways to model the theoretical RAO in regular waves for a single-torus are both briefly presented in this section. They were used as a basis of comparison for the experimental results and to investigate how well they predicted the motions of a multi-torus. The limitations of the RAO derived from what is referred to as the *Zero-frequency theory* (ZFT) in this study, meant that it was only once to compare it to the more accurate *Low-frequency slender-body theory* (LST) to emphasize the difference between the two.

Zero-frequency theory

The wave-induced vertical motion of an elastic torus can be derived for the limiting case where $\omega \to 0$ and the rigid free surface condition is used Faltinsen (2011). The resulting RAO in heave, i.e. the mode $n = 0$, is described in the following equation

$$\left|\frac{a_{0,a}}{\zeta_a}\right| = \left|\frac{\rho g b_w - \omega^2 a_{33}^{(0)}}{\rho g b_w - \omega^2 \left(m + a_{33}^{(0)}\right) - i\omega b_{33}^{(0)}} i J_0(kR)\right| \tag{2.1}$$

The RAO for the other modes, where $n = 1$ is pitch, $n = 2$ is the first flexible mode and $n = 3$ is the second flexible mode, can be found by

$$\left|\frac{a_{n,a}}{\zeta_a}\right| = \left|\frac{\rho g b_w - \omega^2 a_{33}^{(n)}}{\rho g b_w + \frac{n^4}{R^4} EI - \omega^2 \left(m + a_{33}^{(n)}\right) - i\omega b_{33}^{(n)}} 2 i J_n(kR)\right| \tag{2.2}$$

Low-frequency slender-body theory

A frequency dependent study on the vertical motion of an elastic torus is described in Li and Faltinsen (2012) and Li (2017). This theoretical model have been utilized substantially in this study, and therefore a comprehensive description of it is included in Appendix A. There, the different terms and variables included in both the Zero-frequency theory and the Low-frequency slender-body theory are derived and explained. The RAO in heave is found from

$$\left|\frac{a_{0,a}}{\zeta_a}\right| = \left|\frac{\left[\left(1 - \frac{\pi k c}{4}\right) \rho g b_w - \left(\omega^2 a_{33}^{(0)} + i\omega b_{33}^{(0)}\right) \exp(k z_m\right] i J_0(kR) + T_A}{-\omega^2 \left(m + a_{33}^{(0)}\right) - i\omega b_{33}^{(0)} + \rho g b_w}\right| \tag{2.3}$$

and the RAO for the other modes can be found using the following expression

$$\left|\frac{a_{n,a}}{\zeta_a}\right| = \left|\frac{\left[\left(1 - \frac{\pi k c}{4}\right) \rho g b_w - \left(\omega^2 a_{33}^{(n)} + i\omega b_{33}^{(n)}\right) \exp(k z_m\right] 2 i^{n+1} J_n(kR) + T_B}{-\omega^2 \left(m + a_{33}^{(n)}\right) - i\omega b_{33}^{(n)} + \rho g b_w + \frac{EI}{R^4}(n^4 - n^2 + T_C}\right| \tag{2.4}$$

2.2 Irregular Waves

This section is based on Faltinsen (1993) and is meant to give a brief overview over why and how the response are tested in irregular waves. Results from irregular waves give a close approximation to the results in realistic sea states. These results can be obtained by adding together results from regular waves of different amplitudes, wavelengths and propagation directions. By representing a time domain solution of the waves in the frequency domain, the sea spectrum $S(\omega)$ can be used to describe an irregular sea. This can be modelled as a summation of sinusoidal wave components, where the simplest random wave model is the linear long-crested wave model given by

$$\zeta = \sum_{j=1}^{N} A_j \ sin(\omega_j t + \epsilon_j) \tag{2.5}$$

Here A_j is the wave amplitude and ϵ_j is the random phase angle, and where

$$\frac{1}{2} A_j^2 = S(\omega_j)\Delta\omega \tag{2.6}$$

The response to each wave component in 2.5 can be analyzed separately because of linearity. This can thus be used for studying and representing the actual responses in the frequency domain, including non-linear phenomena as high frequency and low frequency responses, impact loads and survivability in extreme sea states. However, to produce realistic wave frequency responses during model-testing, the energy spectrum of the input waves have to be accurate Steen and Aarsnes (2014). To check if the generated input waves are comparable to realistic sea conditions, the spectral density of the input wave field can be compared to the JONSWAP spectrum. The JONSWAP wave spectrum $S_j(\omega)$ gives a theoretical description of irregular waves and can be applied for fully developed, fetch limited wind seas, and is thus able to describe wind sea conditions that often occur for the most severe sea states DNV (2011). This was used to check the experimental irregular sea states, and the formula can be found in Appendix B

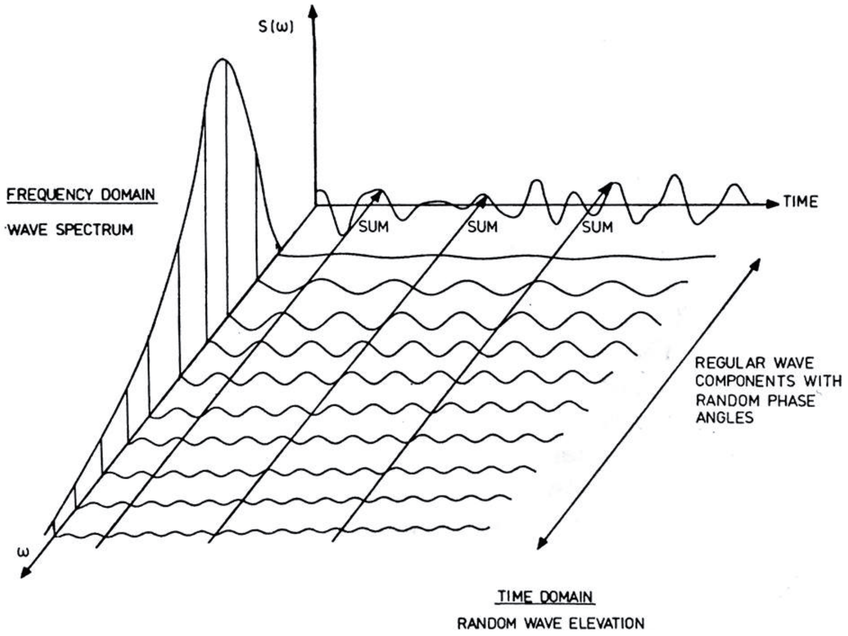

Figure 2.2: Connection between a frequency domain and time domain for waves in a long-crested short term sea state Faltinsen (1993).

2.2.1 Response Amplitude Operator for Irregular Waves

In irregular waves, the transfer function $H(\omega)$ is the equivalence to RAO in regular waves Steen and Aarsnes (2014). The measured response spectrum $S_{yy}(\omega)$ is divided by the input wave spectrum $S_{xx}(\omega)$, both of which are found through spectral analysis, and the transfer function is thus found by

$$|H(\omega)|^2 = \frac{S_{yy}}{S_{xx}} \tag{2.7}$$

2.3 Modal Analysis

The experimental wave-induced elastic response of a torus is found through modal analysis. The total periodic response of the torus are determined by superposition of the response from single points distributed over the torus. Figure 2.3 shows a single-torus where a_n for $n = 1, 2, .., 8$ are the positions of the accelerometers used to measure the local position, and β_n for $n = 1, 2, ..., 8$ gives the radial fixed position of the corresponding accelerometers on the torus.

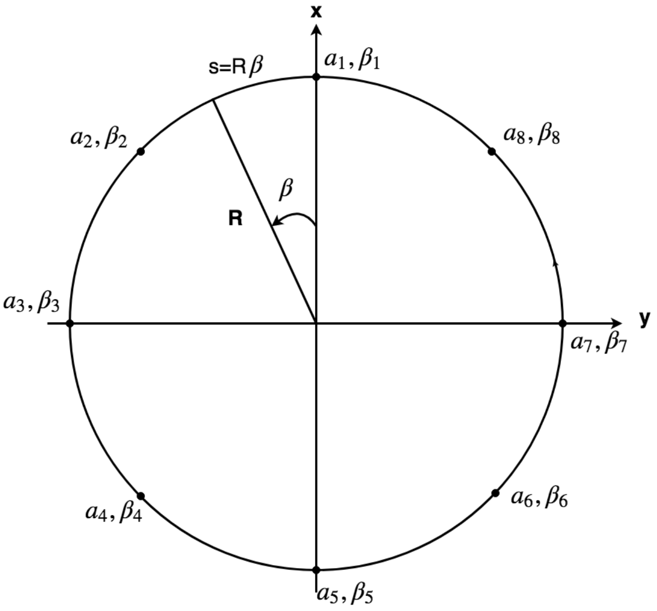

Figure 2.3: Accelerometers a_n and their corresponding radial position β_n, for n=1,2,..8. R is the radius from the center of the torus to the centerline of the torus.

The accelerations $a_n^{exp}(t)$ measured at each point are differentiated to find the vertical motion $w_n^{exp}(t)$. The response is assumed symmetric about the x-axis for waves propagating in the negative x-direction, thus the measured motion w_n^{exp} can be expressed as a

Fourier Series on the following form

$$
\begin{aligned}
w_1^{exp}(t) &= \sum_{n=0}^{N} b_n(t)cos(n\beta_1) = b_0 + b_1cos(\beta_1) + b_2cos(2\beta_1) + b_3cos(3\beta_1)\\
w_2^{exp}(t) &= \sum_{n=0}^{N} b_n(t)cos(n\beta_2) = b_0 + b_1cos(\beta_2) + b_2cos(2\beta_2) + b_3cos(3\beta_1)\\
&\vdots\\
w_8^{exp}(t) &= \sum_{n=0}^{N} b_n(t)cos(n\beta_8) = b_0 + b_1cos(\beta_8) + b_2cos(2\beta_8) + b_3cos(3\beta_1)
\end{aligned}
\tag{2.8}
$$

Here, $cos(n\beta)$ is the mode n. Superposition of eight points makes it possible to calculate the four first modes of the torus, where $n = 0$ is in the heave direction, $n = 1$ is in the the pitch direction and $n = 2$ and $n = 3$ are the first and second flexible modes respectively. Figure 2.4 illustrates how the motions of the center line of the torus for the different modes.

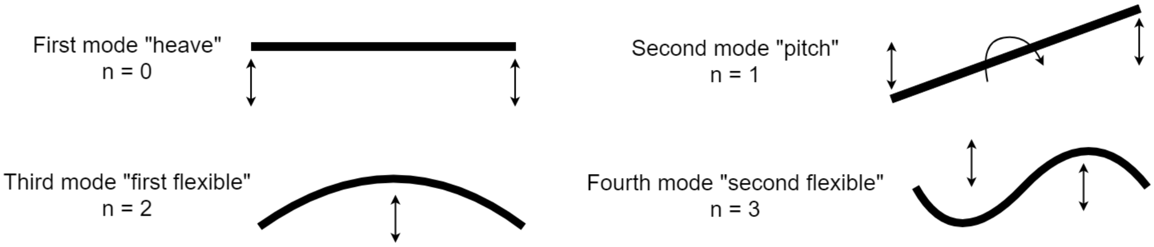

Figure 2.4: Modes

To find the equation of motion for each mode amplitude $b_n(t)$, the following system of equations are used

$$
\underbrace{\begin{bmatrix} 1 & cos(\beta_1) & cos(2\beta_1) & cos(3\beta_1)\\ 1 & cos(\beta_2) & cos(2\beta_2) & cos(3\beta_2)\\ \vdots & \vdots & \vdots & \vdots\\ 1 & cos(\beta_8) & cos(2\beta_8) & cos(3\beta_8) \end{bmatrix}}_{A}
\underbrace{\begin{bmatrix} b_0(t)\\ b_1(t)\\ b_2(t)\\ b_3(t) \end{bmatrix}}_{b}
=
\underbrace{\begin{bmatrix} w_1^{exp}(t)\\ w_2^{exp}(t)\\ \\ w_8^{exp}(t) \end{bmatrix}}_{a}
\tag{2.9}
$$

from which the response for the different modes $\mathbf{b}(t)$ can be found by the least squares method

$$\mathbf{b}(t) = [(\mathbf{A}^T\mathbf{A})^{-1}\mathbf{A}^T]\mathbf{w}(t) \tag{2.10}$$

2.4 Overtopping

Wave overtopping occurs when a wave hits the top of the torus, and is a nonlinear phenomenon not described by linear potential flow theory Faltinsen et al. (2004) and Kristiansen (2010). This can significantly influence the vertical forces and the relative motions of the torus and the waves, and can lead to viscous flow separation. Figure 2.5 shows how overtopping over a cross-section of the torus looks.

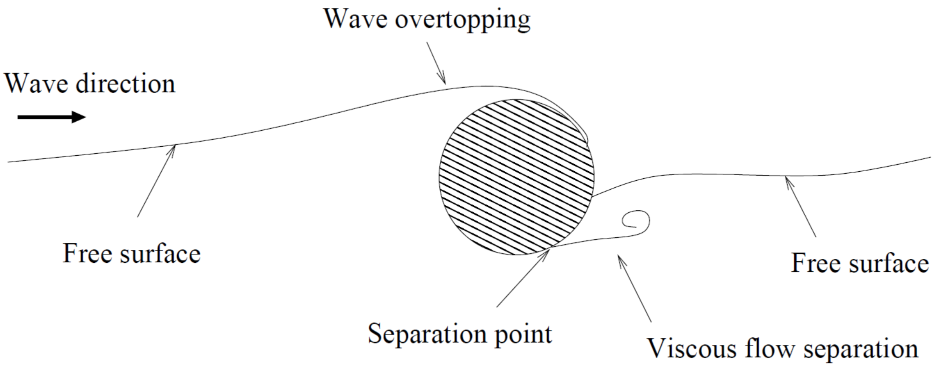

Figure 2.5: Cross-section of torus during overtopping Kristiansen (2010).

Overtopping occuring between the tori will strike the deck from below and potentially cause serious damage to the integrity of the structure or damage any solar panels. If waves are overtopping on the sides of the tori, the deck will become subjected to large wave forces and be partly submerged for a period of time, also possibly damaging both the structure and the solar panels. Overtopping is considered as the main concern of the multi-torus, as its freeboard is quite low. It is therefore desirable that the structure is relatively flexible and that it moves in motion with the waves.

2.5 Truss model

This section briefly presents a possible way to model the behavior of the trusses between the tori of the structure and the mooring-lines. The theory was originally presented by Marichal (2003), and then developed by Kristiansen and Faltinsen (2015). In the latter paper, the truss model and theory for the floater was implemented in an integrated manner. This means that the solver was implicit, such that the motions for both the floater and trusses were solved for simultaneously. A different approach could have been to solve iteratively for the floater and the trusses, but that is in general not desirable due to inherent numerical instabilities. Only a few details are provided in the paper, and since the truss model was not implemented in the present study, only an outline of the procedure is presented here. Figure 2.6 shows an example on a possible distribution of truss-nodes on a multi-tori consisting of three tori.

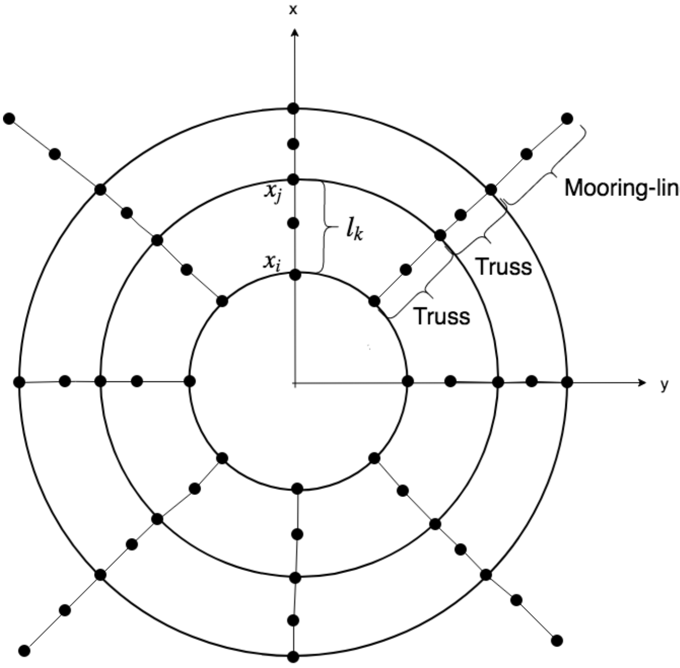

Figure 2.6: Example of how truss-nodes and mooring-line-nodes can be distributed on a multi-tori consisting of three tori. The black dots are the position of the truss-nodes, x_j and x_i are the end-nodes of a truss and l_k is the constant length of a truss.

First, the hydrodynamic forces acting on the floater are calculated followed by solving a linear system of equations for the tensions in all the trusses and the mooring-lines. Having obtained the tensions, the positions of the truss-nodes, mooring-line nodes and floater nodes are time-stepped according to Newton's second law, using a lumped-mass approach for the truss-nodes. The trusses are assumed inelastic but it is possible to include elasticity, as seen in Marichal (2003). The length of the trusses must be constant, which can be expressed as

$$l_k^{(n)} = l_k^{(n+1)} \tag{2.11}$$

where l is the truss length, n is the time-step number and k is the truss-number. The ends of the trusses are given by the nodes $\mathbf{x}_i$ and $\mathbf{x}_j$, such that $l_k^n = |\mathbf{x}_j^n - \mathbf{x}_i^n|$, where i and j refers to nodes. Then, a first-order time marching scheme is used to evolve the nodes according to Newton's second law

$$\mathbf{x}_j^{(n+1)} \; = \; \mathbf{x}_j^{(n)} + \Delta t \mathbf{u}_j^{(n)}, \; \mathbf{u}_j^{(n+1)} \; = \; \mathbf{u}_j^{(n)} + \Delta t \mathbf{a}_j^{(n)} \tag{2.12}$$

where

$$M_j \mathbf{a}_j^{(n)} = \mathbf{f}_j^{(n)} \tag{2.13}$$

Here, Δt is time step size, and $\mathbf{u}_j$ and $\mathbf{a}_j$ are the three-dimensional velocity and acceleration vectors of the floater, respectively. M_j is the mass and added mass of the tori surrounding the node. $\mathbf{f}_j^n$ is the force that acts on the node, and consists of the tensions in the trusses connected in the node, and the hydrodynamic forces acting on the tori surrounding the node. Inserting Equation 2.12 and 2.13 into 2.11 yields an equation which is nonlinear in $\mathbf{a}_j^n$, and therefore also in the tension T. The nonlinear higher order terms can be neglected as they are of the order $(\Delta)^3$, and the following expression is obtained

$$\mathbf{s}_k \cdot \left(\mathbf{a}_j^{(n)} - \mathbf{a}_i^{(n)}\right) \;=\; -\frac{1}{2l_k}|\mathbf{u}_j^{(n)} - \mathbf{u}_i^{(n)}|^2 \;-\frac{1}{\Delta t}\mathbf{s}_k \cdot \left(\mathbf{u}_j^{(n)} - \mathbf{u}_i^{(n)}\right) \tag{2.14}$$

$\mathbf{s}_k = \left(\mathbf{x}_j^{(n)} - \mathbf{x}_i^{(n)}\right)/l_k$ is the tangential unit vector of truss number k. On the left hand side the accelerations are substituted with the forces according to 2.13. On the right hand side are the known, pre-calculated hydrodynamic forces, while the unknown tensions are kept on the left hand side. With N trusses, and as each truss provides an equation, a $N \times N$ system of equations $Ax = b$, for the unknown tensions is obtained,. Solving this, yields the node positions according to 2.12 and 2.13. Modelling the mooring-lines as trusses, the same procedure can be applied. The accelerations $\mathbf{a}_j^n$, are given by the equation of motion for the multi-torus, and all parts of the system is solved for simultaneously. This gives a strong coupling between the tori, the trusses and moorings.

Chapter 3

Model Tests

The purpose of testing a model of the suggested structure was to acquire reliable data to be examined and compared in order to gain a understanding of the structures hydrodynamical properties in different sea-states. The models were tested in the Small Towing Tank at the Norwegian University of Science and Technology, in Trondheim, Norway in February and March of 2018. A single-torus model was tested in regular waves and a multi-torus model was tested in both regular and irregular waves. The only environmental loads applied on the models were those from waves generated by a wave-maker and those from four springs acting as mooring-lines evenly attached to the outer-most torus of the structure. Forces acting on the mooring-lines, wave-elevation, accelerations of the structure in response to the waves and the over-all movement of it were measured and post-processed. This chapter presents a description of how experimental results from a model test can be utilized to predict behavior of a full scale structure, the design and dimensions of the models, the test setup, the test conditions and the post-processing of the data.

3.1 Modelling and Scaling Laws

The data acquired from the model testing are transmissible to full-scale structures by utilizing a set of scaling-laws when designing the model and setting up the test-conditions. According to Steen and Aarsnes (2014), the similarity in forces can be achieved by applying these three conditions:

- GEOMETRICAL SIMILARITY: The model and the full-scale must have the same shape where all the length dimensions must have the same scale ratio $\lambda = L_F/L_M$.
- KINEMATIC SIMILARITY: The velocities and accelerations have to be equal for model and full-scale for both the structure and the flow acting on it.

- DYNAMIC SIMILARITY: The relative ratios of the different force components out of the total force are the same for full-scale and model-scale.

As it is difficult to satisfy all these conditions during model testing, Froude-scaling can be applied to ensure similarity between inertia forces and gravity forces for the different scales, and as surface waves are gravity driven, this will ensure that wave resistance and other wave-forces are correctly scaled. Froude-scaled parameters utilized for the model testing can be seen in table 3.1

Table 3.1: Froude-scaled parameters where $\lambda = L_F/L_M$, and ρ_F and ρ_M are the fluid density for the full scale and model scale structure, respectively.

Physical Parameter	Unit	Multiplication Factor
Length	[m]	λ
Structural Mass	[kg]	$\lambda^3 \cdot \rho_F/\rho_M$
Force	[N]	$\lambda^3 \cdot \rho_F/\rho_M$
Moment	[Nm]	$\lambda^4 \cdot \rho_F/\rho_M$
Acceleration	[m/s^2]	a$_F = a_M$
Time	[s]	$\sqrt{\lambda}$
Pressure	[Pa=n/m^2]	$\lambda \cdot \rho_F/\rho_M$

3.2 The Models

The single-torus and the multi-torus were built in scale 1 : 50 and scaling of all dimensions were done according to Froude-scaling. Figure 3.1 shows the two models fully instrumented in the towing tank. The coordinate system used for the models, is the same as previously seen in Figure 2.3. The fore of the models are at $\beta = 0^o$ and the aft is at $\beta = 180^o$.

The tori are made of corrugated tubes with water-repellent tape wrapped around to increase the bending stiffness of the tubes and to make them smoother, see Figure 3.2.

The bending stiffness EI of a torus was found by using cantilever beam theory, where a force F_c was applied at the end of torus-section of length L_c and the resulting deflection δ_c was measured. The bending stiffness was then calculated from

$$EI = \frac{F_c L_c^3}{3\delta_c} \tag{3.1}$$

The trusses consists of a rubber core with polyester silk enclosing them. The elongation relative to the force on the trusses were small and were therefore assumed linear for simplicity, meaning that they can be modelled as springs with a constant spring stiffness. The mooring-line spring and truss spring stiffness were found by applying a force F to a

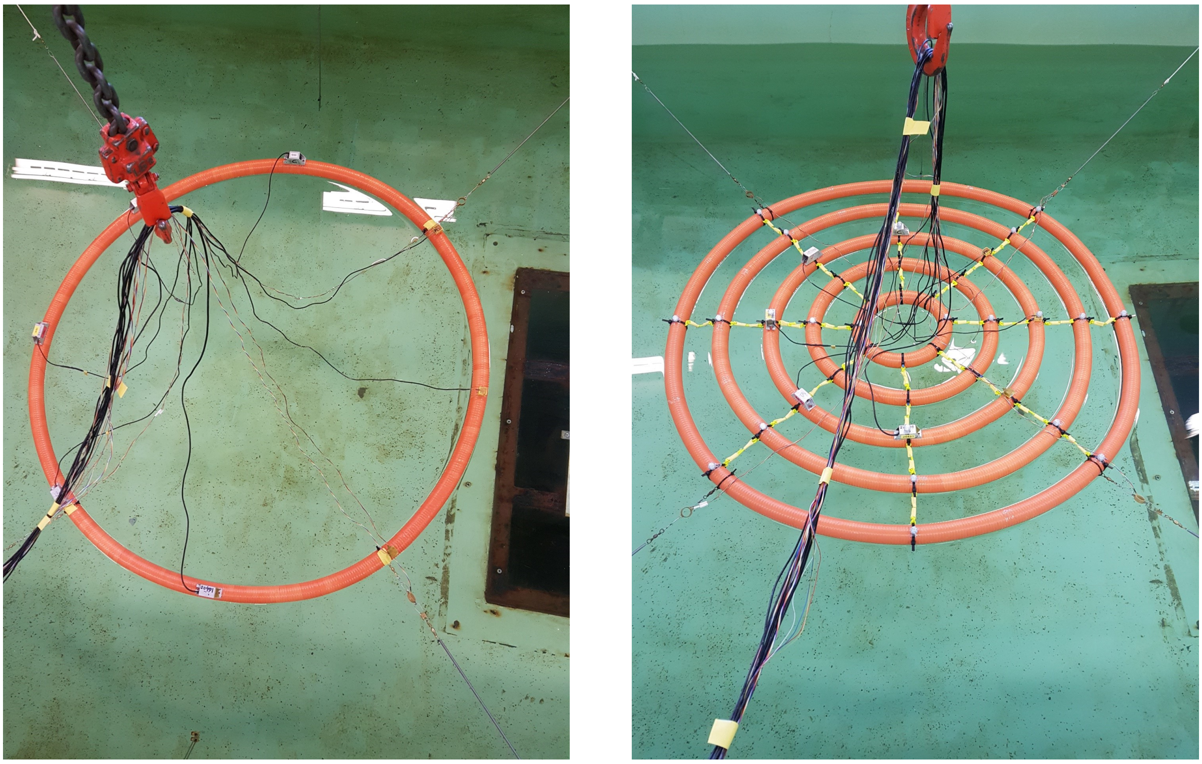

Figure 3.1: two different models tested, with instrumentation and mooring lines.

Table 3.2: Main parameters of both models and the corresponding full scale structure.

Description	Parameter	Model scale	Full scale
Cross-sectional diameter of tori	2c	32 mm	1.6 m
Torus mass per unit length	m	0.257 kg/m	642.5 kg/m
Torus bending stiffness	EI	0.8467 Nm^2	2.65 $\times 10^8$
Mooring-line spring stiffness	k_s	25.9 N/m	64.8 kN/m
Truss spring stiffness	k_t	45 N/m	112.5 kN/m

spring and a truss and then measuring the resulting elongation x, from which the spring stiffnesses k were found from

$$k = \frac{F}{x} \tag{3.2}$$

For both the trusses and the mooring-line springs several measurements were made, and the average value of the spring-stiffness were used. In Table 3.2 the model and full scale parameters for both models are shown.

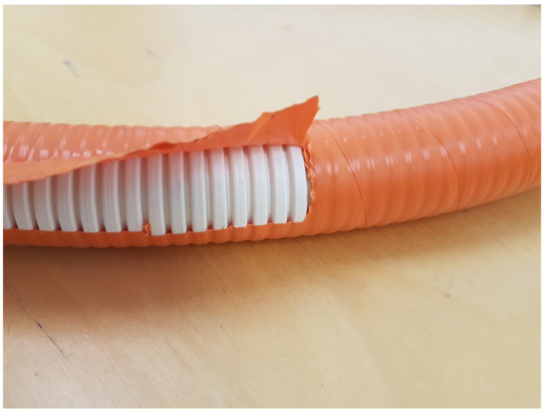

Figure 3.2: Corrugated tube enclosed by water repellant tape.

Table 3.4: Main dimensions of the model and the full scale structure for the multi-torus where Torus 1 is the outermost and Torus 5 is the innermost.

Torus	Model diameter	Full diameter	Model weight	Full weight
Torus 1	1.020 m	50 m	0.83 kg	103.8 $\times 10^3 kg$
Torus 2	0.825 m	40 m	0.70 kg	87.5 $\times 10^3 kg$
Torus 3	0.620 m	30 m	0.55 kg	68.8 $\times 10^3 kg$
Torus 4	0.423 m	20 m	0.40 kg	50.0 $\times 10^3 kg$
Torus 5	0.228 m	10 m	0.23 kg	28.8 $\times 10^3 kg$

(3.3)

3.2.1 Single-torus Model

The single-torus consists of one ring with dimensions as seen in Table 3.3.

Table 3.3: Main dimensions of the model consisting of a single-torus and the corresponding full scale structure.

Torus	Model diameter	Full scale diameter	Model weight	Full scale weight
single-torus	1 m	50 m	0.83 kg	103.8 $\times 10^3 kg$

3.2.2 Multi-torus Model

The multi-torus model consists of five rings with dimensions as seen in Table 3.4. On each ring there are eight plastic strips where elastic trusses are tied between the rings, each truss have a length of $10.2mm$ and a diameter of $4.0mm$. There are 8 trusses between each ring, and in total there are 32 elastic trusses, and the same amount of strips.

3.3 Experimental Setup

The experimental setup for both models were the same with an exception for some of the instruments. Figure 3.3 shows the experimental setup for the multi-torus which includes the motion-capture cameras.

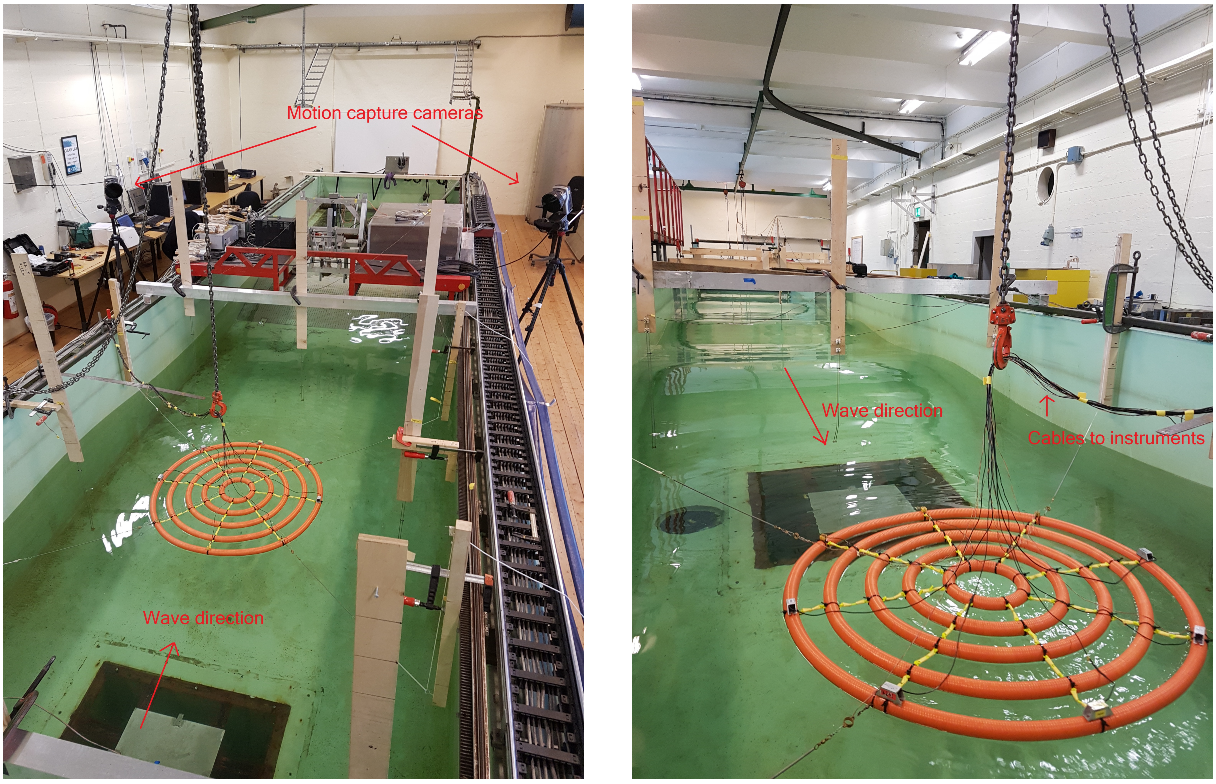

Figure 3.3: In the left figure the experimental setup is seen from the wave direction. The mooring-lines and some of the wave probes can be seen, as well as the two motion capture cameras on the left and right side of the tank. In the right figure the model is seen towards the wave direction. The accelerometers, the force rings and the cables connecting the instruments to the work station are visible.

Figure 3.4 illustrates the setup with some of its main dimensions. The towing tank is 25m long, 2.5m wide and 1.2m deep, and the waves are generated by a flap-piston wave maker that creates waves in the negative x-direction. There is also a damping beach at the end of the tank to increase the energy dissipation of the waves and make the surface calm in between tests.

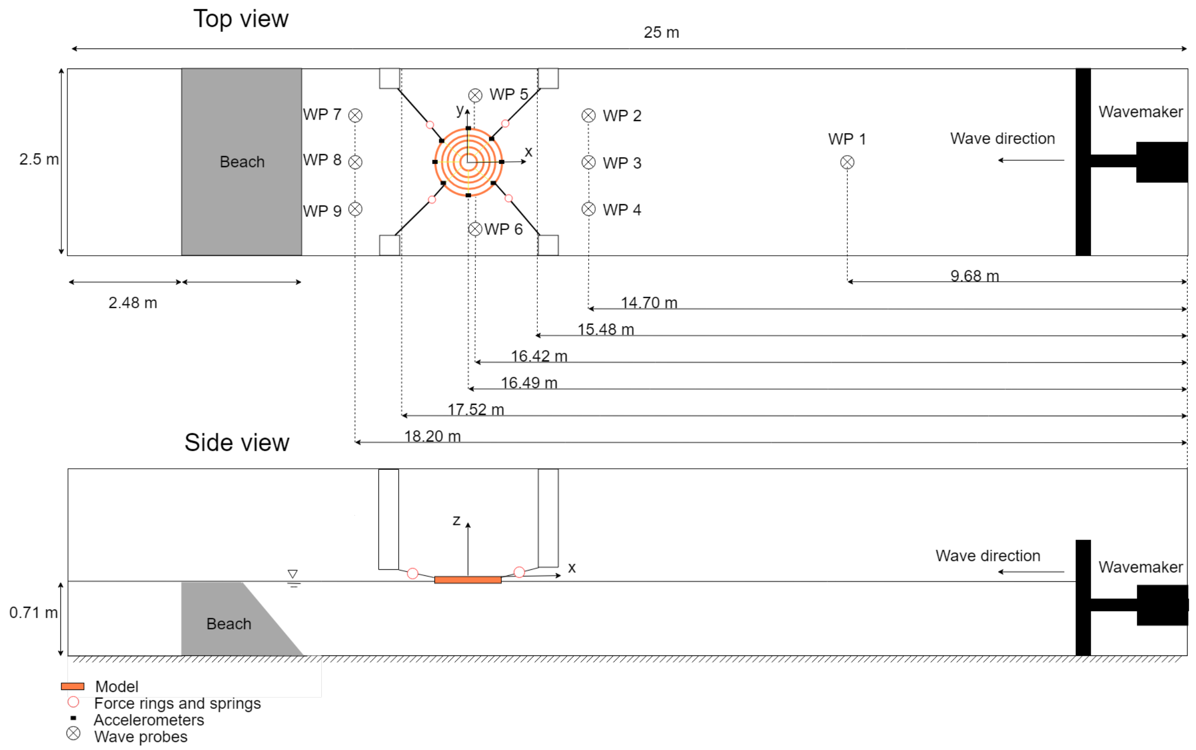

Figure 3.4: Experimental setup of the multi-torus model. The upper figure shows the top view, and the lower figure shows the side view.

The models were attached to four mooring-lines symmetrically distributed around the models at $\beta = 45^o$, $\beta = 135^o$, $\beta = 225^o$ and $\beta = 315^o$. The mooring-lines were subjected to a pre-tension $T_p = 5N$ to keep the springs from slacking and becoming submerged when the models moved in the horizontal motion with large waves.

3.3.1 Instrumentation

Different instruments recorded the wave height, flap motion, accelerations, motions and forces acting on the model. Each of the instruments were calibrated and in total, 130 channels recorded at 200 Hz, creating a large amount of data. In this section a brief overview over the instruments is presented.

Force rings

Each of the four mooring-lines were equipped with a force ring to measure the forces they were exposed to, and were thus positioned symmetrically around the models at $\beta = 45^o$, $\beta = 135^o$, $\beta = 225^o$ and $\beta = 315^o$.

Wave probes

Nine wave probes were placed around the tank to measure the wave elevation at sites of interest. Results from wave probe 9 showed a large deviance from the other wave probes and were thus not included in post-processing.

Cameras

At times, a camera was used to record the motions of the torus and different phenomenons of interest, such as overtopping.

Accelerometers

The vertical accelerations were measured by eight accelerometers evenly distributed around a torus with an interval of $\beta = 37.5^o$, as seen in Figure 2.3. To measure the movements of each torus the accelerometers had to be re-positioned on the torus of interest. As the fourth torus and fifth torus, the two innermost, were almost rigid, their vertical accelerations were not measured with accelerometers. However, the accelerations for the outermost torus, the second torus and the third torus were measured for different wave series. Two different types of accelerometers were used. Three smaller ones with a weight of $10g$, corresponding to $1.25tons$ in full scale, and five larger accelerometers with a weight of $30g$ corresponding to $3.75tons$ in full scale. The weight of these accelerometers are large enough to have had an effect on the motion of models.

Motion capture

By utilizing two motion-capture cameras it was possible to measure the motions of the multi-torus in the x,y,z-direction (3D), in addition to the error of margin related to that position. A camera and some of the markers can be seen in Figure 3.5.

The multi-torus was equipped with a total of 24 reflexive markers and the position of the markers before starting a wave series can be seen in Figure 3.6. The local coordinate system had to be re-calibrated almost every day. This involved covering all the markers and using a set of calibration tools familiar to the software. Then, the position of each marker was registered in the motion capture software before starting the measurements to make sure that the markers were correctly placed. The flat shape of the multi-torus confused the software. When the water in the tank was lying still, the markers existed in the x, y-plane only and this gave the software some trouble registering the correct positions in 3D. This further increased the need for doing re-calibration, and for every re-calibration, the positions of the markers and the channel they fed data into, changed. It

Figure 3.5: The Oqus Camera, used for measuring the x,y,z-position of the 24 motion capture markers at 200 Hz. Equipment and instruments used to measure movement, force and acceleration of the model.

therefore became necessary to create a system to organize the markers and the channels they fed data into. This was done by first plotting the markers original position and setting up a script that identified their position, and then placed the data in the correct order.

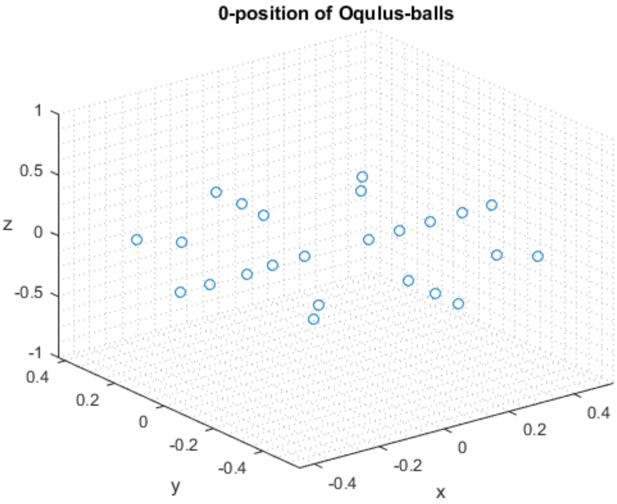

Figure 3.6: Position of markers before starting the wave-maker. 8 markers were placed on the outer and second ring, 4 markers were placed on the third ring, and 2 markers were placed on the fourth and inner ring.

To be sure that each marker were correctly registered for the duration of each test, the positions of each marker were plotted over time as well. An extract of plots from one of the movies created for this purpose can be seen in Figure 3.7. It shows the positions of the markers during one regular wave period. To be able to differentiate between the markers, orange lines are added between the markers of the two outermost tori and yellow lines between the markers where the trusses are located.

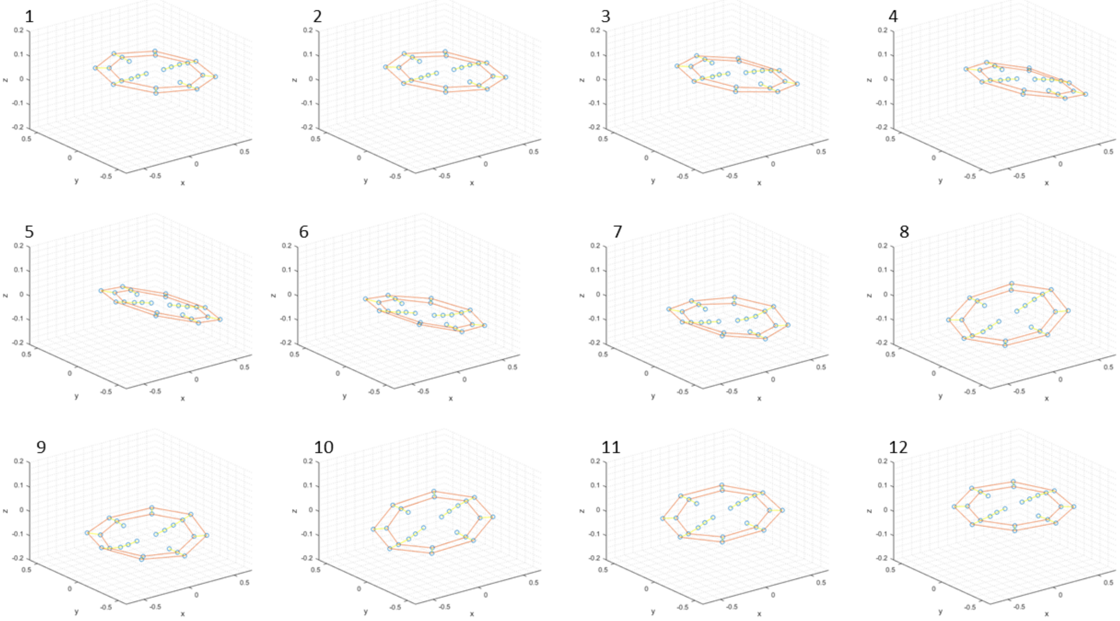

Figure 3.7: Marker positions for one regular wave period with $T = 12s$, $H/\lambda = 1/25$. Orange lines are added between the markers of the two outermost rings to illustrate the global behavior of the tori. Yellow lines are also added to illustrate the trusses between the different rings at positions where the markers are.

Compared to the accelerometers, the motion capture markers are very light and can be placed anywhere without requiring any cables. However, they have to be in view of the two motion capture cameras at all times or else the data for the marker is lost for that duration of time. This could happen for large waves that blocked the view, overtopping that submerged the markers, or other instruments and cables that got in the way as the multi-torus moves in motion with the waves.

3.4 Wave-series Characteristics

Both regular and irregular waves were used in the experiment, with several different wave conditions in order to get a broad range of results on the models behavior. Here, a wave-series refers to a set of waves generated, where all the variables deciding the shape of the wave are kept constant for a given amount of waves or time.

3.4.1 Regular waves

Incident waves propagating along the x-axis were used. The wave steepness H/λ and the wave period $T = 2\pi/\omega$ were varied for each wave series. The wave-series that were generated can be seen in full-scale in Table 3.5, and the corresponding waves-series in model-scale can be seen in Appendix C. Both the multi-torus and the single-torus were tested in regular waves. The length of each test depended on the amount of wave-series to be tested. Each wave-series consisted of 5 ramp-waves preceding the generation of 60 waves of steady state. Between each wave-series there was a pause of 120 seconds to allow the water in the tank to become still.

T [s]	$\lambda[m]$	H/λ = 1/60 H [m]	H/λ = 1/40 H [m]	H/λ = 1/30 H [m]	H/λ = 1/20 H [m]
2.0	6.2452	0.1041	0.1561	0.2082	0.3123
2.5	9.7582	0.1626	0.2440	0.3253	0.4879
3.0	14.0518	0.2342	0.3513	0.4684	0.7026
3.5	19.1260	0.3188	0.4782	0.6375	0.9563
4.0	24.9810	0.4163	0.6245	0.8327	1.2490
4.5	31.6165	0.5269	0.7904	1.0539	1.5808
5.0	39.0319	0.6505	0.9758	1.3011	1.9516
5.5	47.2222	0.7870	1.1806	1.5741	2.3611
6.0	56.1672	0.9361	1.4042	1.8722	2.8084
6.5	65.8153	1.0969	1.6454	2.1938	3.2908
7.0	76.0710	1.2679	1.9018	2.5357	3.8036
7.5	86.8002	1.4467	2.1700	2.8933	4.3400
8.0	97.8525	1.6309	2.4463	3.2618	4.8926
8.5	109.0881	1.8181	2.7272	3.6363	5.4544
9.0	120.3954	2.0066	3.0099	4.0132	6.0198
9.5	131.6953	2.1949	3.2924	4.3898	6.5848
10.0	142.9379	2.3823	3.5734	4.7646	7.1469
10.5	154.0946	2.5682	3.8524	5.1365	7.7047
11.0	165.1515	2.7525	4.1288	5.5050	8.2576
11.5	176.1040	2.9351	4.4026	5.8701	8.8052
12.0	186.9532	3.1159	4.6738	6.2318	9.3477
12.5	197.7033	3.2951	4.9426	6.5901	9.8852
13.0	208.3599	3.4727	5.2090	6.9453	10.4180
13.5	218.9295	3.6488	5.4732	7.2976	10.9465
14.0	229.4186	3.8236	5.7355	7.6473	11.4709

Table 3.5: Test conditions for regular waves in full scale.

3.4.2 Irregular waves

Irregular wave-tests were performed where the peak wave period T_p was kept constant and the significant wave heights H_s varied for each wave-series. The different test conditions used for irregular waves can be seen in full scale in Table C.2 and model scale in C.

Table 3.6: Test conditions for irregular waves in full scale.

	$\mathrm{T}_p = 12s$	$\mathrm{T}_p = 10s$	$\mathrm{T}_p = 9s$	$\mathrm{T}_p = 8s$
$\mathrm{H}_s[m]$	1.0	2.0	2.0	0.5
	2.0	3.0	3.0	1.0
	3.0	4.0	4.0	1.5
	4.0	-	-	2.0
	5.0	-	-	2.5
	6.0	-	-	3.0
	7.0	-	-	3.5
	8.0	-	-	4.0

3.5 Post-Processing

In total, 43 tests produced usable data and were subsequently post-processed. Each test consisted of a different setup and varying wave-conditions. For regular waves, the wave-series came in intervals of 60 waves at a time, of which data from twenty waves in steady-state were extracted and passed through a band-pass filter that transformed the time-dependent data to frequency-dependent by the use of FFT. The time interval for the twenty waves in steady state were utilized to extract the corresponding data from all the instruments measuring the response as well, thus acquiring the input and the following response. The accelerometers measured the accelerations of the models during testing. These accelerations were integrated to acquire the positions of the models. Modal analysis was used on all data acquired from the accelerometers and the motion capture system. The upper figure in Figure 3.8 illustrates the raw data of wave elevation measured by wave probes for a full test and the extraction of one wave series, the lower figure shows the subsequent selection of twenty filtered waves in steady-state that was used.

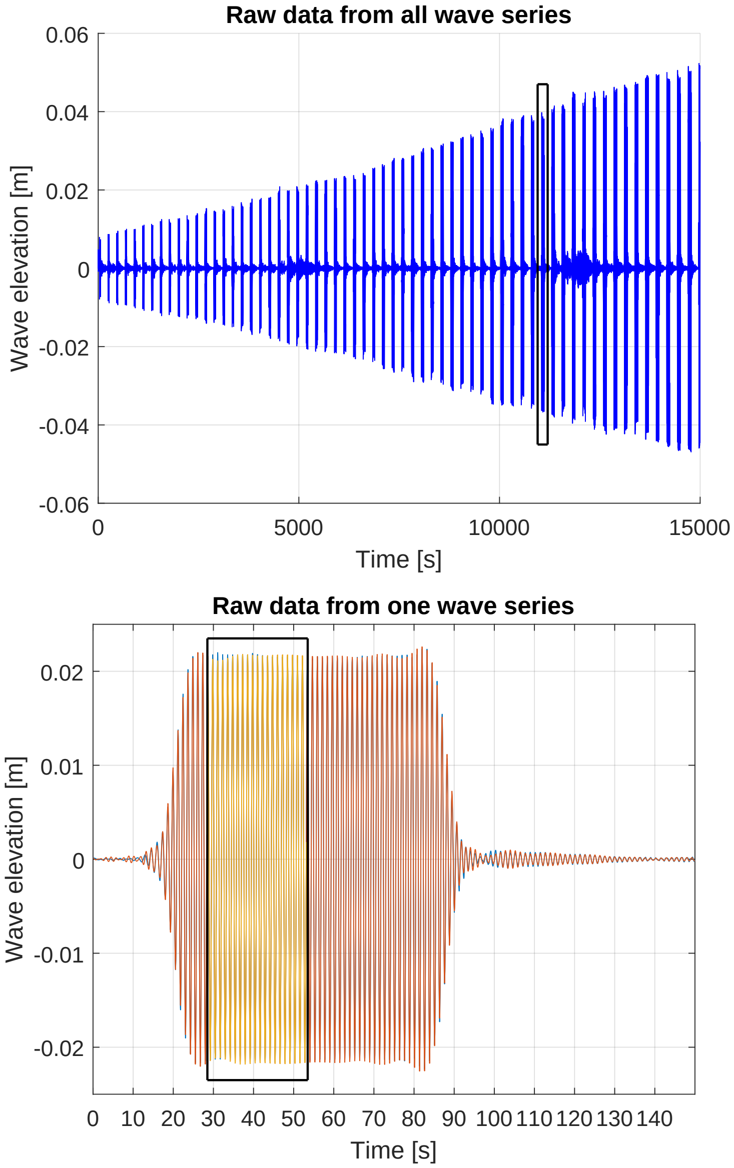

Figure 3.8: In the top figure the raw data from one wave series is extracted from all the wave series. In the figure below, the extracted wave series is shown from which twenty waves in the steady-state are extracted again and filtered.

A similar process was performed for the irregular waves, the difference being that there was no steady-state to be reached so raw data was selected and cut manually before being filtered through spectral analysis.

3.6 Error Sources

There were several potential sources of error during the testing that might have affected the final results. The largest and most probable error sources are presented in this section.

The models were close to circular and symmetric, but not perfectly so, producing a potentially small error source. This imperfection was also increased due to the mooring-lines pulling the outer torus in four directions. The size and relative size of the different tori also varied slightly, which can give rise to slight deviations between the theoretical and experiemental results. The simplistic approach to finding the bending stiffness of the tori using the cantilever beam theory did not give the exact bending stiffness, but a close approximation.

The mooring-lines, accelerometers and motion capture markers were not perfectly symmetrically positioned, and there is a possibility that there were small variations in the pre-tension of the springs. The cables connecting the instruments to the computer might have affected the motions of the tori slightly. Temperature variations in the water affects the waves and the measurements of the instruments. The instruments are also prone to drift slightly over time, producing different measurements during a test, and between different tests. The motion capture system is not as reliable as the accelerometers as there are several factors that can disturb the measurements, and the distance between the cameras and the motion capture markers might affect the precision of the measurements for smaller motions. The wave probes were not reliable over time and had to be tested and calibrated to make sure that the deviating measurements were not too large.

The wave maker generates waves that deviate slightly from the input-settings, producing slightly smaller waves. The waves also dissipate slightly on their way from the wave flap to the model, which is particularly true for smaller waves. This can mainly be attributed to wave-reflections of the tank-walls. In addition, the waves with smaller wave steepness have a tendency to be unstable and collapse slightly, creating lower wave amplitudes. The waiting time between the tests, and the usage of a damping beach allowed the water surface to calm before starting each test. However, the water surface never became completely still between tests with waves radiating off the tank-walls, and thus affecting the induced waves. There were water leakage on the sides of the wave flap, and water was pumped into the tank at regular intervals. This means there were small variations in water depth in the tank during the tests.

Chapter 4

Results and Discussion - Regular Waves

This chapter presents the results acquired from tests of a single-torus and the multi-torus in regular waves, which are in turn compared to the existing theory for the vertical response presented in Chapter 2 and explained in Appendix A. Results from different wave-steepnesses are included, where most of the results in this chapter comes from tests with wave steepness $H/\lambda = 1/60$. In Appendix D, the RAO-results from $H/\lambda = 1/30$ are included. Data for tests with other wave steepnesses that show interesting phenomenon are also presented. All the measurements plotted against the non-dimensional wave number kR, where the torus outer radius $R = 0.51$ for all plots.

4.1 Wave Height

Experimental wave height measured by wave probe 1 are presented for different steepness. Figure 4.1, gives an impression of how the wave elevation varies with kR for the different wave steepnesses and shows how the wave elevation has a substantial increase for $kR < 11$, corresponding to $T > 3s$ in full scale, for all steepnesses. As there is a considerable distance between the wave maker and wave probe 1 and even longer to the model, the smaller waves, especially for $T < 3s$, are expected to dissipate slightly.

In Figure 4.2, the theoretical wave amplitudes are compared with the amplitude measured by wave probe 1. The input to the wave maker should have created waves with wave steepnesses $H/\lambda = 1/60$ and $H/\lambda = 1/30$, instead the resulting measured wave amplitudes closely resembled the wave amplitudes expected for $H/\lambda = 1/65$ and $H/\lambda = 1/32$, respectively.

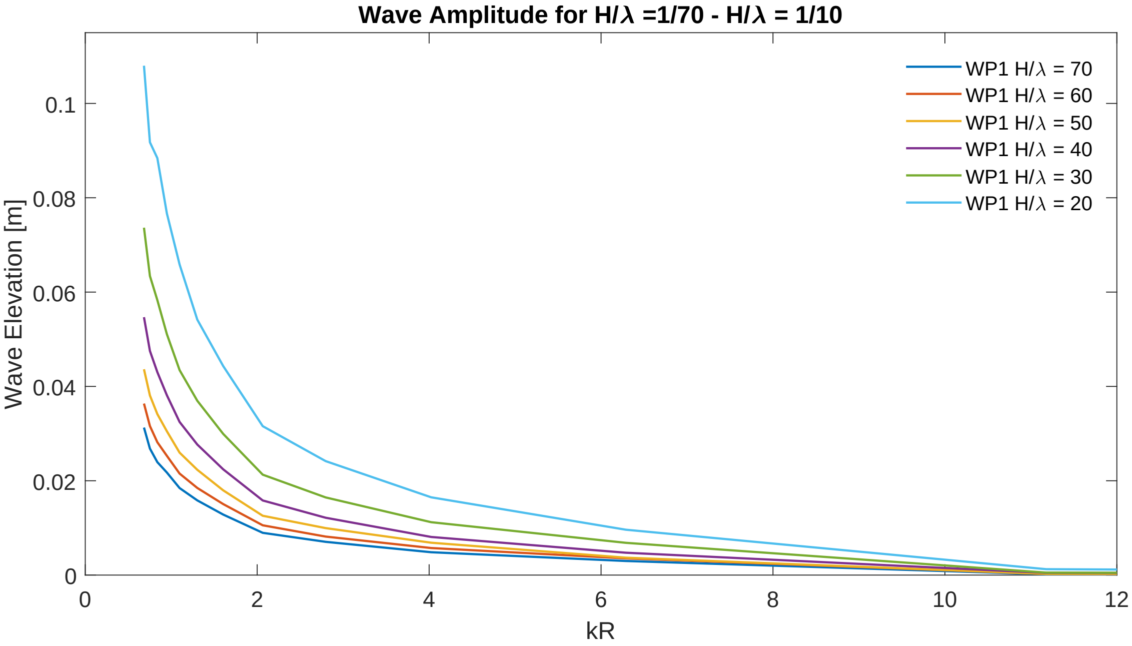

Figure 4.1: Measured wave amplitude in model scale for regular waves as measured by wave probe 1 for wave steepness $H/\lambda = 1/70$ to $H/\lambda = 1/20$. The wave elevations are plotted against the frequency dependent non-dimensional wave number kR.

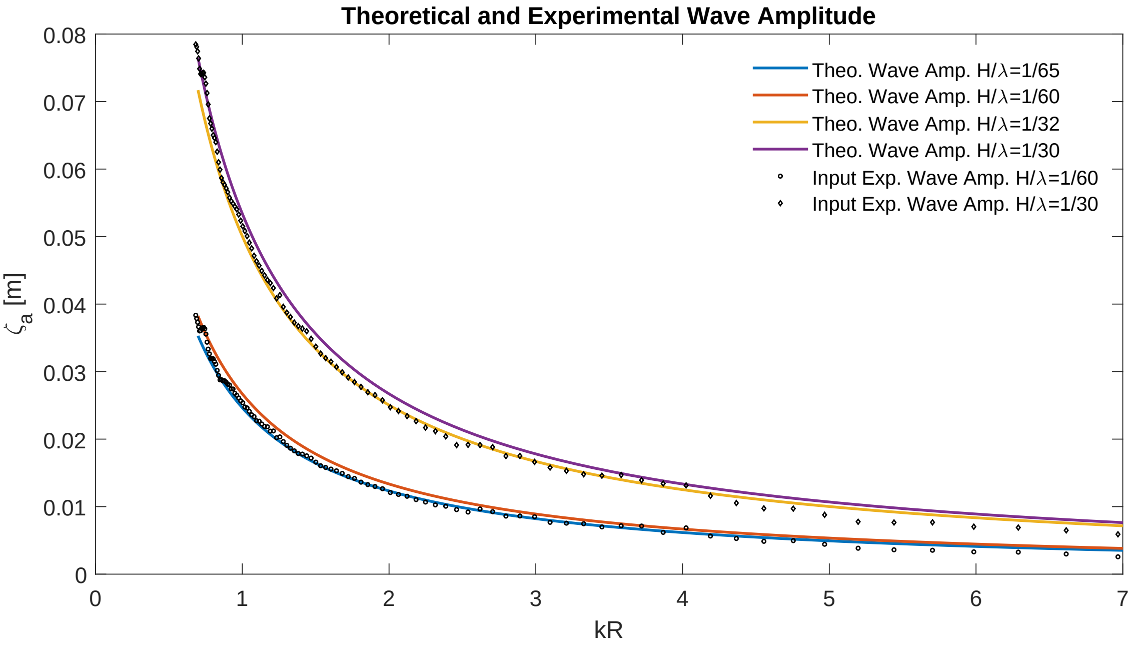

Figure 4.2: Measured wave amplitude in model scale for regular waves with input wave steepness $H/\lambda = 1/60$ and $H/\lambda = 1/30$, plotted together with its corresponding theoretical wave amplitude and the theoretical wave amplitude for $H/\lambda = 1/65$ and $H/\lambda = 1/41$.

This indicates that the waves used during the study were smaller than they were supposed to be. For simplicity and to avoid confusion, the waves are still referred to by the wave steepness input, and not by the actual wave steepness measured.

The effect on the waves by the multi-torus can be seen in Figure 4.3, which shows the wave height measured by wave probe 3 and 8 for steepness $H/\lambda = 1/60$ and $H/\lambda = 1/30$. Wave probe 3 is situated in front of the multi-torus and wave probe 8 right behind it, thus the effect of the multi-torus on the wave height can be compared. Interaction between wave height and multi-torus is most visible between $kR = 10$ and $kR = 2$, where the wave amplitude is reduced for the most part, except at $kR \approx 4.2$. A peak can be seen there, and the wave amplitude at wave probe 8 exceeds the wave amplitude at wave probe 3 for both steepnesses, indicating non-linear effects that increases the wave height in this frequency range.

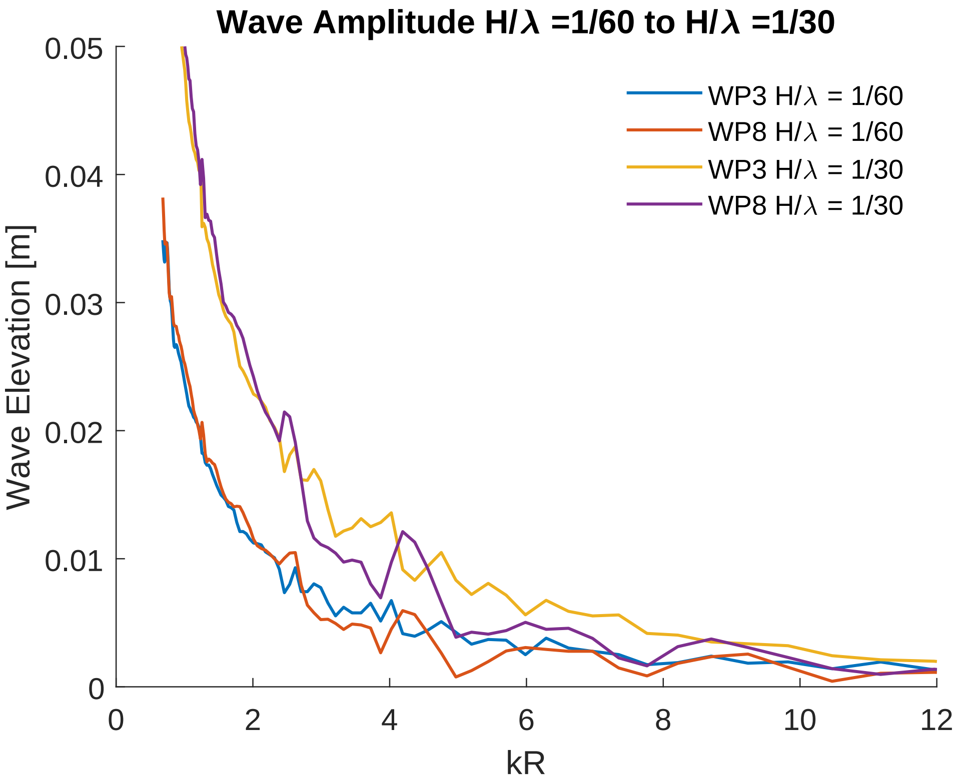

Figure 4.3: Measured wave amplitude in model scale with wave steepness $H/\lambda = 1/60$ and $H/\lambda = 1/30$ for wave probe 3 and 8, where wave probe 3 is situated in front of the multi-torus and wave probe 8 is situated behind the multi-torus.

4.2 Time Series Examples

Figure 4.4 shows an example from a time-series with $kR = 1.0061$, corresponding to $T = 10s$ in full scale, of the measured accelerations and the corresponding vertical position of the accelerometer at $\beta = 180^o$ plotted against the non-dimensional time t/T.

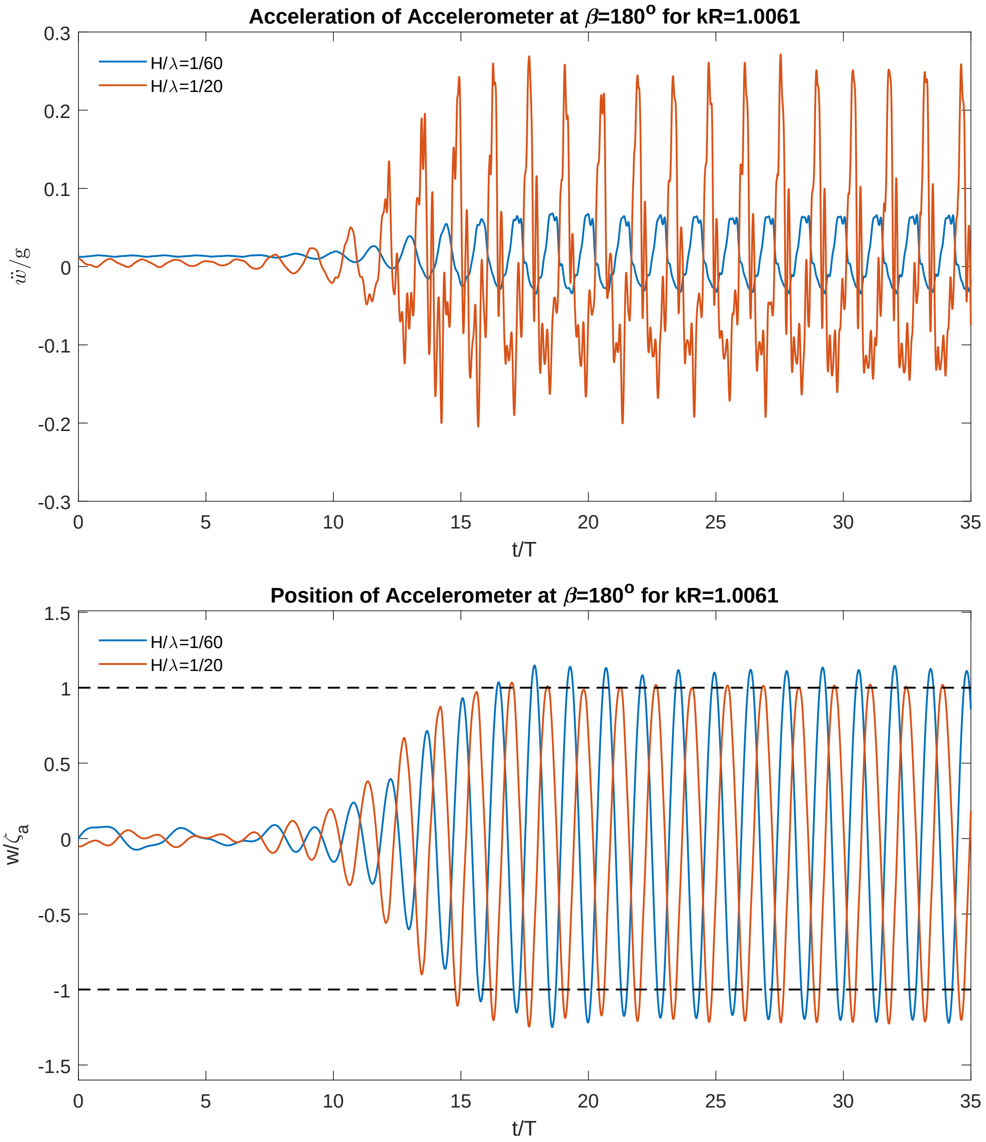

Figure 4.4: Both figures show time-series examples of experimental results from a wave series with $H/\lambda = 1/60$ and $H/\lambda = 1/20$ at $kR = 1.0061$. Upper figure shows the non-dimensional acceleration $\ddot{w}$ at $\beta = 180^o$. Lower figure shows a time-series example of the non-dimensional motion w of the accelerometer at $\beta = 180$ relative to the incident wave ζ_a.

The accelerations seen in the top figure are made non-dimensional by the acceleration of gravity g, and are not particularly sinusoidal. The vertical motion seen in the lower figure are made non-dimensional by the incident wave amplitude ζ_a and are much more harmonic.

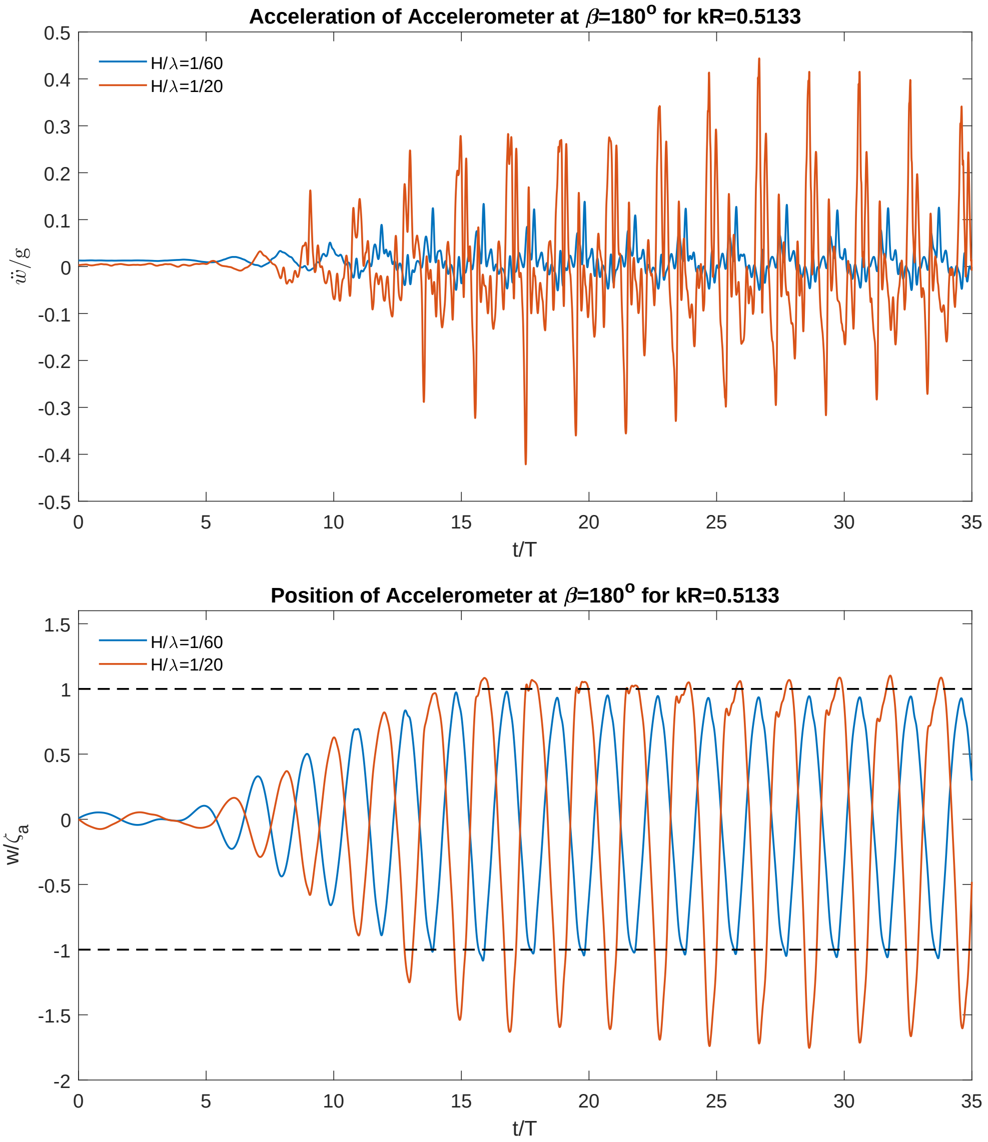

Figure 4.5: Multi-torus: Both figures show time-series examples of experimental results from a wave series with $H/\lambda = 1/60$ and $H/\lambda = 1/20$ with $kR = 0.5133$. Upper figure shows the non-dimensional acceleration $\ddot{w}$ at $\beta = 180^o$. Lower figure shows a time-series example of the non-dimensional motion w of the accelerometer at $\beta = 180^o$ relative to the incident wave ζ_a.

The vertical motion is lower relative to the wave height for $H/\lambda = 1/20$ in the positive direction, but approximates the vertical motion for $H/\lambda = 1/60$ in the negative direction-

This means that the negative vertical motion of the multi-torus is larger than the wave amplitude for both steepnesses, and that there is a possibility of submergence.

Another example of a time-series with $kR = 0.5133$, corresponding to $T = 14s$ in full scale, is included in Figure 4.5. The vertical motion in the negative direction is much larger here for $H/\lambda = 1/20$, strongly suggesting overtopping and submergence. More time-series are included in Appendix F, and are meant to demonstrate how the motion of the multi-torus relative to the wave amplitude varies for different wave conditions.

4.3 Vertical Response Amplitude Operators

The wave-induced vertical response of the models was measured by accelerometers. In addition, the multi-torus was also equipped with motion capture markers for some of the tests, thus it was possible to measure the movements of the multi-torus in the x, y, z-direction. In this section the results based on the vertical motion in the z-direction are presented.

4.3.1 Single-Torus RAO

Figure 4.6 shows the numerical RAO of the Linear-Slender Body theory (LST) and the Zero-Frequency theory (ZFT), compared to the experimental RAO for a single-torus in heave, pitch, first flexible mode and second flexible mode in a wave steepness of $H/ = 1/60$. For lower frequencies there are good agreement between the theoretical predictions and the experimental results. As $\omega \to 0$ for ZFT, the predictions deviate and for higher frequencies ZFT fails to predict the motion of a single-torus. Between the LST and the experimental results there are still agreement, even for higher frequencies, although they are not completely in phase. The torus carried eight accelerometers, which are not enough points to predict second flexible mode, $n = 3$, and are thus expected to deviate slightly from numerical predictions, which is also evident in the figure.

4.3.2 Multi-torus

Figure 4.7 shows the numerical RAO of the LST compared to the experimental RAO measured by the accelerometers and the motion capture markers for the outer torus of the multi-torus in heave, pitch, first flexible mode and second flexible mode in a wave-steepness of $H/\lambda = 1/60$.

In heave, there are good agreement between the numerical and the two experimental RAOs for $kR < 2.5$, but for higher kR the deviation in the results increases. The experimental RAO are seen to have less motion relative to the waves for smaller wave periods,

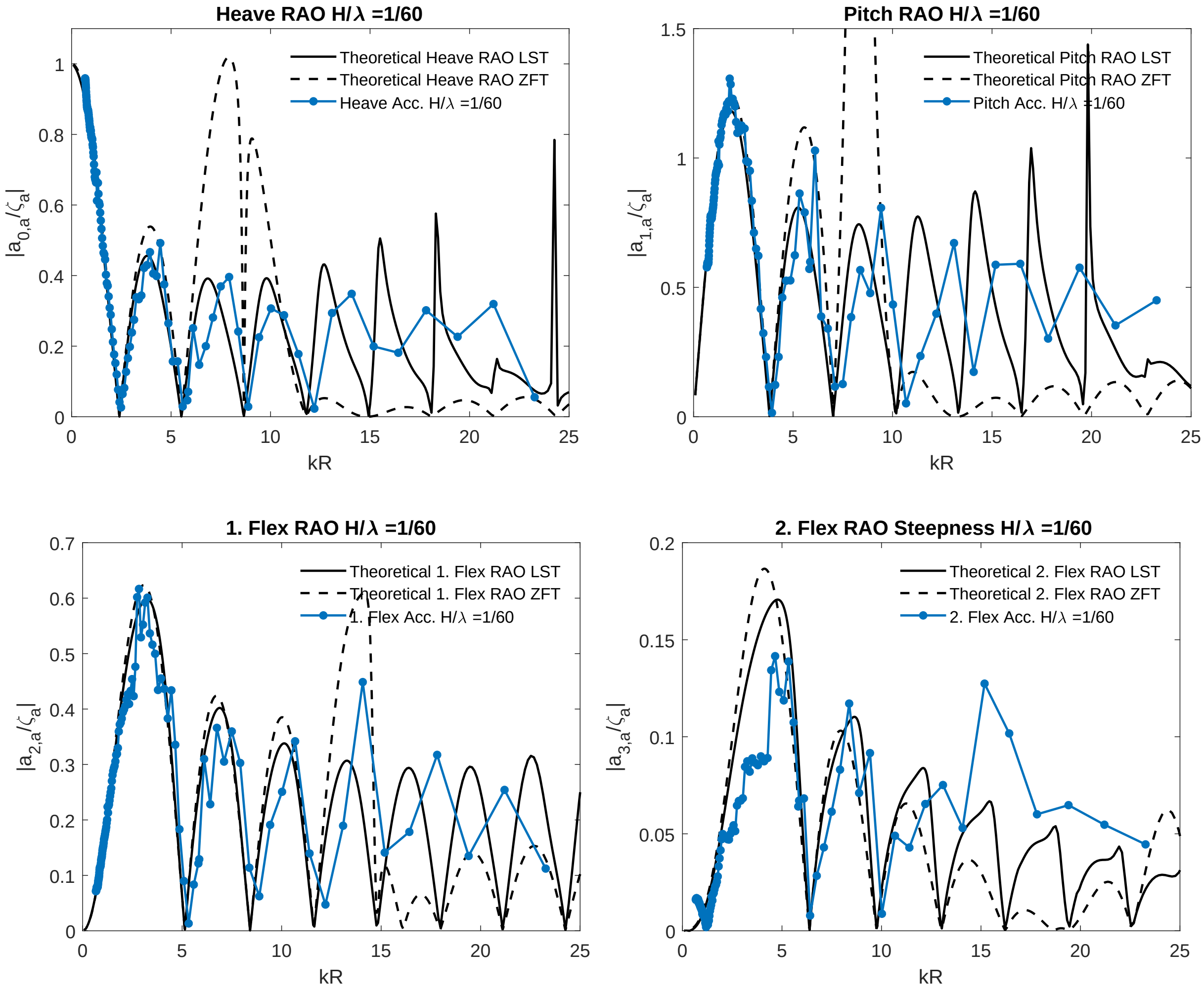

Figure 4.6: Numerical RAO for the Linear-Slender Body theory and the Zero-Frequency theory compared to the experimental RAO for the single-torus, in heave, pitch, first flexible mode and second flexible mode for wave steepness $H/\lambda = 1/60$.

and the peaks are also out of phase compared to the RAO for a single-torus. This is expected as the outer torus is attached to the other rings by trusses, which for waves with lower energy will have a stronger effect on the relative motion between the different tori. The results from the accelerometer and the motion capture markers also deviate slightly, where the accelerometers have a tendency of predicting a higher RAO than the motion-capture camera does. This is especially true for smaller waves where the movement in x, y, z-direction is very small, indicating that the precision of the motion capture camera is somewhat dependent on how large the movement of the motion capture markers are. The results from the three other modes deviate even more from the numerical RAO. The experimental RAO in second flexible mode is expected to be to deviate from the theoret-

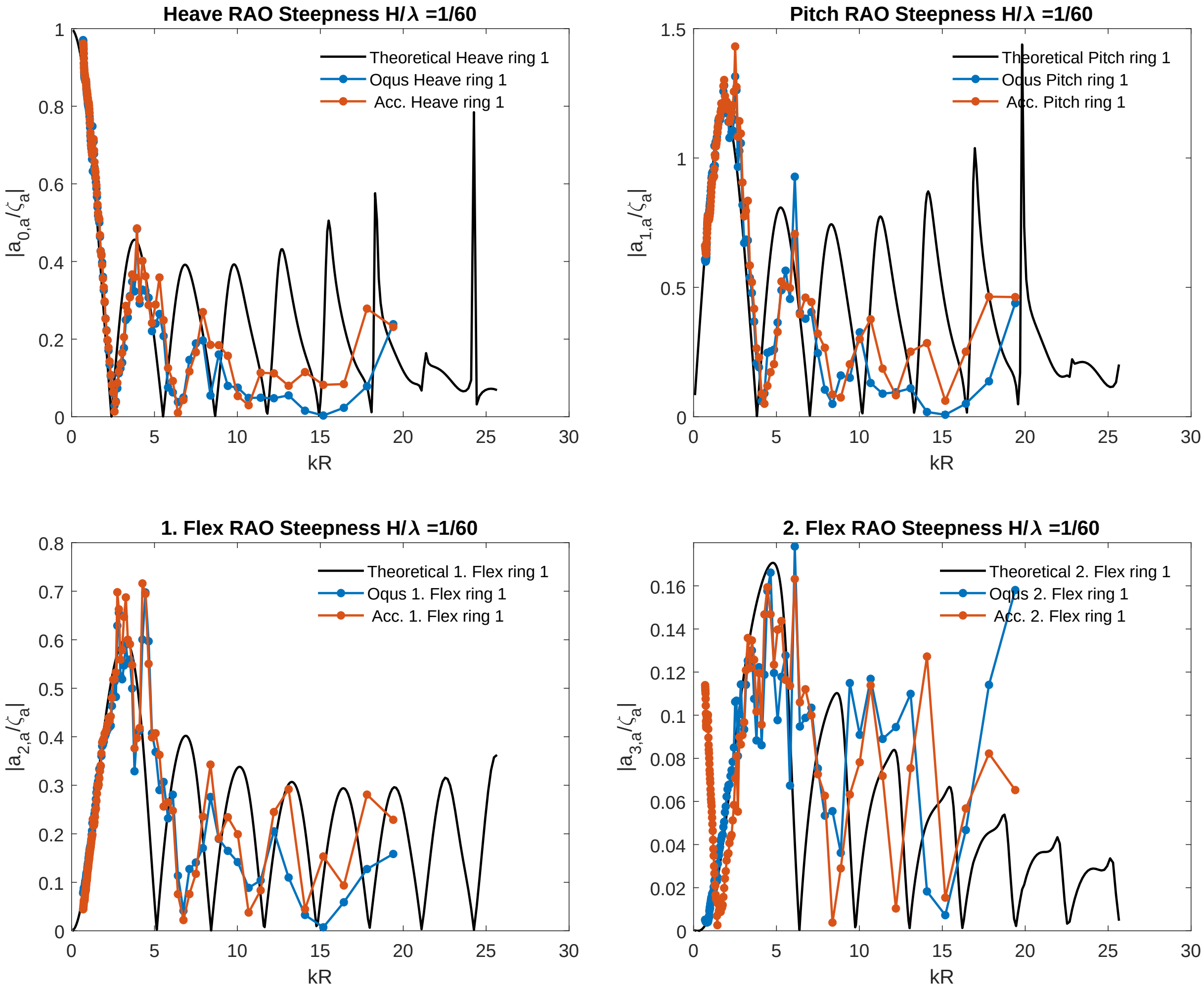

Figure 4.7: Numerical RAO for the Linear-Slender Body theory compared to the experimental RAO results for the multi-torus using accelerometers and motion capture markers, in heave, pitch, first flexible mode and second flexible mode for wave steepness $H/\lambda = 1/60$.

ical prediction, as the acceleelerations were only measured at eight different points on the torus, when more points are needed in order to be correctly predicted.

The experimental RAO in heave and pitch for the three outermost tori in wave steepness $H/\lambda = 1/60$ are compared with the LST for a single-torus in Figure 4.8, and in first flexible mode and second flexible mode in Figure 4.9. There seems to be more agreement between the numerical and experimental RAO for the outermost torus, ring 1, with a slight increase in deviation for the second torus, ring 2, and with a larger increase for the third torus, ring 3.

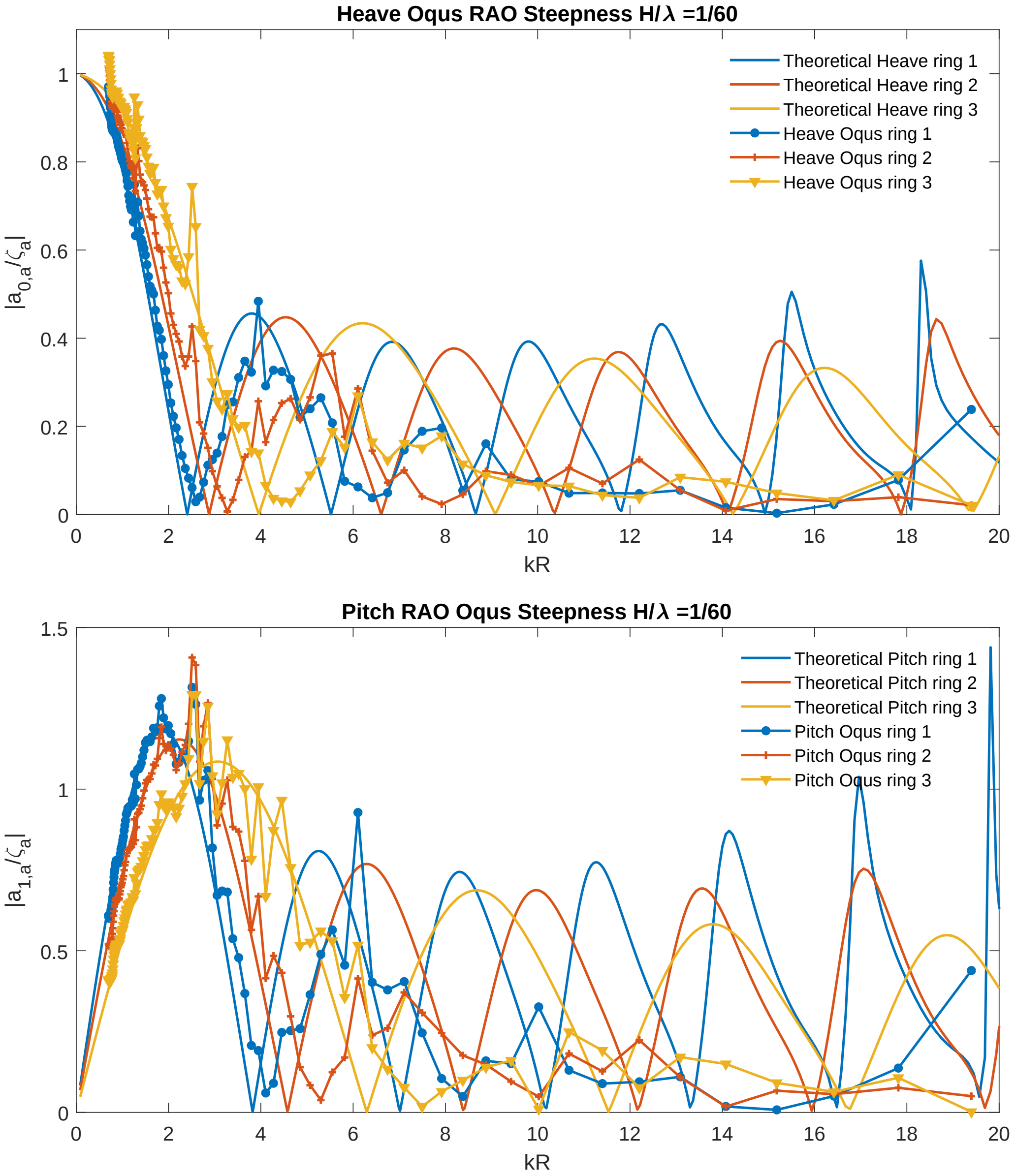

Figure 4.8: Numerical RAO for the Linear-Slender Body theory compared to the experimental RAO results using motion capture markers for ring 1, 2, 3 , in heave and pitch for wave steepness $H/\lambda = 1/60$.

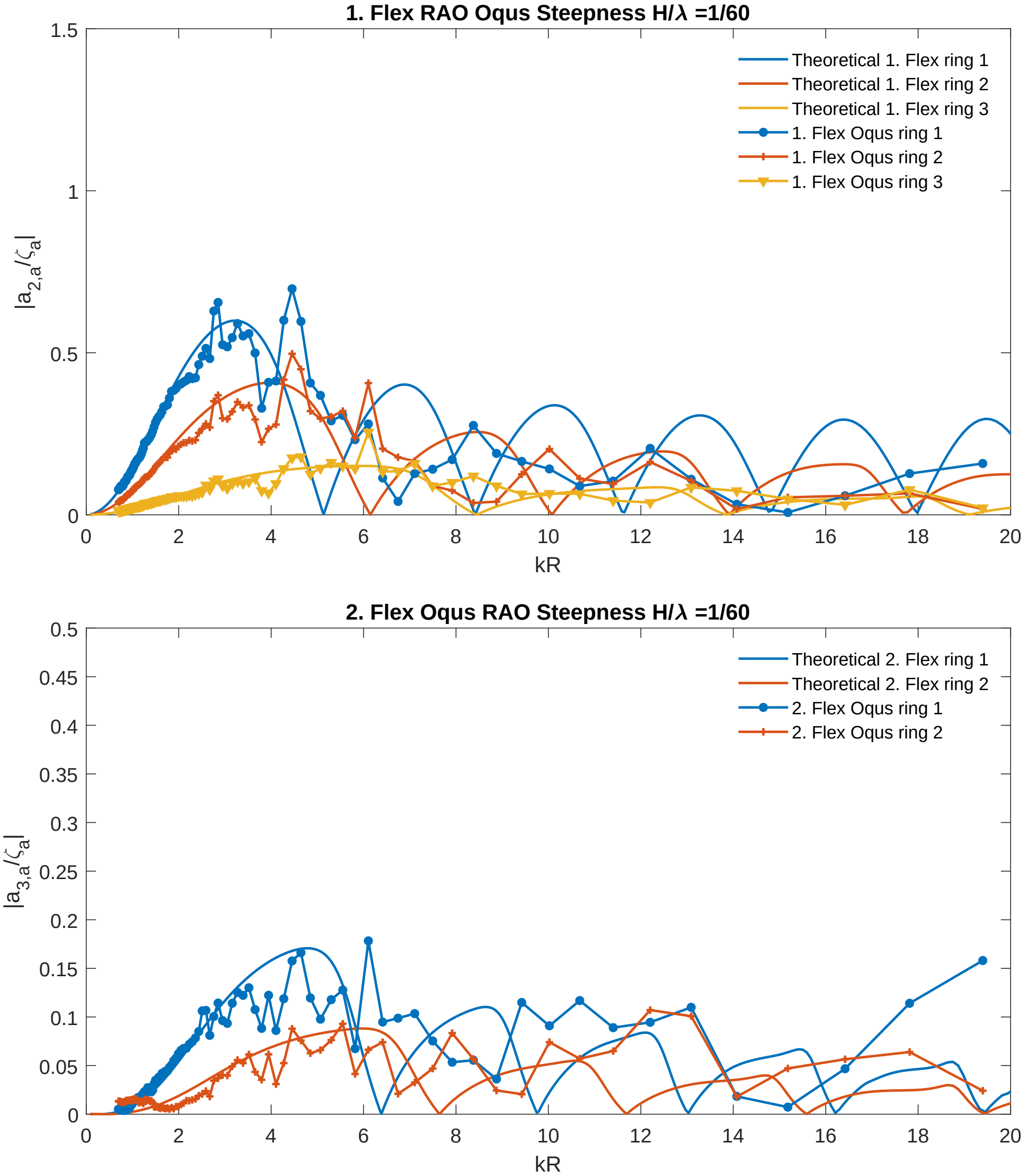

Figure 4.9: Numerical RAO for the Linear-Slender Body theory compared to the experimental RAO results using motion capture markers for ring 1, 2, 3 , in first flexible mode and second flexible mode for wave steepness $H/\lambda = 1/60$.

In Figure 4.10, the experimental and numerical RAO in heave and pitch are plotted for wave steepness $H/\lambda = 1/60$ for the two innermost tori are shown. There is very little motion of the tori relative to the waves. The difference in the abilities of the different tori to be predicted by LST can be attributed to at least four things; 1) That the truss-forces keep the tori in place, and that the interaction effects are larger for tori connected on both sides creating less motion relative to the wave. 2) That a decrease in circumferential size of the rings will increase their stiffness and thereforer their ability to move in motion with the waves. 3) That the smaller mass and added mass of the smaller tori means they are less able to resist the motions of the larger tori. 4) That the outer tori possibly shields the inner ones from some the wave forces.

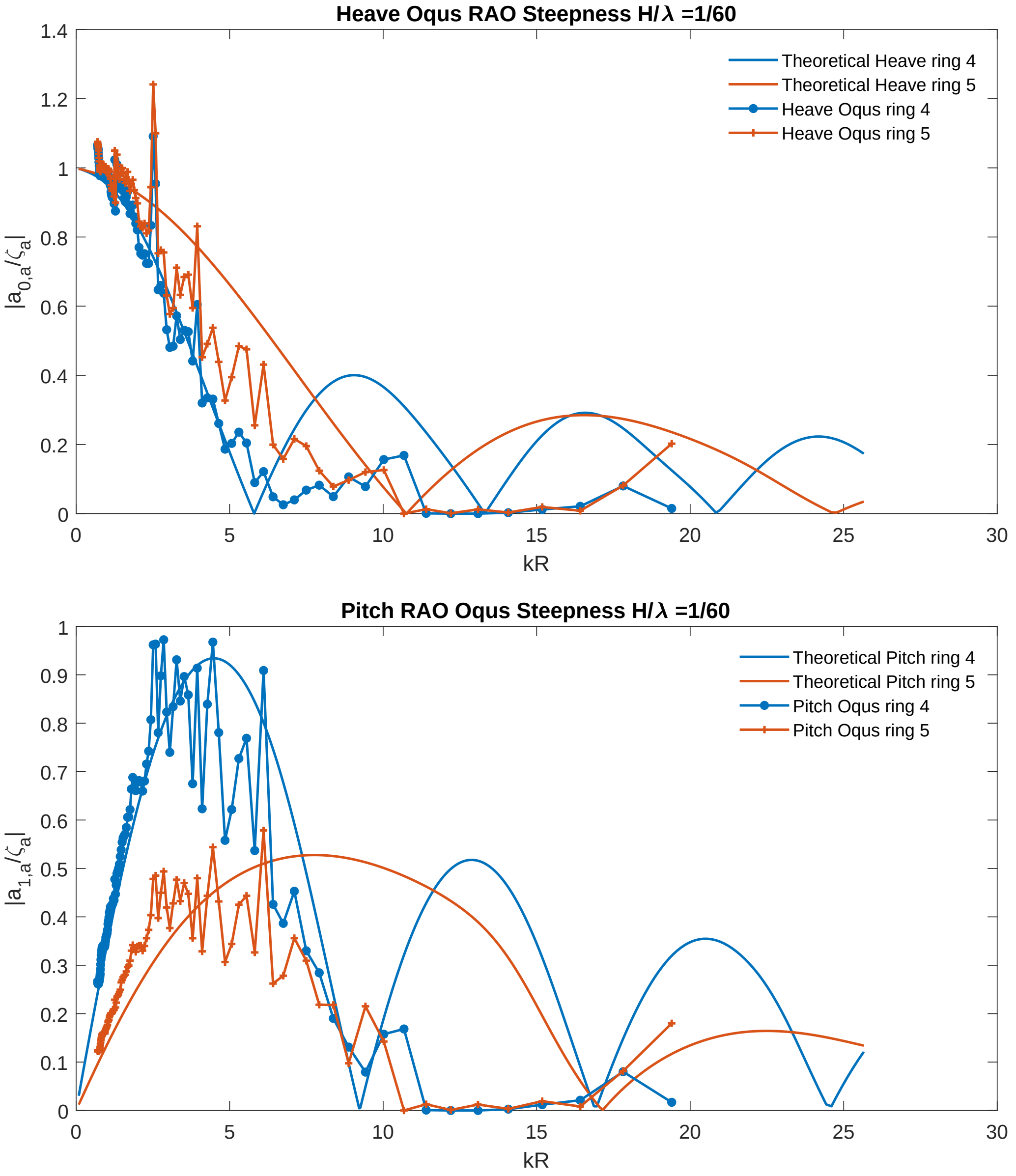

Figure 4.10: Numerical RAO for the Linear-Slender Body theory compared to the experimental RAO results using motion capture markers for ring 4 and 5, in heave and pitch for wave steepness $H/\lambda = 1/60$.

4.4 Horizontal Response Amplitude Operator

Using motion capture markers it was possible to measure the movements of the multi-torus in the x, y, z-direction. This made it possible to calculate the RAO in the horizontal plane. In this section the results based on the motion in the x-direction is presented.

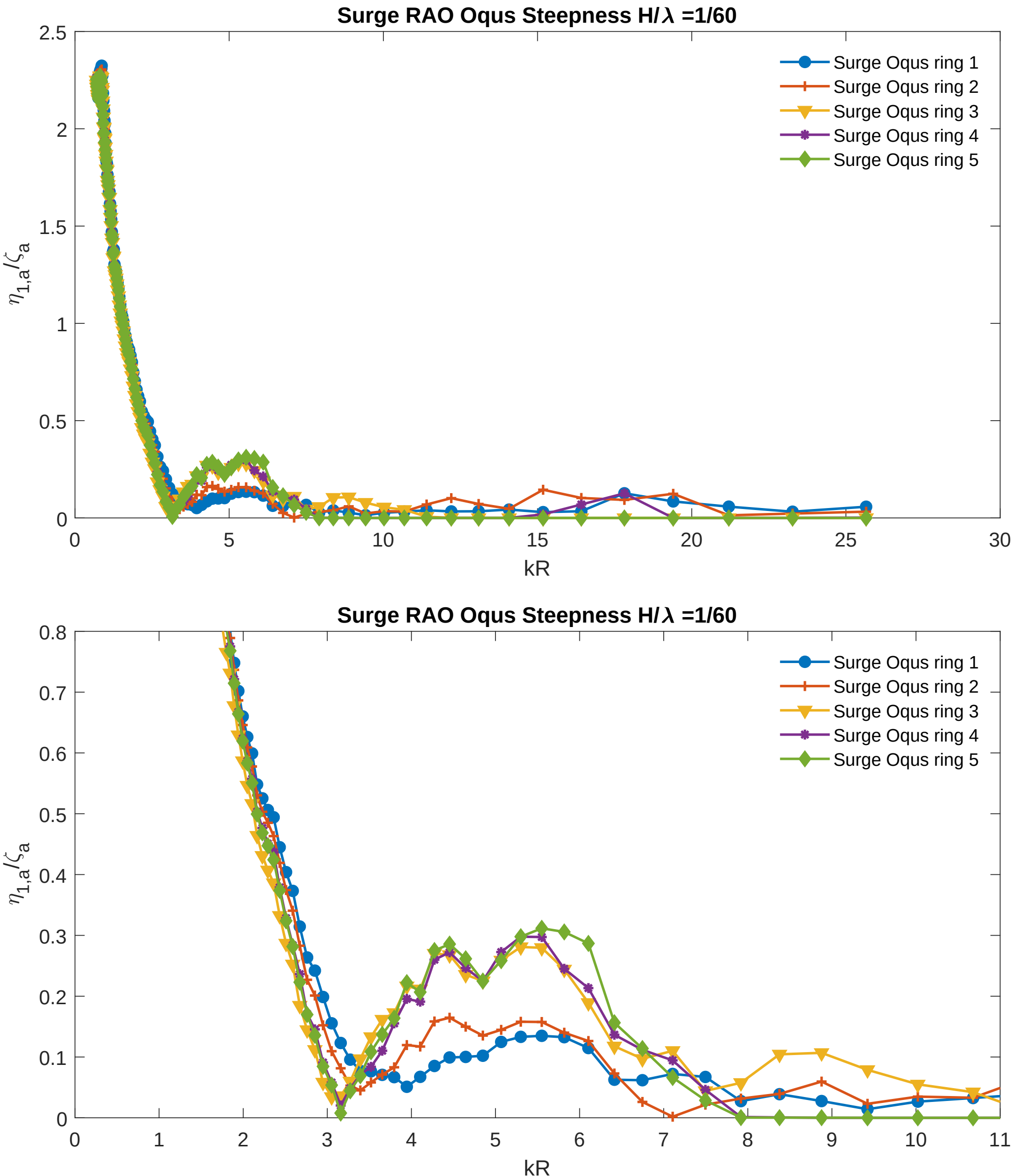

Figure 4.11: Experimental RAO-results using motion capture markers for ring 1, 2, 3, 4 and 5 in surge for wave steepness $H/\lambda = 1/60$. Upper figure provides the whole plot, whilst the lower figure gives a close-up on the frequency range where the motions of the tori diverge.

4.4.1 Surge

The experimental RAO in surge are found by taking the mean position in the $x-direction$ of the markers on each torus and dividing them by the wave amplitude ζ_a. Figure 4.11 compares the RAO of the multi-torus in surge for all the tori in wave steepness $H/\lambda = 1/60$. The upper figure presents the response for all kR, while the lower figure gives a close-up on a frequency of interest. There is clear indication of resonant behavior between the natural frequency of the multi-torus and the wave frequency at $kR \approx 2$. There seems to be a larger relative motion for torus 3, 4 and 5, than for torus 1 and 2 in the range $kR = 3 - 7$, where the outermost torus have the smallest relative motion and the inner torus have the largest relative motion. This can possibly be attributed to the outer tori amplifying the motions relative to the waves of the inner tori by the pull of the elastic trusses.

4.4.2 Ovalizations

Utilizing modal theory on the x-position of the motion capture markers yields the ovalization of the tori in the horizontal plane. Figure 4.12 shows the experimental ovalization as RAO for $n = 2$ for ring 1, 2 and 3 in the left figure and $n = 3$ for ring 1 and 2 in the right figure.

4.5 Harmonic Accelerations

In order to compare the magnitudes of the harmonic accelerations, this section presents the mean values of the steady-state amplitude of the non-dimensional first and second harmonic accelerations $\ddot{w}(\omega)/g$ plotted against the non-dimensional wave number kR. The measurements of the accelerations are done on the outermost torus of the multi-torus for different wave steepnesses. In this section only results from accelerometers placed on $\beta = 0^o$ and $\beta = 180^o$ are shown, results from the rest of the accelerometers are included in Appendix G.

4.5.1 First Harmonic Acceleration

Figure 4.13 shows the first harmonic accelerations for $\beta = 0^o$ and $\beta = 180^o$ on the single-torus and the multi-torus for varying wave steepnesses. The first harmonic accelerations increases for higher wave steepnesses, and there seems to be a higher relative increase of accelerations at $\beta = 180^o$ compared to at $\beta = 0^o$ for both models, especially for wave steepness $H/\lambda = 1/20$. The multi-torus seems to be subjected to slightly larger accelerations than the single-torus.

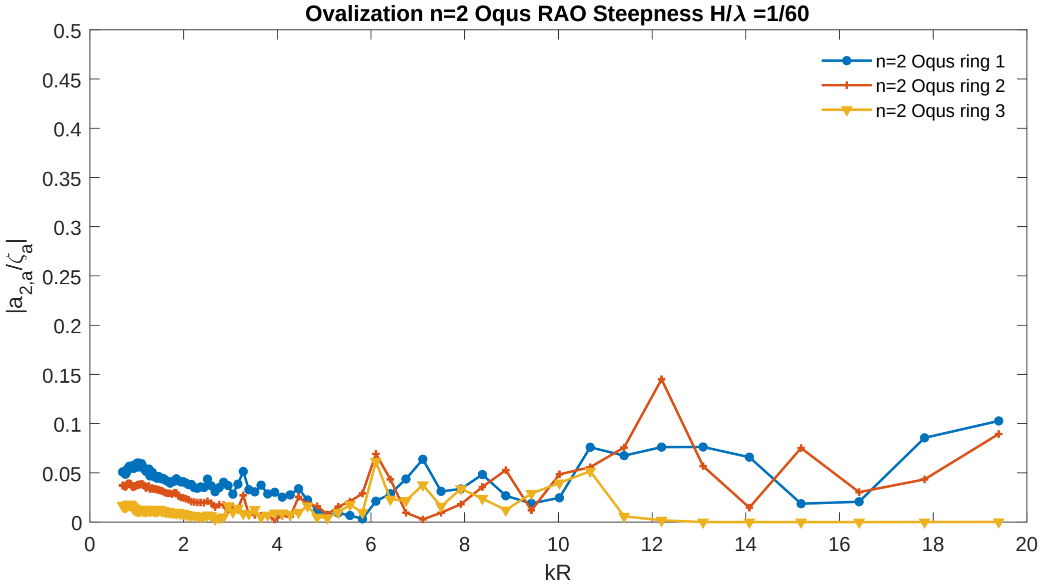

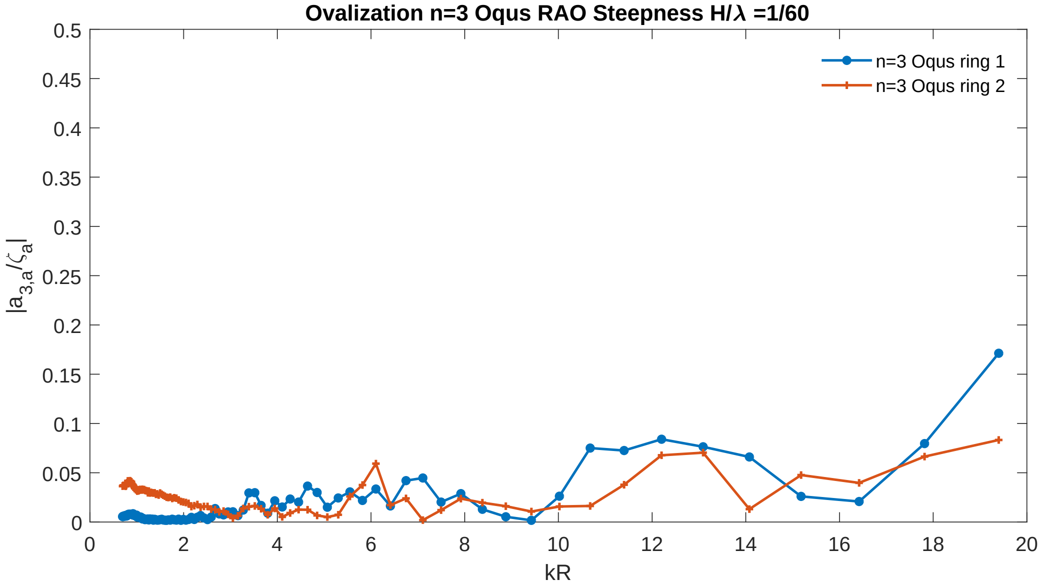

Figure 4.12: Horizontal ovalization RAO of multi-tori for ring 1, 2 and 3 when $n = 2$ in the left figure, and for ring 1 and 2 when $n = 3$ in the right figure. Wave steepness is $H/\lambda = 1/60$.

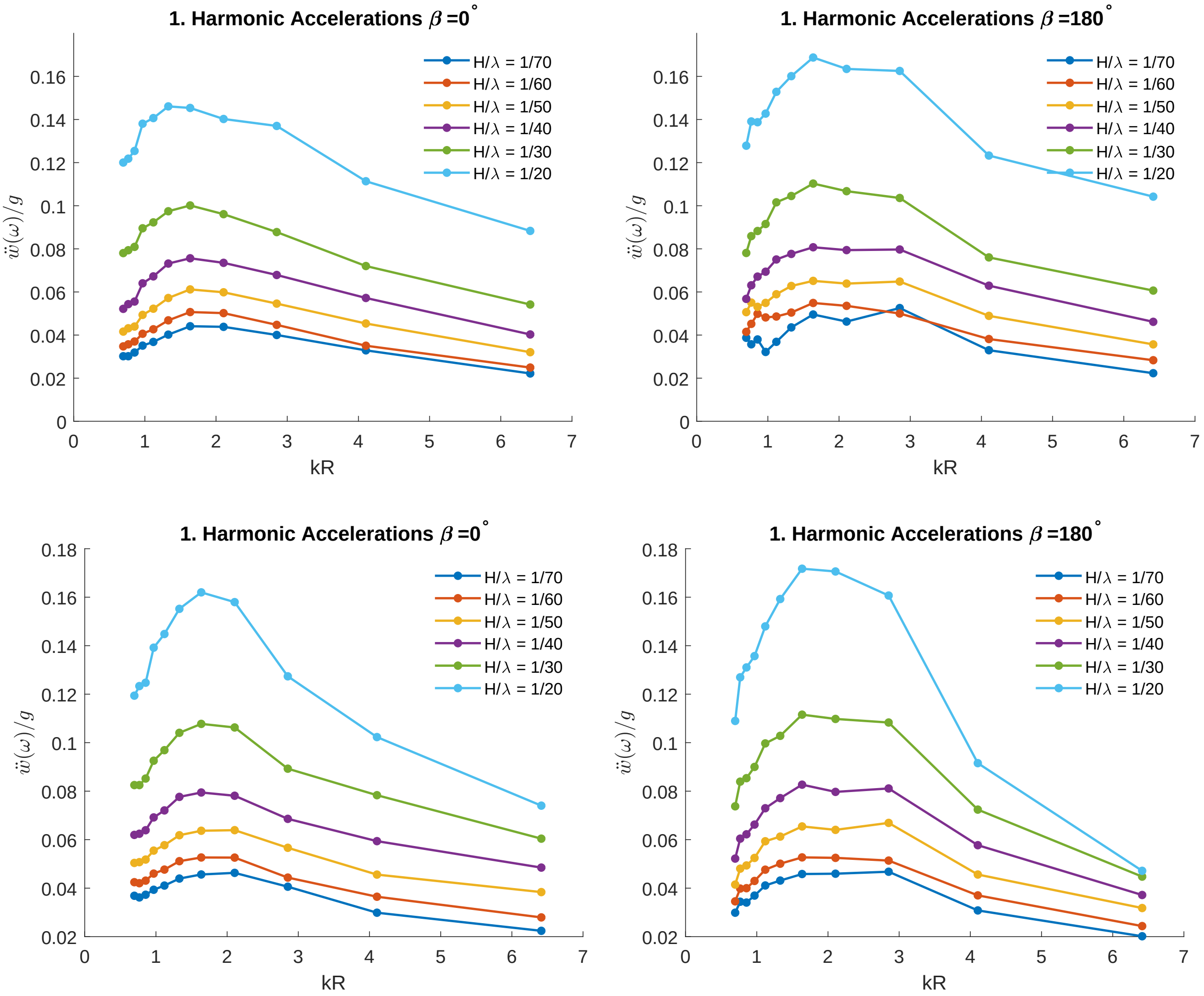

Figure 4.13: Experimental first harmonic accelerations for $\beta = 0^o$ and $\beta = 180^o$ at steepness $H/\lambda = 1/70$, $H/\lambda = 1/60$, $H/\lambda = 1/50$, $H/\lambda = 1/40$, $H/\lambda = 1/30$, $H/\lambda = 1/20$. The two uppermost figures show the results from the single-torus, and the two figures below show the results from the outermost ring of the multi-torus.

4.5.2 Second Harmonic Acceleration

Figure 4.14 shows the second harmonic accelerations for $\beta = 0^o$ and $\beta = 180^o$ on the single-torus and the multi-torus for varying wave steepnesses. The peaks at $kR \approx 1$ are much larger for the accelerometers at $\beta = 180^o$, and the multi-torus have a peak at $kR \approx 3$.

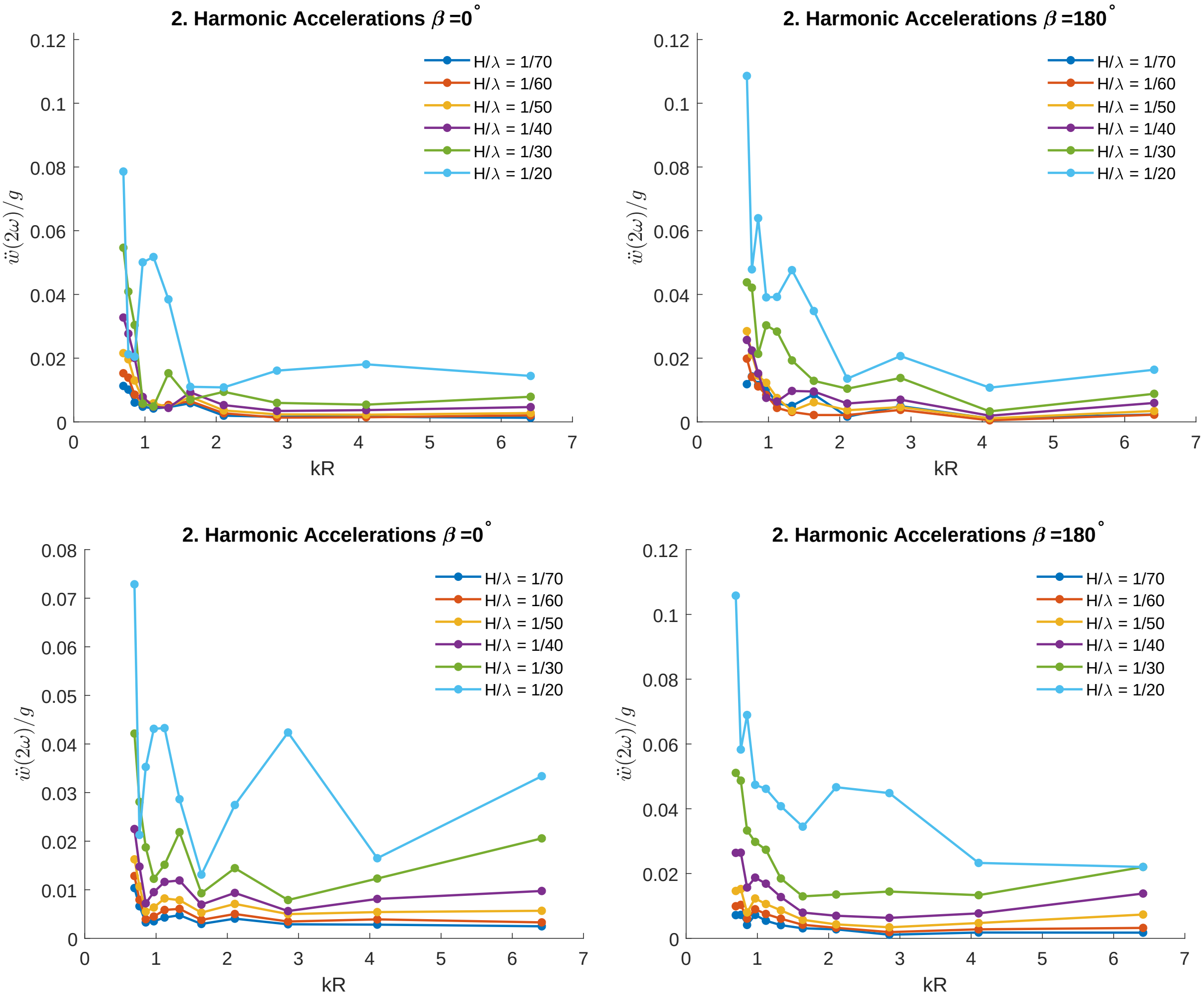

Figure 4.14: Experimental first harmonic accelerations for $\beta = 0^o$ and $\beta = 180^o$ at steepness $H/\lambda = 1/70$, $H/\lambda = 1/60$, $H/\lambda = 1/50$, $H/\lambda = 1/40$, $H/\lambda = 1/30$, $H/\lambda = 1/20$. The two uppermost figures show the results from the single-torus, and the two figures below show the results from the outermost ring of the multi-torus.

4.6 Mooring-line Forces

Figure 4.15 shows the difference $F = F_{0^o} + F_{315^o} - F_{225^o} - F_{135^o}$ between the non-dimensional mooring-line tension in the fore and aft of the single-torus and the multi-torus, where F_{0^o} and F_{315^o} are tensions in the fore, and F_{225^o} and F_{135^o} are tensions in the aft. This is thus the total force contribution on the models. The mooring-line tension forces F are each made non-dimensional by mg, where m is the total mass of the model. The relative forces acting on the single-torus are larger than those acting on the multi-torus for both steepnesses. It is possible that this is due to the larger added mass of the multi-torus absorbing some of the wave forces.

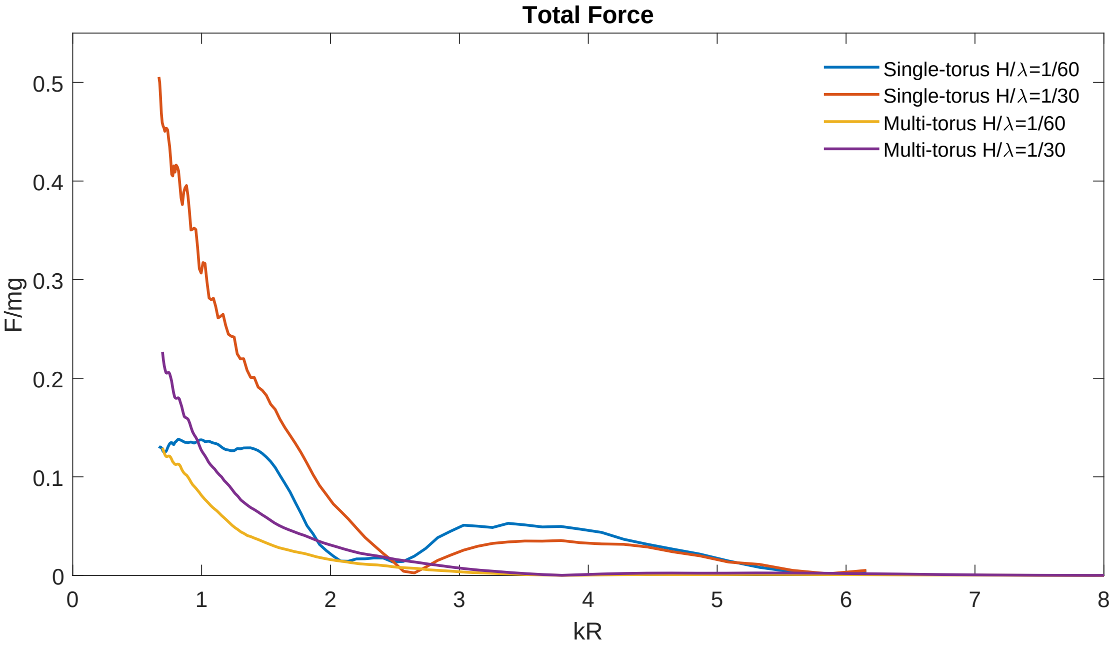

Figure 4.15: Experimental mooring-line force difference between fore and aft of acting on the mooring lines of the model for different wave steepnesses $H/\lambda = 1/70$, $H/\lambda = 1/60$, $H/\lambda = 1/50$, $H/\lambda = 1/40$, $H/\lambda = 1/30$ and $H/\lambda = 1/20$

Figure 4.16 shows how the variations in the wave steepnesses increases the total mooring-line forces by a large amount for $kR < 3$, which is expected as the wave forces causes the mooring-line tensions in the fore as the multi-torus is forced backwards with the wave, and the mooring-line tensions in the aft are caused by the restoring forces in the springs as the multi-torus moves to its original position.

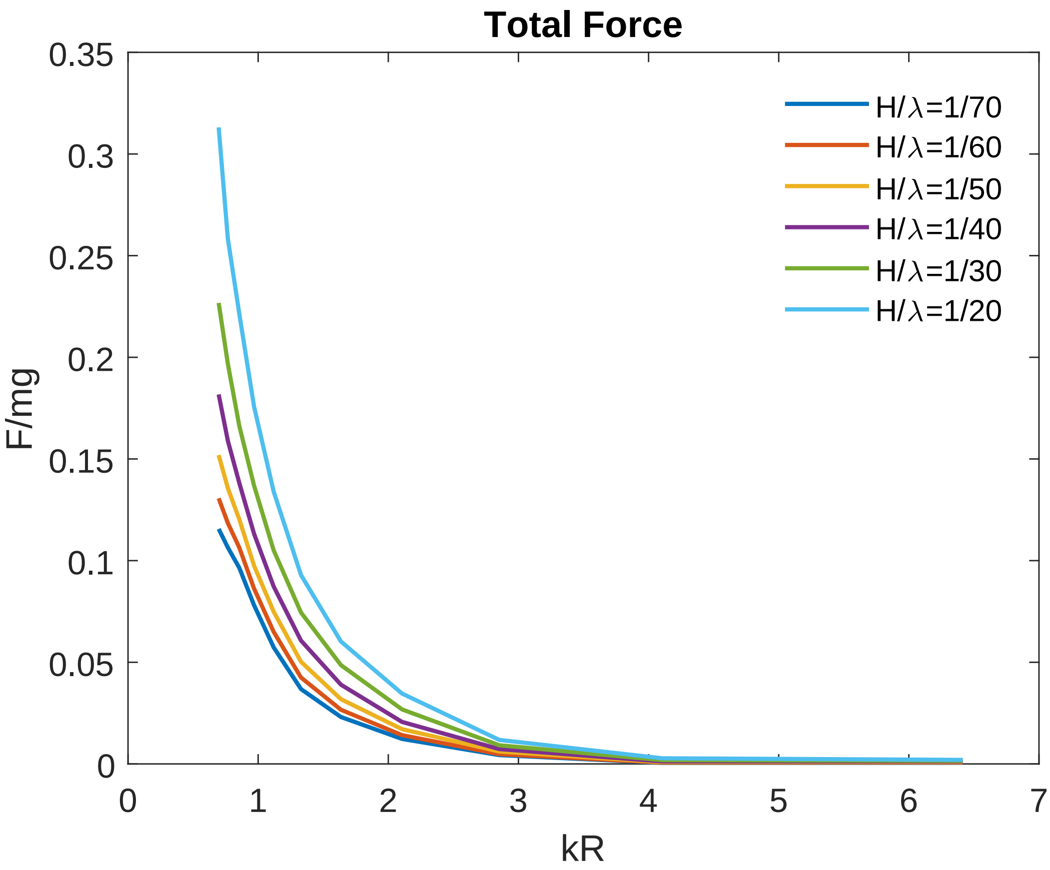

Figure 4.16: Experimental mooring-line force difference between fore and aft of acting on the mooring lines of the model for different wave steepnesses $H/\lambda = 1/70$, $H/\lambda = 1/60$, $H/\lambda = 1/50$, $H/\lambda = 1/40$, $H/\lambda = 1/30$ and $H/\lambda = 1/20$

4.7 Overtopping in Regular Waves

Overtopping occured for wave periods $T \geq 10s$ with wave steepness $H/\lambda \geq 1/40$. For even higher wave steepness, $H/\lambda = 20$, there was some overtopping occuring for $T \geq 6s$, and for $H/\lambda = 1/10$ there was overtopping even for $T = 4.5s$. There was a clear tendency for the aft of the multi-torus to be subjected to overtopping for high wave periods with small wave steepness, this can be seen in Figure 4.17 where the wave is flowing over the two rings in the aft.

A time-series plot of a wave-series with $T = 14s$ and $H/\lambda = 1/40$ is presented in Figure 4.18. The motion of the aft, $\beta = 180^o$, of the multi-torus is slightly lower than the waves in steady state, which possibly correlates with the observed overtopping. It is also

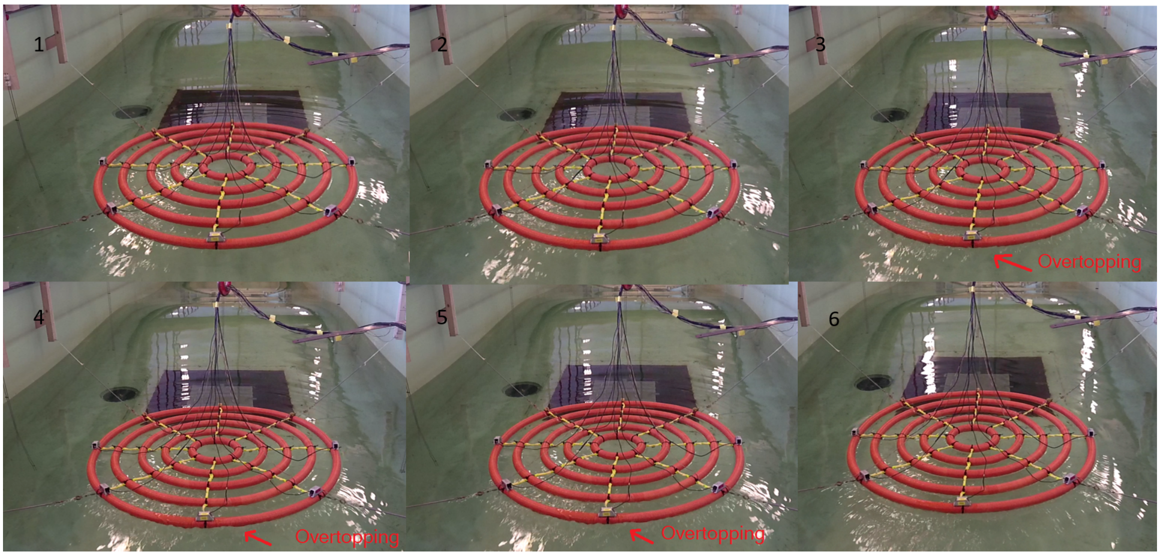

Figure 4.17: Model seen from the aft in regular waves with $T = 14s$ and $H/\lambda = 1/40$. Barely visible overtopping occurs at the aft of the two outermost rings.

interesting to note that there was no observed overtopping for this wave-series at the fore, $\beta = 0^o$, and the measured relative motion of the multi-torus is higher than the steady state waves.

Overtopping during waves with high wave steepness and low wave period showed a clear tendency of overtopping occuring first at the front of the outermost ring. This is the case for the wave-series with $T = 4.5s$ and $H/\lambda = 1/10$, seen in Figure 4.19, where overtopping only occured at the front. In Figure 4.20, a wave-series with $T = 5s$ and $H/\lambda = 1/10$ is shown. Here, wave overtopping occurs first at the front, then gradually it moves with the wave backwards. It is also possible to see how the water rises very high in the innermost ring for both these wave-series, but there are no sign of any strong sloshing there, neither between any of the rings.

Figure 4.21 shows the time-series plots of the vertical motion for the wave-series corresponding to Figure 4.20 and Figure 4.19. The vertical motion of the fore of the torus is lower than the wave amplitude for both wave periods, this suggests that the vertical motion relative to the wave amplitude is somewhat dependent on the wave steepness, and that by evaluating such a time-series one can get a pointer to whether or not there is a probability of overtopping happening. This is not certain however, and should possibly be further looked into. Appendix F shows multiple time-series. The correlation with overtopping is slightly ambigous.

An example of full structural overtopping is included in Figure 4.22. With $H/\lambda = 1/10$ and $T = 8s$, this corresponds to a significant wave height $H_s = 9.8$, which is much higher than this structure is supposed to withstand.

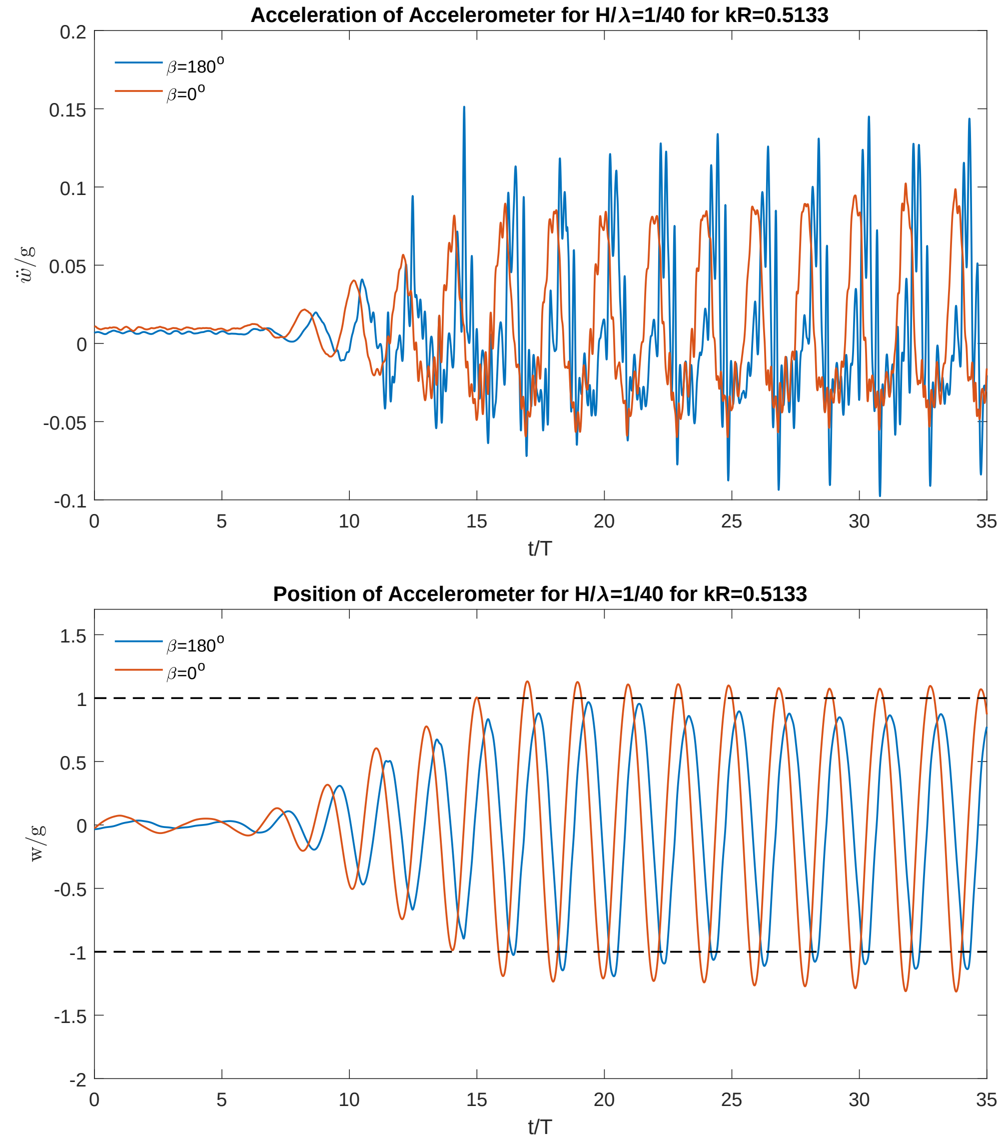

Figure 4.18: Both figures show time-series examples of experimental results from a wave series with $H/\lambda = 1/40$ at $kR = 0.5133$, i.e. $T = 14s$. Upper figure shows the non-dimensional acceleration $\ddot{w}$ at $\beta = 180^o$ and $\beta = 0^o$. Lower figure shows a time-series example of the non-dimensional motion w of the accelerometer at $\beta = 180$ and $\beta = 0^o$ relative to the incident wave ζ_a.

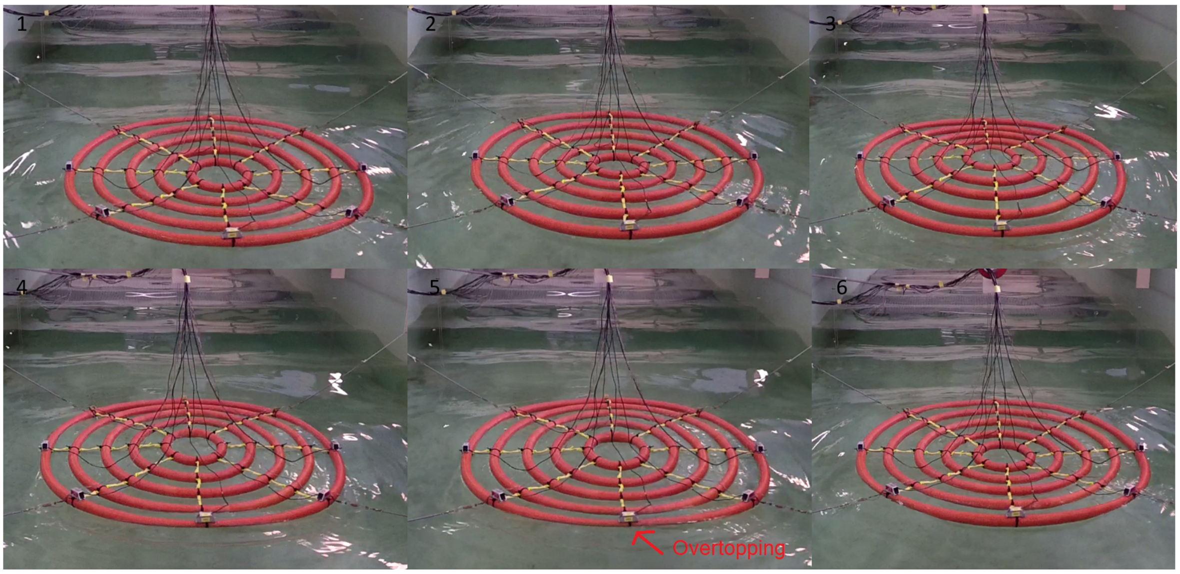

Figure 4.19: Model seen from the front in regular waves with $T = 4.5s$ and $H/\lambda = 1/10$. Overtopping occurs at the front only.

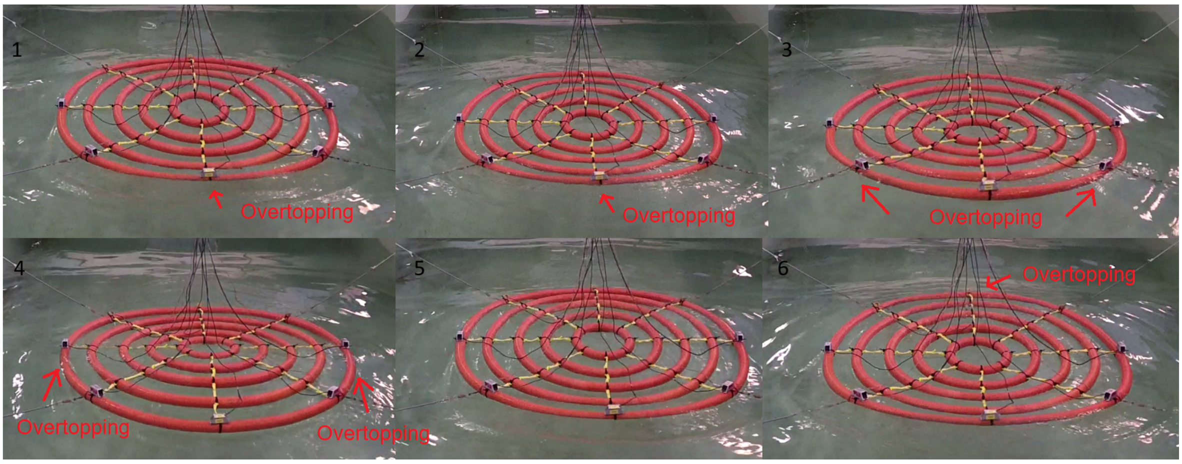

Figure 4.20: Model seen from the front in regular waves with $T = 5s$ and $H/\lambda = 1/10$. Overtopping occurs over the whole outer torus.

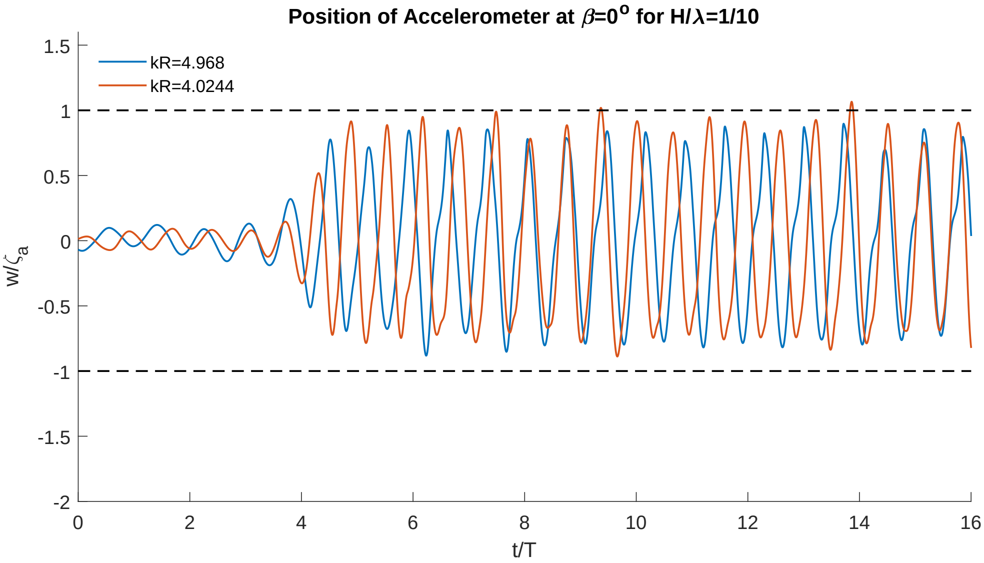

Figure 4.21: Time-series examples of the experimental non-dimensional motion w of the accelerometer at $\beta = 0^o$ relative to the incident wave ζ_a, acquired from a wave series with $H/\lambda = 1/10$ at $kR = 4.968$ and $kR = 4.0244$, corresponding to $T = 4.5s$ and $T = 5s$ respectively.

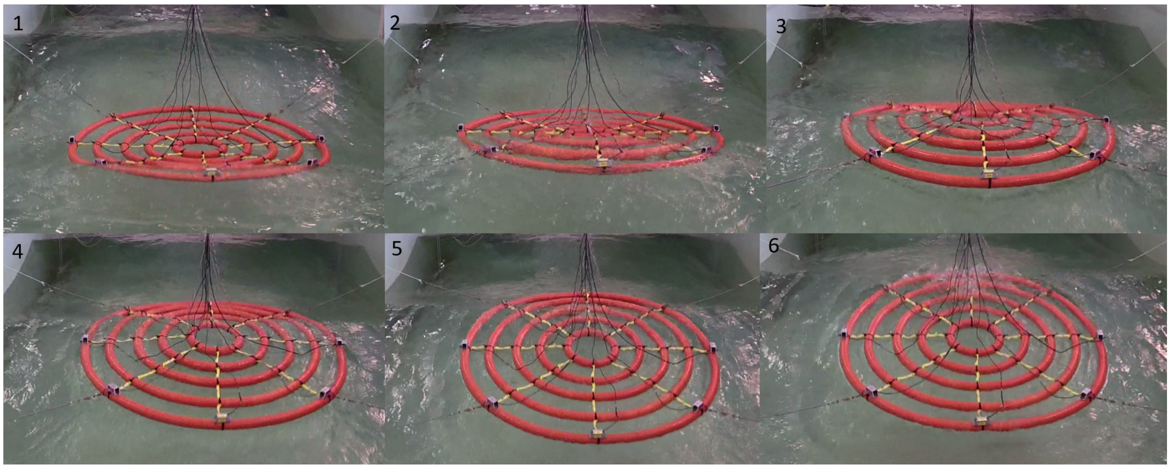

Figure 4.22: Model seen from the fore in regular waves with $T = 8$ and $H/\lambda = 1/10$. Overtopping occurs over the whole structure and it becomes partly submerged.

Chapter 5

Results and Discussion - Irregular Waves

In this chapter the results from the tests on the multi-torus in irregular waves are presented. The variables that have been varied during the tests are the peak wave period T_p and the significant wave height H_s, which are always referred to in the full-scale size. The results are presented as power spectral densities $S(\omega)$ plotted against the angular wave frequency ω. For results plotted against the non-dimensional wavenumber kR, the torus outer radius is $R = 0.51$. In Appendix E more results from the irregular wave tests are included.

5.1 Input Spectrum

The wave heights of the irregular waves generated were measured by the wave probes and the input spectrum thus refers to the power spectral density of the irregular waves over a time span.

5.1.1 Wave Spectrum

In Figure 5.1, the figure to the left shows the power spectral density of the irregular wave height measured by wave probe 1 for the largest H_s for each T_p tested, and the figure to the right shows the power spectral density of irregular waves with $T_p = 10s$ with varying H_s. The results are plotted together with the corresponding JONSWAP spectrums. There is a noticeable difference between the experimental results and the JONSWAP spectrums for larger significant wave heights, which is much less profound for irregular waves with smaller significant wave height. This indicates that larger waves are harder to sustain in the small towing tank, possibly because of waves breaking and viscous effects due to tank wall effects.

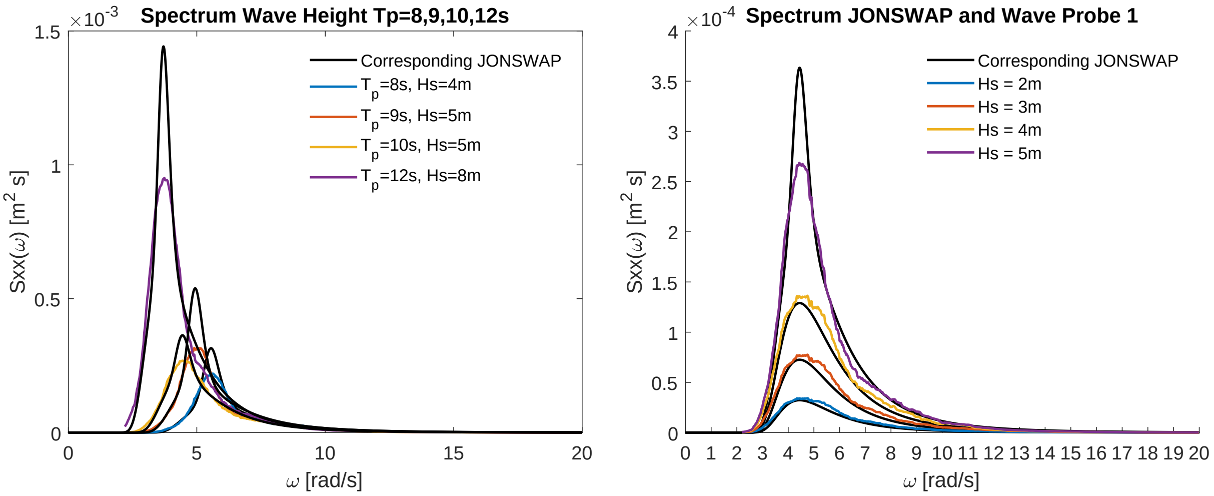

Figure 5.1: Figure to the left shows the experimental power spectral density for wave heights with peak wave period $T_p = 8, 9, 10, 12s$ and $H_s = 5m$ compared to the JONSWAP spectrum. Figure to the right shows the experimental power spectral density peak wave period $T_p = 10s$ and $H_s = 2, 3, 4, 5m$ with corresponding JONSWAP spectrum.

Figure 5.2 shows the power spectral density of the different wave probes in irregular waves with $T_p = 10s$ and $H_s = 5m$. For wave probe 3 and 5 the peaks are slightly lower, indicating that these two probes have not measured the correct wave height during the irregular wave tests.

5.1.2 Measured Significant Wave Height

For the different irregular wave series the input significant wave height H_{si} is increased linearly for each peak wave period. It is of interest to know if the measured significant wave height H_s increases linearly as well, and if it follows the linearity of the input H_{si}. The relation between the two is illustrated in Figure 5.3. The input H_{si} is compared to the measured H_s in the left figure, where H_s from the irregular waves is found by taking the standard deviation σ of the measured wave height and multiplying it by four. How much H_s deviates from H_{si} is then presented in right figure. It is seen that the measured H_s is close to increasing linearly, but it deviates from H_{si} in the range of $1.09 - 1.125$. This means that the measured irregular significant wave height is $9 - 12.5\%$ larger than the input significant wave height, and does not increase linearly.

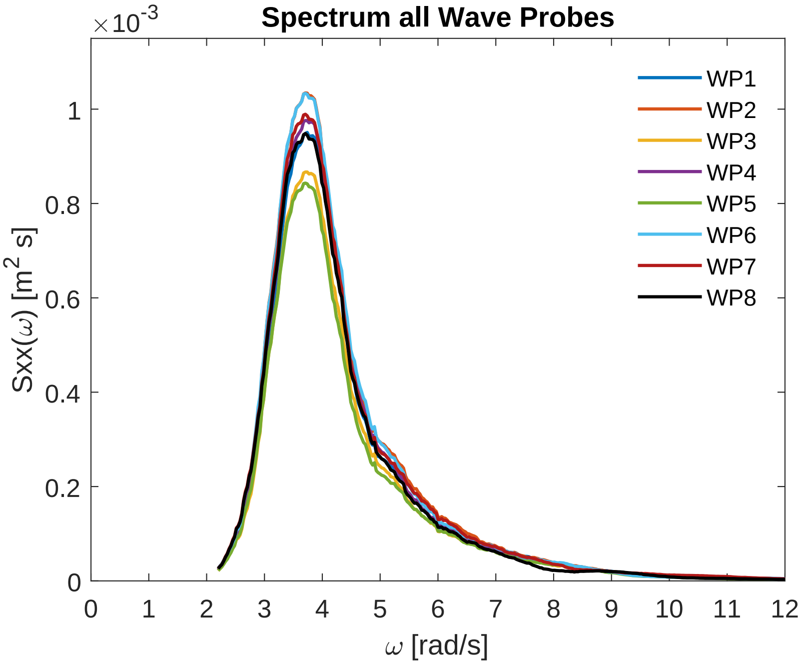

Figure 5.2: Power spectral density of irregular wave elevation measurements with $T_p = 10s$ and $H_s = 5m$ for different wave probes.

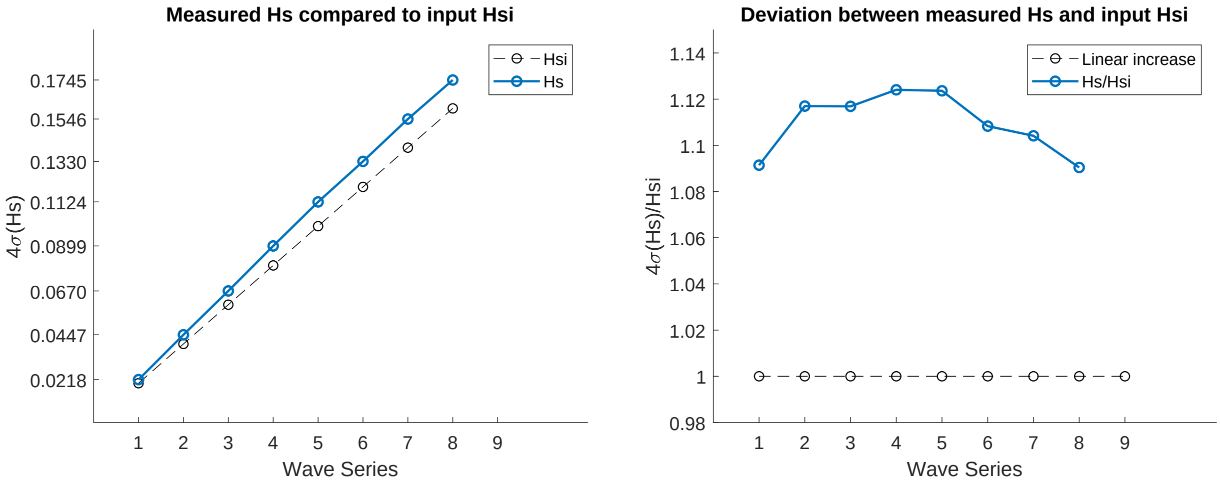

Figure 5.3: In the left figure the input H_{si} is compared to the measured H_s. In the right figure the ratio of deviation between H_s and H_{si} is compared to the case of full linearity for increase of significant wave height. The data is collected during a a wave series with $T_p = 12s$ and $H_s = 1, 2, 3, 4, 5, 6, 7, 8, 9m$ in full scale.

5.2 Response Spectrum

This section presents the spectral analysis of the response of the model to the input irregular waves.

5.2.1 Motion Spectrum

In Figure 5.4, the figure to the right shows the spectral densities of the z-positions of different motion capture markers during in an irregular wave field with $T_p = 10s$ and $H_s = 8m$. In the picture to the left the z-position of the markers on the outer ring of the multi-torus are shown. The results seems to indicate similarity of motion for markers positioned at symmetrically the same position relative to the incoming waves. At $\beta = 0^o$ and $\beta = 180^o$ the multi-torus is expected to be subjected to the largest amount of motion, and as seen in the figure the markers at these positions have the highest peaks. The markers at $\beta = 90^o$ and $\beta = 270^o$ are expected to be subjected to the least amount of motion due to their location on the sides, which is also found in the figure as they have the lowest peaks. The figure to the left shows the spectral densities of the motion capture markers positioned at $\beta = 180^o$ for each tori. The inner torus, ring 5, have the smallest peak. Ring 2 has the highest peak, which is 17% higher than the inner torus. The outermost torus, ring 1, only have the third highest peak.

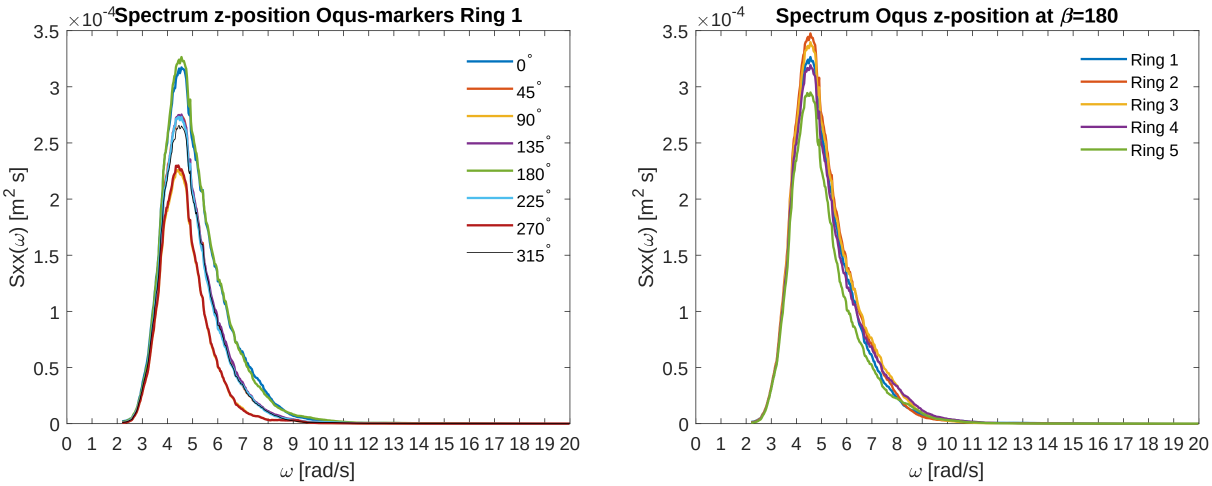

Figure 5.4: Figure to the left shows the spectral densities of the z-position of different motion capture markers in irregular waves with $T_p = 10s$ and $H_s = 8m$. The figure to the right shows the spectral densities of the z-position of motion capture markers placed at $\beta = 180^o$ for all the tori on the multi-torus in the same irregular wave-series.

5.2.2 RAO in Irregular Waves

The RAO measured by the accelerometers and the motion capture markers are shown in Figure 5.5. There seems to be some deviation between the measurements for higher significant wave height $H_s = 2m$ as seen in the figure to the right, which is in contrast to the results for the lower significant wave height $H_s = 2m$ shown in the right figure. This is the opposite observation as made in Chapter 4 for regular waves, where the motion capture camera seemed to have a difficulty observing the smaller movements of the markers created by smaller waves.

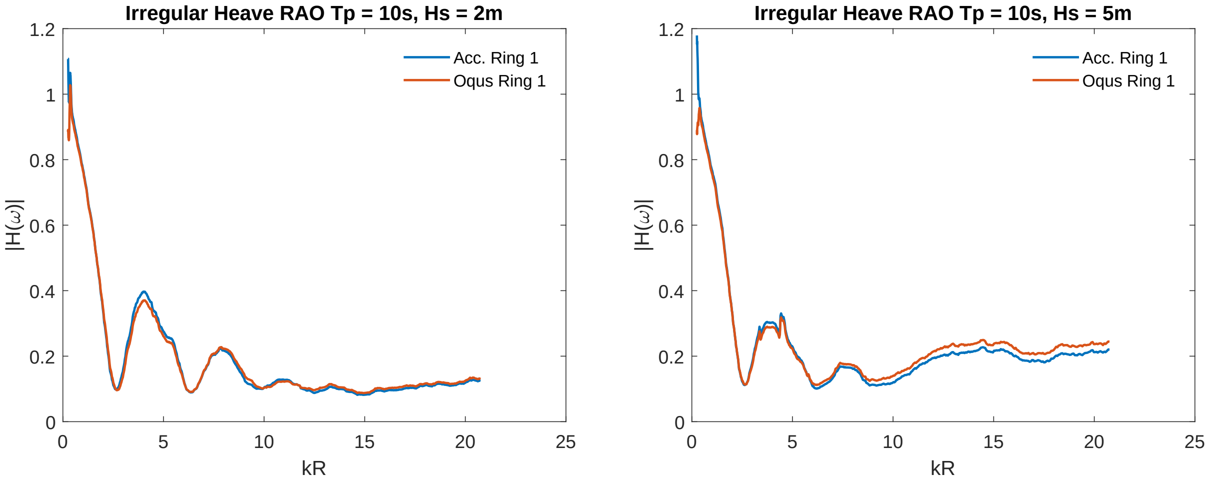

Figure 5.5: Experimental RAO results in heave for irregular waves for accelerometers and motion capture with peak wave period $T_p = 10s$. In the figure to the left $H_s = 2m$ and in the figure to the right $H_s = 5m$.

In Figure 5.6 the experimental RAO in irregular waves are compared to the experimental RAO in regular waves using accelerometers in heave, pitch, first flexible mode and second flexible mode. The wave-series for irregular waves had a $T_p = 9$ and a $H_s = 4m$, and the wave-series for regular waves had a $T = 9s$ and $H/\lambda = 1/40$, corresponding to $H_s = 4.21m$. The responses are somewhat in agreement, but the highs and lows of the RAO in irregular waves are reduced compared to the regular waves. The smoothing parameters used when analyzing the irregular wave tests are probably the main reason for this. However, it might be slightly related to the different frequencies of the irregular waves and the different natural frequencies of the different sized tori cancelling each other out and amplifying each other since the tori can interact through the elastic trusses, creating a motion closer to the mean without the more peaked highs and lows as seen in regular waves.

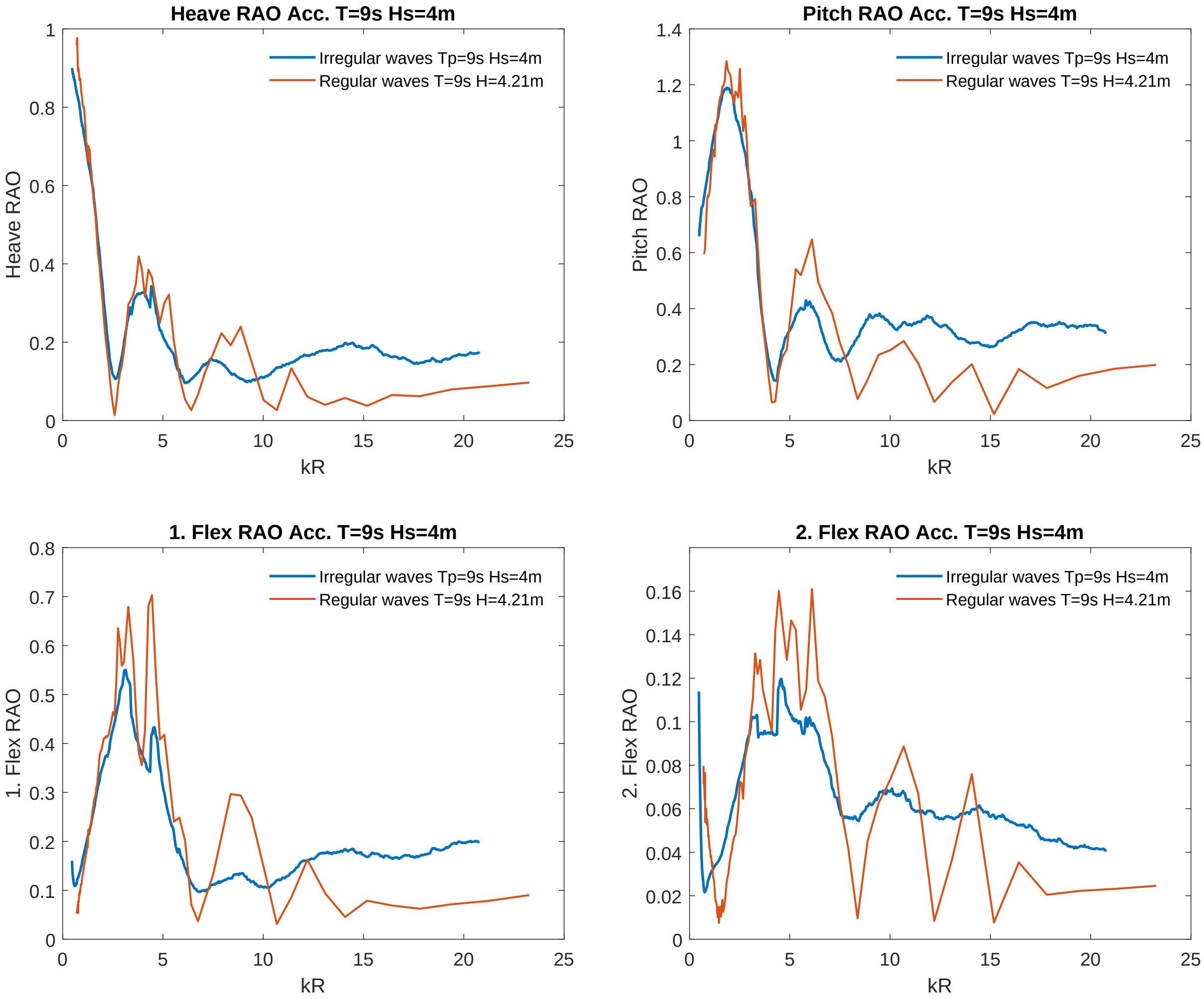

Figure 5.6: Experimental RAO in irregular waves compared to the experimental RAO in regular waves for the multi-torus using accelerometers in heave, pitch, first flexible mode and second flexible mode. Peak wave period $T_p = 9$ and $H_s = 4m$ for irregular waves. Wave period $T = 9s$, $H_s = 4.21m$ and wave steepness $H/\lambda = 1/40$ for regular waves.

Figure 5.7 shows how the RAO looks with a lower smoothing parameter in irregular waves with $T_p = 10s$ and $H_s = 5m$. The RAO is close to zero at $kR \approx 2.6$ in heave and $kR \approx 4$ in pitch. This indicates that the smoothing parameter has a large effect on the RAO-plots. In this study, it is the relative RAO-difference in different irregular wave conditions that have been the focus. Thus, smoother RAO-plots are preferred as these are easier to use for comparisons between plots.

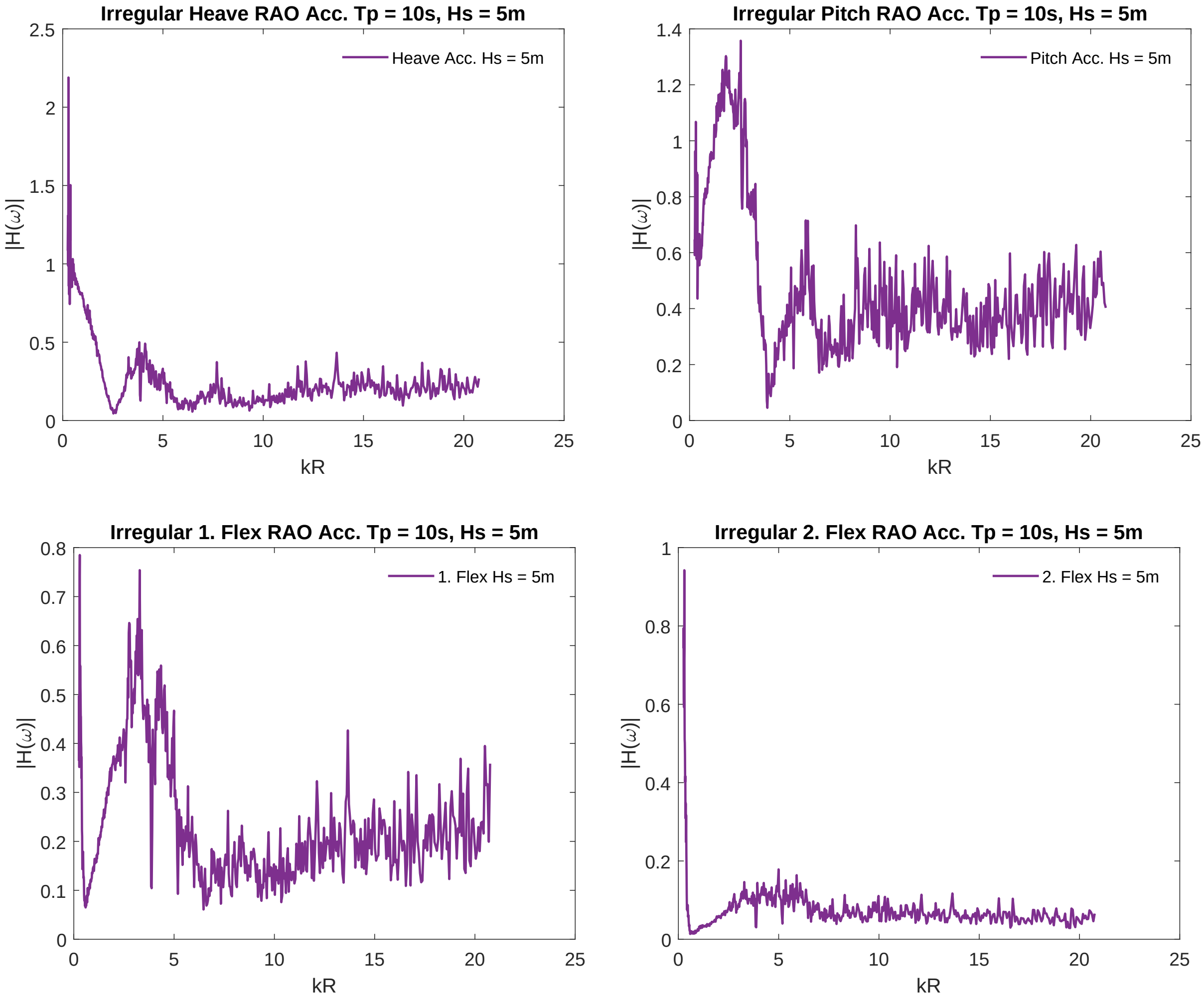

Figure 5.7: Unsmoothed experimental RAO results in heave, pitch, first flexible and second flexible mode measured with motion capture system in irregular waves with peak wave period $T_p = 10s$ and $H_s = 2, 3, 4, 5m$.

Figure 5.8 presents the RAO in the different modes for $T_p = 10s$ with $H_s = 2m$, $H_s = 3m$, $H_s = 4m$ and $H_s = 5m$, measured by the motion capture camera. The difference between the different significant wave heights are largest for smaller kR and for $kR \approx 4.8$, where the peak is slightly higher for $H_s = 2m$ and $H_s = 3m$.

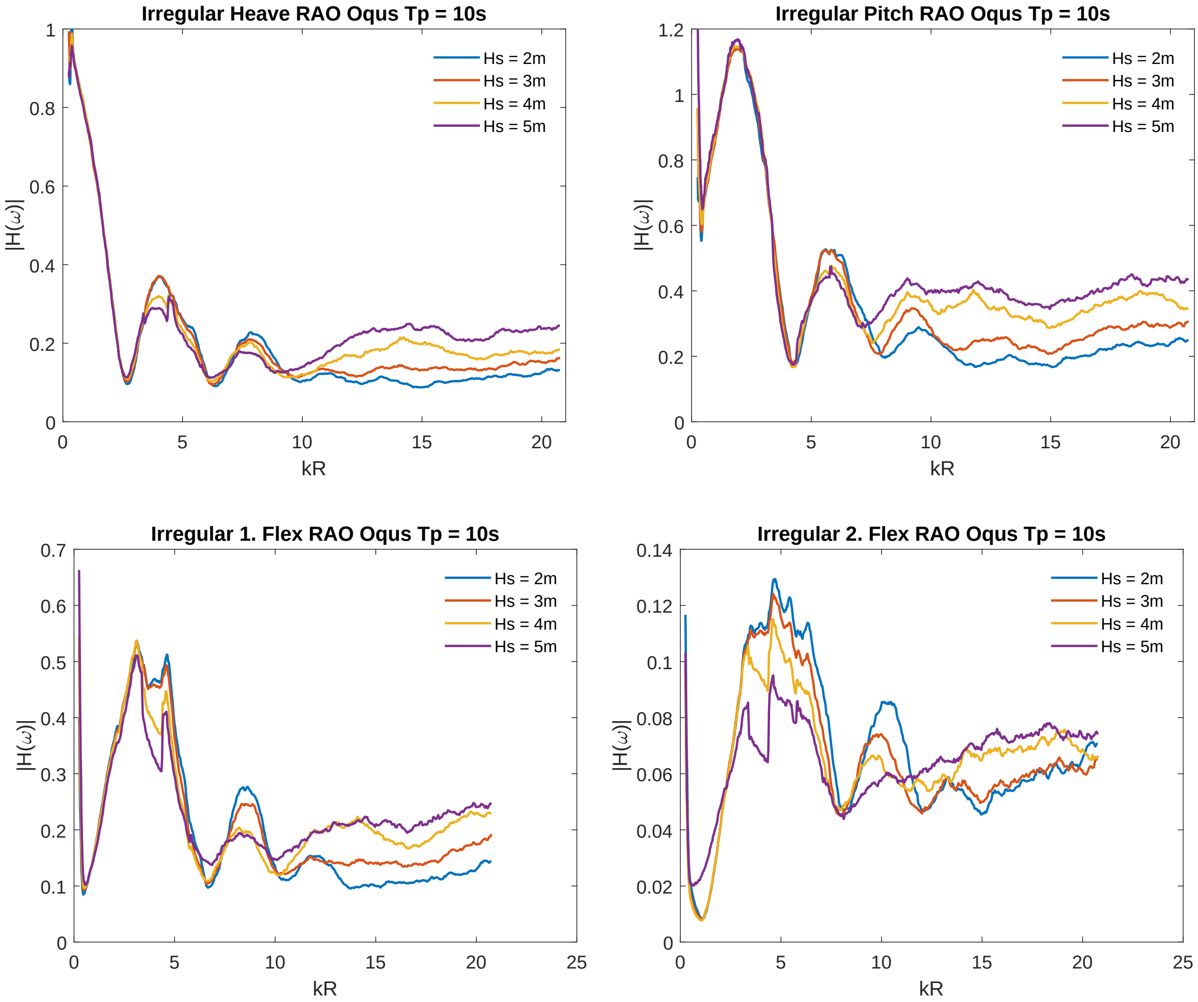

Figure 5.8: Experimental RAO results in heave, pitch, first flexible and second flexible mode measured with motion capture system in irregular waves with peak wave period $T_p = 10s$ and $H_s = 2, 3, 4, 5m$.

The RAO in irregular waves for the different tori are compared in Figure 5.9. The heave and pitch RAO of the two inner tori, ring 4 and ring 5, have very small peaks for $kR \approx 5$ compared to the other tori. The RAO in heave for Ring 3 also seems to be slightly reduced around this wavenumber. Ring 3, 4 and 5 have less motion capture markers than ring 1 and 2, which might explain this, but most likely this is an indication of how the motions of the inner tori are determined by motions of the outer tori through the elastic trusses for reasons previously mentioned in Chapter 4.

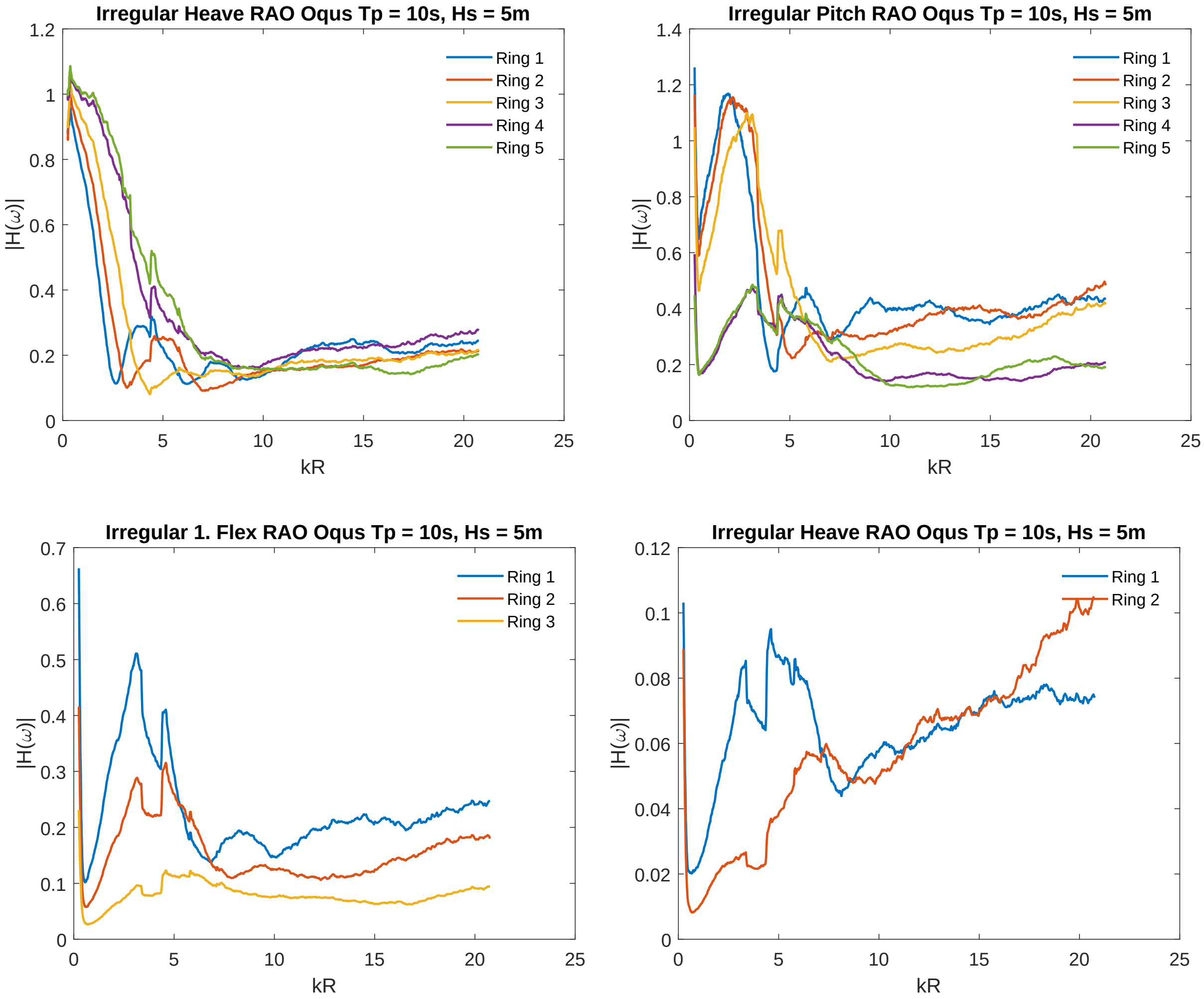

Figure 5.9: Experimental RAO results in heave, pitch, first and second flexible mode in using motion capture markers on ring 1, 2, 3, 4 and 5, in irregular waves with $T_p = 10s$ and $H_s = 5m$
.

5.2.3 Force Spectrum

The power spectral density of the forces measured at the mooring-lines fixed at $\beta = 135^o$, $\beta = 225^o$ and $\beta = 315^o$ on the multi-torus are given in Figure 5.10, 5.11 and 5.12, respectively. The force spectrum are given for irregular waves with $T_p = 12s$ and $H_s = 1, 2, 3, 4, 5, 6, 7, 8m$. The relative force in the fore and aft of the structure can then be seen. The mooring-line located at $\beta = 45^o$ is not included as its force ring was defect during the irregular tests. However, if symmetry in the force-distribution is assumed, the mooring-lines in the fore is exposed to much larger forces than the aft, creating a large total force, as was seen in the regular wave tests.

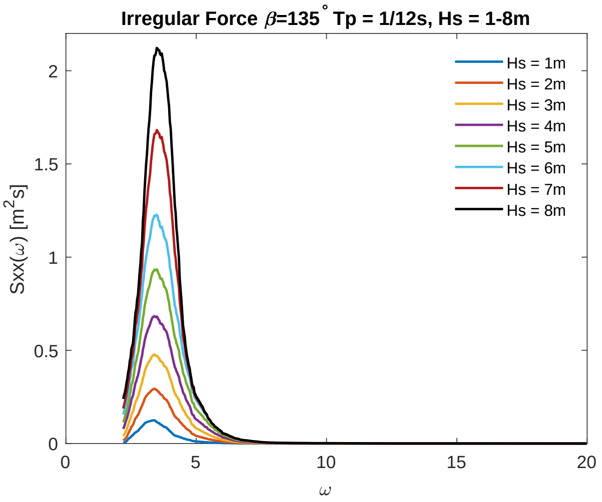

Figure 5.10: Power spectral density of forces in the mooring-line at $\beta = 135^o$ in irregular waves with $T_p = 12s$ and $H_s = 1, 2, 3, 4, 5, 6, 7, 8m$

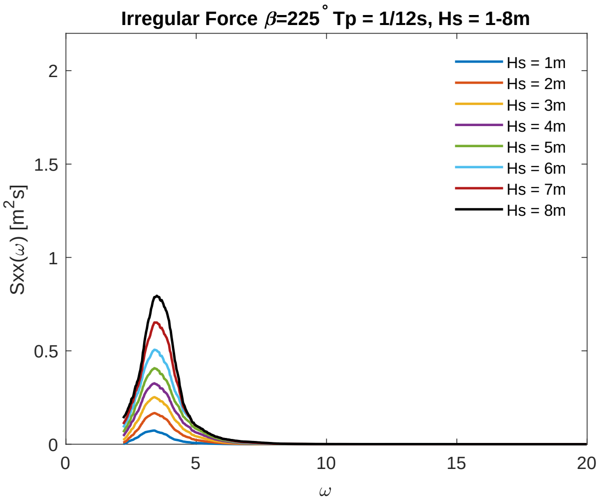

Figure 5.11: Power spectral density of forces in the mooring-line at $\beta = 225^o$ in irregular waves with $T_p = 12s$ and $H_s = 1, 2, 3, 4, 5, 6, 7, 8m$

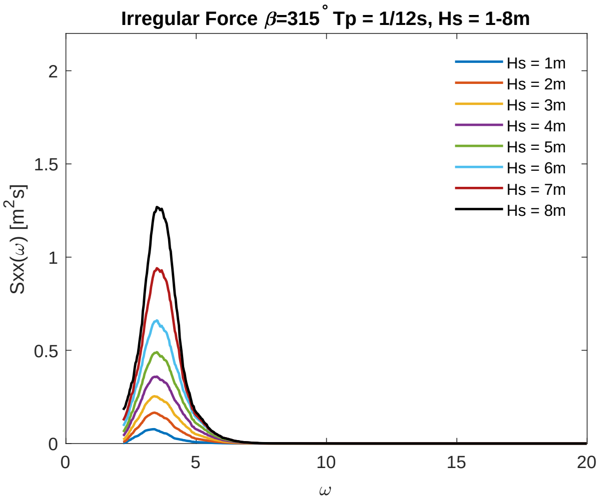

Figure 5.12: Power spectral density of forces in the mooring-line at $\beta = 315^o$ in irregular waves with $T_p = 12s$ and $H_s = 1, 2, 3, 4, 5, 6, 7, 8m$

5.3 Overtopping in Irregular Waves

Overtopping in irregular waves occured at random locations on the multi-torus, with a tendency of occuring more often at the fore of the structure and on the two outer tori. However, it did not follow the pattern observed for regular waves, where there was a clear tendency for where overtopping would occur. Overtopping was registered at relatively low peak wave periods and significant wave heights compared to regular waves, in Figure 5.13 it is shown how overtopping occurs at several different locations in waves with $T_p = 9s$ and $H_s = 3m$, corresponding to $H/\lambda \approx 1/43$. Overtopping occured for even lower peak wave periods and significant wave heights as well, but no systematic study on this was performed.

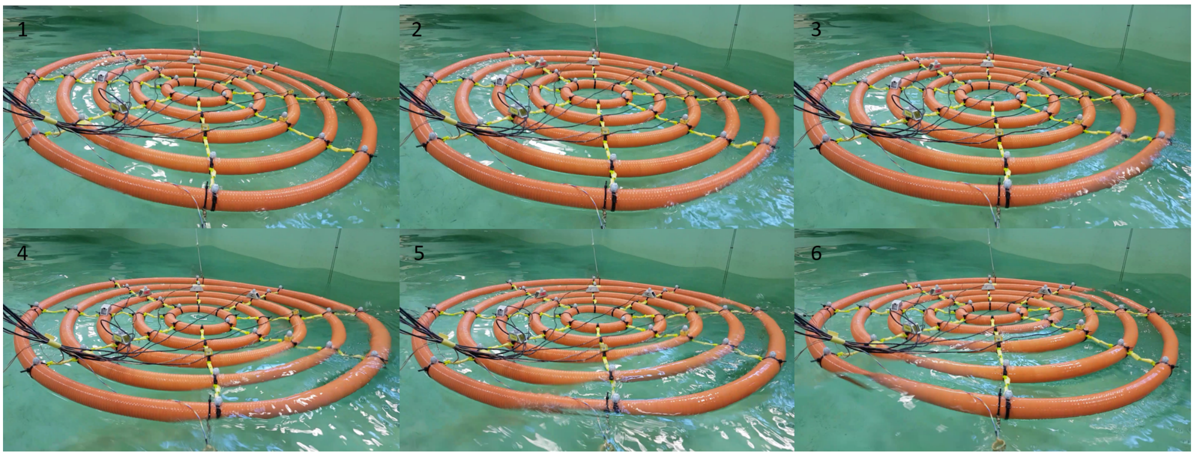

Figure 5.13: Overtopping occuring randomly on the multi-torus in irregular waves with $T_p = 9s$ and $H_s = 3m$

Figure 5.14 shows how overtopping occurs for $T_p = 9s$ and $H_s = 5m$ from an angle where a wave can be seen flowing over the side of the fore of the outer torus.

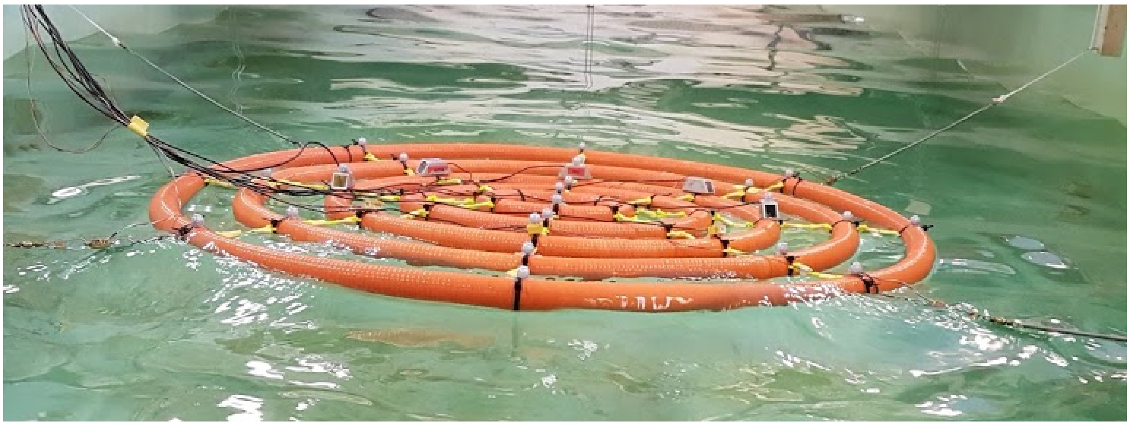

Figure 5.14: Overtopping waves seen flowing over the fore of the multi-torus in irregular waves with $Tp = 9s$ $Hs = 5m$

Chapter 6

Conclusion and Further Work

6.1 Summary of results

The RAO calculation based on the low-frequency slender-body theory and zero-frequency are in good agreement with the experimental RAO for the first three modes; heave, pitch and 1. flexible mode, for a single-torus for longer wave periods, i.e. with $kR < 10$. The fourth mode deviates the most, caused by the limited amount of eight measurement-points on the torus. The experimental RAO from the multi-torus also approximates the low-frequency slender-body theory for very long wave periods, i.e. $kR < 3.5$, when considering the first three modes. Comparing the different tori with the low-frequency theory, it was seen that the outer torus, ring 1, had the closest approximation to this theory, and that this agreement gradually decreased for the tori when moving towards the innermost torus, that thus had the least amount of agreement. This is most likely caused by the trusses between the tori, pulling the tori in different directions, slightly reducing their relative motion to the wave. The smaller tori are more vulnerable to this due to their lower mass and position between larger tori. The experimental RAO in surge showed that the relative motions of the smaller tori were larger than that of the two largest tori for $kR \approx 5.8$.

The first harmonic accelerations were smaller for the multi-torus than the single-torus for lower wave periods, $kR > 4$. For $2 \leq kR \leq 3$, the accelerations of the multi-torus were slightly larger. There was some tendency for both models to have a higher first harmonic acceleration at the aft than at the fore. The second harmonic accelelerations exhibited the same tendencies as the first harmonic accelerations, where accelerations for the multi-torus have peaks between $2 \leq kR \leq 3$.

The total mooring-line tension force in both regular and irregular increased for larger waves, and as expected, the force in the fore of the multi-tori was much larger than at the aft.

The instrumentation that was used to measure the vertical and horizontal response produced results that deviated slightly from one another. Accelerometers had more precise measurements for smaller waves than the motion capture system in regular waves, were more reliable, and easier to calibrate and use. However, the accelerometers weighed more than the motion capture markers, needed to be attached to cables and are much more expensive to acquire. Once the motion capture cameras are in place, any number of motion capture markers can be added at relatively low cost, and they are able to measure the motion in any direction, not just in one direction, like the accelerometers. The loss of data when a motion capture marker is submerged can also possibly be used to register the occurrence of overtopping.

Overtopping in regular waves occurred predominantly at the aft of the outermost tori for longer wave periods with relatively low wave steepness, and at the fore for high wave steepnesses and shorter wave periods. Time-series plot with the motions of the outer torus relative to the wave amplitude can possibly be used to predict overtopping, however not decisively. If the motions of the torus is smaller than the wave-amplitude in the positive z-direction, or if the motions of torus is larger than the wave-amplitude in the negative z-direction, this will indicate a chance for overtopping. There were no measurements on the forces in the overtopping waves. These forces is of high interest as they will be a determining factor when considering whether the forces are of such magnititude that they can threaten the integrity of the structure, and what counter-measures to overtopping can be considered. If the force are deemed small, overtopping on the sides can perhaps be avoided by encircling the structure with a water-stopping fence. If the forces are deemed large, it will perhaps be necessary to consider locating the structure at sites with calmer sea-conditions, or improving the structure somehow.

The experimental RAO in irregular waves deviated slightly from the RAO in regular waves, mainly by having smaller peaks and lows. This was attributed to the interactions between the tori due to the trusses and to the smoothing parameter ued when calculating the input and output spectrums. The RAOs were in good agreement for different significant wave heights for longer waves, with smaller variations for shorter waves. The RAO of the smaller tori showed that they had larger relative motions for shorter wave periods in heave, but smaller motions in pitch.

The RAO of the multi-torus showed satisfactory response relative to the waves. In both regular and irregular waves the multi-torus are able to move with the waves without exhibiting too many nonlinear effects.

6.2 Conclusion

The hydroelastic response of a semi-submerged multi-torus in different wave conditions have been investigated. Development of a floating solar island requires a platform capable of withstanding large wave motions, preferably by being sufficiently elastic to move in motion with the waves to minimize the wave-forces acting on the platform, and at the same time sufficiently rigid to carry the required weight and withstand the wave-forces. An elastic multi-torus have the desired properties to solve that problem, with the main concern being overtopping. No complete systematic study on overtopping was performed in regular and irregular waves, which registered every wave period, wave steepness and significant wave height overtopping occured in. However, there seemed to be little overtopping occuring within sea-conditions that the multi-torus can be expected to be located in. Slamming was not observed.

The elasticity of the tori and the trusses are decisive variables for the response of the structure, and thus far only one set of variables have been investigated. The results are also limited by not placing a deck on top of the multi-torus, which most likely will have a great effect on the response as well. However, this study on a more basic structure will hopefully alleviate any further work on developing a large floating solar island capable of operating in conditions offshore. The results from the multi-torus shows potential, but more work and research are needed to secure an additional steady supply of renewable energy from floating solar islands.

6.3 Recommendations for further work

There are a multitude of different aspects of the multi-torus that needs to be investigated to further develop a floating solar island based on the current design. Deriving a theoretical model of the multi-torus, possibly by expanding the low-frequency slender-body theory to include elastic trusses, is of great interest. A first step in that direction would be to build and test a numerical model of the multi-torus in a program based on the linear and second-order potential theory, such as WAMIT. The complexity of the structure and its motion in incident waves are difficult to recreate numerically. Modelling five tori where each have twenty flexible modes will result in a total of 20^5 modes when they are connected. A more comprehensive theoretical study on the trusses should be considered as well.

Further experimental studies where a deck is included are necessary. A flexible deck is the preferred option as this will not inhibit the flexible motion of the multi-torus. Most solar panels existing today are rigid, and placing rigid solar panels on a flexible deck will lead to certain complications. These might be overcome either by ingenious design, or by using flexible printed solar panels that are relatively new to the market. A large step in the right direction would also be to build a prototype of the floating solar island, and test it in the ocean. A more complete study on overtopping is also of interest. For both regular and irregular waves, the wave-sizes causing each overtopping should be systematically registered, preferably also registering the exact location on the multi-torus where it occurs. The forces in the overtopping waves should also be measured as they pass over the torus, to determine how critical the overtopping actually is. Depending on the forces, different counter-measures should be investigated.

Bibliography

Bishop, R. E. D., Bishop, R. E., and Price, W. (1979). *Hydroelasticity of ships*. Cambridge University Press.

Borvik, P. P. (2017). Experimental and numerical investigation of floating solar islands. Master's thesis, NTNU.

BPS, B. P. S. (2017). A history of the bruce nuclear site. http://www.brucepower.com/about-us/history/.

DNV (2011). Modelling and analysis of marine operations. *Offshore Standard*.

DNVGL (2017). Energy transition outlook 2017.

EIA (2017). International energy outlook 2017. U.S. Energy Information Administration.

Faltinsen, O. (1993). *Sea loads on ships and offshore structures*, volume 1. Cambridge university press.

Faltinsen, O. (2011). Hydrodynamic aspects of a floating fish farm with circular collar. In *Proceedings of the 26th International Workshop on Water Waves and Floating Bodies*.

Faltinsen, O. M., Landrini, M., and Greco, M. (2004). Slamming in marine applications. *Journal of Engineering Mathematics*, 48(3-4):187–217.

GBtimes, W. L. (2017). China's three gorges project increases power output in 2017. https://gbtimes.com/chinas-three-gorges-project-increases-power-output-in-2017.

Heller, S. and Abramson, H. N. (1959). Hydroelasticity: a new naval science. *Naval Engineers Journal*, 71(2):205–209.

IEA (2017). Key world energy statistics 2017. International Energy Agency.

Kristiansen, D. (2010). Wave induced effects on floaters of aquaculture plants.

Kristiansen, T. and Faltinsen, O. M. (2015). Experimental and numerical study of an aquaculture net cage with floater in waves and current. *Journal of Fluids and Structures*, 54:1–26.

Li, P. (2017). A theoretical and experimental study of wave-induced hydroelastic response of a circular floating collar.

Li, P. and Faltinsen, O. M. (2012). Wave-induced vertical response of an elastic circular collar of a floating fish farm. In *International Conference on Hydrodynamics (ICHD), St. Petersburg, Russia.*

Li, P., Faltinsen, O. M., and Greco, M. (2014). Wave-induced accelerations of a fish-farm elastic floater: Experimental and numerical studies. In *ASME 2014 33rd international conference on ocean, offshore and arctic engineering*, pages V007T05A004–V007T05A004. American Society of Mechanical Engineers.

Marichal, D. (2003). Cod-end numerical study. In *Third International Conference on Hydroelasticity in Marine Technology.*

Merriam-Webster, D. Definition of torus.

Newman, J. (1977). The motions of a floating slender torus. *Journal of Fluid Mechanics*, 83(4):721–735.

Steen, S. and Aarsnes, J. V. (2014). Experimental methods in marine hydrodynamics. *Lecture Notes. Department of Marine Technology, Norwegian University of Science and Technology, Trondheim, Norway.*

Appendix A

Theoretical Model of the Vertical Response

This appendix presents the theoretical model of the vertical response of a single-torus that was derived in Li and Faltinsen (2012) and later in its entirety in Li (2017), it is referred to as the *Low-frequency slender-body theory*. The theoretical model was plotted in MATLAB and was used to compare different experimental results. It is also presented in order to give a theoretical understanding of the wave-induced hydroelastic response of a torus.

A.1 Low-frequency slender-body theory

Low frequency corresponds to a wave length that is long relative to the cross-dimension of the torus. The low-frequency linear slender-body theory combined with a curved beam equation with tension for the floater shows that hydroelasticity is important and that 3D effects cause pronounced frequency-dependent hydrodynamic interaction on the scale of the torus diameter. The latter fact means that a strip theory and Morison's equation are not applicable.

A.1.1 Far-field flow description due to forced vertical motions

By utilizing potential theory, it is possible to represent the geometry of different bodies by a combination of sources, sinks and point dipoles within the body. In the far-field view the effects of the motion of the torus is seen from a distance, which means the details of the cross-section are not seen and the torus can be represented by a source distribution on the center-line of the torus Newman (1977).The velocity potential φ^F in the far field satisfies

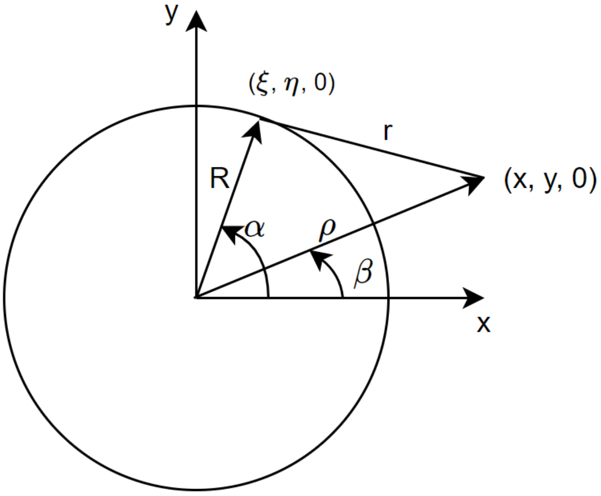

Figure A.1: Far field coordinates

the 3D Laplace equation with radiation conditions and the classical linear free-surface condition. The governing equation and the free-surface condition are

$$\nabla^2 \varphi^F \;=\; 0 \tag{A.1}$$

$$-k\varphi^F \;+\; \frac{\varphi^F}{\partial z} = 0 \; on \text{ z } \;=\; 0, \text{ k } \;= \omega^2/g \tag{A.2}$$

The far-field view and coordinate system of a single torus can be seen in Figure A.1. It is a Cartesian axis system with $z = 0$ at the mean free surface where the z-axis is pointing up, out of the water. (x, y, z) is the field point and $(\xi, \eta, 0)$. R is the torus radius, β is the angle and ρ is the distance to the field point from the origin. The field points x and y are defined by

$$\begin{aligned} x &= \rho cos(\beta) \\ y &= \rho sin(\beta) \end{aligned} \tag{A.3}$$

The coordinates $(\xi, \eta, 0)$ on the center line of the torus are given by

$$\begin{aligned} \xi &= Rcos(\alpha) \\ \eta &= Rsin(\alpha) \end{aligned} \tag{A.4}$$

n	0	1	2	3
K_n	0	2.0000	2.6667	3.0667

Table A.1: Values for K_n

Considering the forced vertical tour for each Fourier mode separately, the associated source density varies as $Q\ cos(n\alpha)\exp(-i\omega t)$ along the center line of the torus, and thus the far-field velocity potential can be described as

$$\varphi^F = \frac{Q\exp(-i\omega t)}{4\pi} R \int_0^{2\pi} cos(n\alpha) G(x,y,z;\xi,\eta,0) d\alpha \tag{A.5}$$

Here, Q is the density of the source distribution, i is a complex unit, n is the Fourier mode and $G(x,y,z;\xi,\eta,0)$ is the Green function which can be divided into three parts. We know that the Green function can be divided into three parts that can be solved separately.

$$G(x,y,z;\xi,\eta,0) = G_1 + G_2 + G_3 \tag{A.6}$$

As this function and the derivations of it are long and complex, they are left out but the details can be seen in Li (2017).

By solving the first term $G_1(x,y,z;\xi,\eta,0)$ of the Green function, an expression ϕ_I^F for the limiting case of $\omega \rightarrow 0$, also known as the zero-frequency theory, is obtained, as seen in Faltinsen (1993). The expression for the wave potential from the first term is as follows

$$\begin{aligned} \varphi_{I1}^F &= \frac{Q\exp(-i\omega t) cos(n\beta)}{\pi} \left[ln\left(\frac{8R}{r'}\right) - K_n \right] \\ K_n &= \frac{1}{2\sqrt{2}} \int_0^{2\pi} \frac{1 - cos(n\mu)}{\sqrt{1 - cos(\mu)}} d\mu \\ &= 2\left(1 + \frac{1}{3} + \frac{1}{5} + ... + \frac{1}{2n - 1}\right), \ n \geq 1 \end{aligned} \tag{A.7}$$

Here R is the radius of the torus, r is the radius of the cross-section of the torus and $\mu = \alpha - \beta$ is used for simplification. Values for K_n can be seen in Table A.1. This solution gives an approximate solution to the response of the torus, but it does not include the wave radiation from the torus, thus the other terms of the Green function must also be solved.

By solving the second term $G_2(x,y,z;\xi,\eta,0)$ the following equation is obtained

$$\begin{aligned}\varphi_{I2}^F &= \frac{Q\exp(-i\omega t)cos(n\beta)}{\pi}(1+kz)kR\pi^2 \\ &\times\left\{-J_n(kR)Y_n(kR)-\frac{1}{\pi R}|y'|+i[J_n(kR)]^2\right\}\end{aligned} \tag{A.8}$$

The variables $J_n(kR)$ and $Y_n(kR)$ are the first and second kind Bessel function respectively and $y' = \rho - R$. The third and last term $G_3(x, y, z; \xi, \eta, 0)$ is then solved and we find the following expression

$$\begin{aligned}\varphi_{I3}^F &= \frac{Q\exp(-i\omega t)}{\pi}cos(n\beta) \\ &\times\left\{-\frac{k\pi R}{4}(1+kz)\int_0^{2\pi}\mathbf{H}_0(kc)|_{\rho=R}cos(n\mu)\ d\mu\right. \\ &+\frac{\pi^2}{2}(1+kz)kR\left[J_n(kR)Y_n(kR)+\frac{1}{\pi R}|y'|\right] \\ &\left.-k|z|\left[ln\left(\frac{8R}{r'}\right)-K_n+1\right]+k\left(\frac{\pi}{2}|y'|-\theta y'\right)\right\}\end{aligned} \tag{A.9}$$

Here $\mathbf{H}_0$ is the Struve function of zero order. Having solved all three terms of the Green function it is now possible to combine them in a expression for the total far-field velocity potential, *i.e.*

$$\begin{aligned}\varphi_I^F &= \frac{Q\exp(-i\omega t)}{\pi}cos(n\beta) \\ &\times\left\{(1-k|z|)\left[ln\frac{8c}{r'})-K_n\right]-k|z|-k\theta y'\right. \\ &+(1+kz)kR\pi^2\left\{-\frac{1}{2}J_n(kR)Y_n(kR)+i[J_n(kR)]^2\right\} \\ &\left.-\frac{k\pi R}{4}(1+kz)\int_0^{2\pi}\mathbf{H}_0(kc)|_{\rho=R}cos(n\mu)d\mu\right.\end{aligned} \tag{A.10}$$

A.1.2 Near-field solution and matching with far-field solution

In the near-field view the details of the cross-section of the torus are seen. The draught of the section is assumed to be equal to the radius c of the cross-section. For the near-field velocity potential φ^N the governing equation is the 2D Laplace equation in the cross-sectional plane, with linearized boundary conditions, and where the free-surface and body-boundary condition are

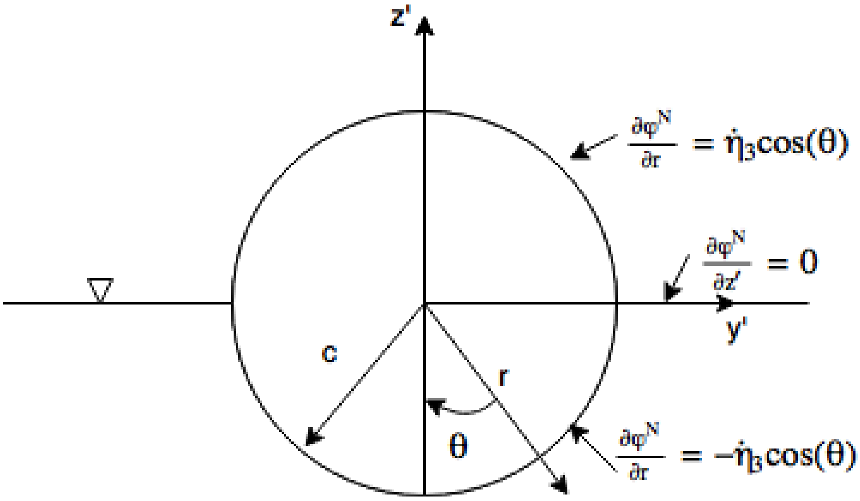

Figure A.2: Near field coordinates

$$-k\varphi^N + \frac{\partial\varphi^N}{\partial z'} = 0 \; on \; z' = 0 \tag{A.11}$$

$$\frac{\partial\varphi^N}{\partial r'} = -\dot{a}_n cos(n\beta) cos(\theta) \; on \; r' = a, \; z \le 0 \tag{A.12}$$

The near-field view and coordinate system of a single torus can be seen in Figure A.2. r is the radial distance from the center of the section and a local Cartesian and a local polar coordinate system with the coordinates (y', z') and (r, θ) are defined as

$$\begin{aligned} y' &= r \; sin(\theta) \\ z' &= r \; cos(\theta) \end{aligned} \tag{A.13}$$

To obtain the near-field velocity potential a series of infinite fluid multipoles are combined in order to satisfy the linearized free-surface condition and the symmetry condition. Due to a source singularity at the center of the circular cylinder, the Green function representing a 2D wave source, is also added. These equations are given in greater detail in Li (2017). The velocity potential can then be described as

$$\begin{aligned} \phi^N \;&=\; \dot{a}_n\; cos(n\beta) \\ &\times \Bigg\{ A_0 \Bigg\{ (1+kz') \left[ln\left(\frac{8R}{r'}\right) \;-\; K_n \;+\; C_n \right] \;+\; kz' \;-\; ky'\theta \Bigg\} \\ &+ \sum_{m=1}^{\infty} A_{2m} \left[\frac{cos(2m\theta)}{r'^{2m}} \;+\; \frac{k\; cos(2m-1)\theta}{(2m-1)r'^{2m-1}} \right] \end{aligned} \tag{A.14}$$

The constant K_n and C_n are introduced to match the near-field solution with the far-field solution. C_n is found by setting the expression for the far-field potential equal to the near-field potential, which results in the following expression

$$\begin{aligned} C_n \;&=\; \pi\; kR\; \Bigg\{ -\frac{\pi}{2}\; J_n\;(kR)\; Y_n\;(kR) \;+\; i\;\pi\;\left[\; J_n\;(kR)\;\right]^2 \\ &\qquad -\frac{1}{4}\int_0^{2\pi} \mathbf{H}_0\; kR\sqrt{2(1\;-\;\cos\mu)}\;)\; cos(n\mu)\; d\mu\Bigg\} \end{aligned} \tag{A.15}$$

Furthermore, A_0 and A_{2m} are complex unknowns that can be determined from the body boundary conditions seen in Eq. A.12, resulting in the following equation

$$A_0 \Bigg\{ k\; cos\theta \left[ln\; \left(\frac{8R}{c}\right) \;-\; K_n \;+\; C_n \right] \;- \tag{A.16}$$

This can be solved by numerical methods at given values of θ when $0 \leq \theta \leq \pi/2$. Compared to the aforementioned zero-frequency theory, the results are consistent for low frequencies. However, due to the additional terms in the equation, it is applicable to a broader frequency range, but it is not valid for high frequencies.

Added mass and damping

To find the 2D added mass a_{33}^n and damping b_{33}^n for mode n, the linearized hydrodynamic pressure force due to the pressure term $-\rho\partial\varphi^N/\partial t$ is integrated over the mean wetted surface of the cross-section. This pressure term is found by differentiating the near-field velocity potential φ^N for vertical motion mode n with respect to t. The forcing motion is the harmonic velocity of the cross-section $\dot{a}_n cos(n\beta)$ for mode n. The hydrodynamic pressure is found by multiplying it with the cross-section radius c and the negative z'-component of the body normal vector $cos\theta$, and then integrated over $\theta = -\pi/2$ to $\theta = \pi/2$. This leads to a expression for added mass and damping loads in z'-direction per unit length on the torus due to the forced motion of mode n. The 2D vertical force thus becomes

$$f_3 \;=\; -\rho \int_{-\pi/2}^{\pi/2} \frac{\partial \varphi^N}{\partial t} cos(\theta) c \; d\theta \;=\; f_3^N \ddot{a}_n \; cos(n\beta) \tag{A.17}$$

Integrating the equation analytically yields the following expression

$$\begin{aligned} f_3^N = -\rho a \Bigg\{ A_0 \left\{ \left(2 - \frac{1}{2}\pi k c\right) \left[ln\left(\frac{8R}{c}\right) - K_n + C_n \right] - \frac{3}{4}\pi k c \right\} \\ + A_2 \frac{\pi k}{2c} - \sum_{m=1}^{\infty} A_{2m} \frac{2cos(m\pi)}{a^{2m}(4m^2-1)} \end{aligned} \tag{A.18}$$

From formal definition of the 2D vertical added mass and damping coefficients we know that

$$f_3^{addedmass+damping} \;=\; -a_{33}^{(n)} \ddot{a}_n cos(n\beta) \;-\; b_{33}^{(n)} \dot{a}_n cos(n\beta) \tag{A.19}$$

Thus, it is shown that

$$\begin{aligned} f_3^{addedmass+damping} \;&=\; f_3^N \ddot{a}_n cos(n\beta) \\ \left(i\omega a_{33}^{(n)} \;-\; b_{33}^{(n)}\right) \dot{a}_n cos(n\beta) \;&=\; \left[i\omega \mathbf{Re}\left(f_3^N\right) \;+\; \omega \mathbf{Im}\left(f_3^N\right)\right] \dot{a}_n cos(n\beta) \end{aligned} \tag{A.20}$$

Which leads to the following expressions for 2D vertical added mass and damping

$$a_{33}^{(n)} = -\mathbf{Re}(f_3^N) \tag{A.21}$$

$$b_{33}^{(n)} = -\omega \mathbf{Im}(f_3^N) \tag{A.22}$$

In turn, these expressions can be used to determine the generalized added mass and damping coefficients of the torus associated with mode n by

$$\begin{aligned} A_{33}^{(n)} \;&= a_{33(n)} \; R \int_0^{2\pi} \; cos^2(n\beta) \; d\beta \\ B_{33}^{(n)} \;&= b_{33(n)} \; R \int_0^{2\pi} \; cos^2(n\beta) \; d\beta \end{aligned} \tag{A.23}$$

A.1.3 Wave potential

Using linear wave theory for deep water gives $k = \omega^2/g$. Deep water implies $h > \lambda/2$, where h is the water depth and $\lambda = 2\pi/k$ is the wave length. We also assume long wave theory where the waves are assumed to be much longer than the cross-sectional diameter of the torus, $\lambda/c >> 1$. Since mode superposition will be used to calculate the response of the torus, it is possible to express the wave forces as a Fourier sum involving Besssel functions. Therefore, utilizing a complex wave potential is preferable, which is expressed as

$$\varphi_0 \;=\; \frac{g\zeta_a}{\omega}\exp(kz \;+\; ikx \;-\; i\omega t) \tag{A.24}$$

The wave elevation is found by differentiating ϕ_0 with respect to time and inserting the expression in the dynamic linear condition $g\zeta \;+\; \frac{\partial}{\partial t}$ on $z = 0$. The wave elevation ζ is then expressed as

$$\zeta \;=\; i\zeta_a\exp(ikx \;- i\omega t) \tag{A.25}$$

It is the real part of the expression that has physical meaning, which also applies for later complex expressions in this text.

A.1.4 Generalized vertical excitation forces and Response Amplitude Operators

The vertical excitation force f_3^{excit} consists of the linear Froude-Kriloff force f^{FK} and the linear diffraction force f^D. The linear Froude-Kriloff force is due to the undisturbed dynamic pressure over the wetted surface and can be found be integrating the undisturbed dynamic pressure over the exact wetted surface where both the torus motion and wave elevation are accounted for. The diffraction force is due to the to added mass and water particle acceleration and can be calculated according to linear theory.

Linear Froude-Kriloff force

The undisturbed incident dynamic pressure is calculated from

$$p^{FK} \;=\; -\rho\frac{\partial\phi_0}{\partial t} \;=\; \rho g\zeta_a i\exp(\;+ikx \;+\; o\omega t),\; where\; x \;=\; Rcos(\beta) \tag{A.26}$$

Since mode superposition will be used to calculate the response of the torus, it is practical to express the wave forces as a Fourier sum involving Bessel functions, as seen below

$$\exp(ikR\ cos(\beta) \;=\; J_0(kR) \;+\; \sum_{m=1} 2i^m J_m(kR)\ cos(m\beta) \tag{A.27}$$

Denoting the mean wetted cross-sectional surface of the torus S_C, and given that for one torus the following expression can be used

$$-\int_{SC} (1 \;+\; kz)n_3\ ds \;=\; c\int_{-\pi/2}^{\pi/2} (1 \;-\; kc\ cos\theta)cos\theta\ d\theta) \;=\; 2c(1 \;-\; \pi kc/4) \tag{A.28}$$

the integration of the dynamic pressure over the wetted surface to find the Froude-Kriloff force is approximated as

$$\begin{aligned} f_3^{FK} \;&=\; -\int_{-\pi/2}^{\pi/2} p^{FK} n_3 c\ d\theta \;=\; i\rho g\zeta \left[J_0(kR) \;+\; \sum_{m=1}^{\infty} 2i^m J_m(kR) cos(m\beta) \right] \\ &=\; \times b_w(1 \;-\; \pi kc/4) \exp(-i\omega t) \end{aligned} \tag{A.29}$$

Linear Diffraction force

The linear diffraction force can be found by solving a boundary value problem with forced oscillations minus the vertical wave particle velocity and acceleration, Newman (1977). The 2D diffraction force is then $a_{3\zeta} a_{33}^{(m)} \;+\; w_\zeta b_{33}^{(m)}$ at $z \;=\; z_m$. Here, z_m is a weighted z-coordinate of the torus which can be approximated at $z_m = -4c/3\pi$. w_ζ and a_z are the vertical velocity of the incident waves and vertical particle acceleration found from the following equations

$$\begin{aligned} w_\zeta \;&=\; \frac{\partial \varphi_0}{\partial z} = \;-\;\omega\zeta_a \exp(kz_m \;+\; ikx_{CL} \;-\; i\omega t) \\ &= \;-\;\omega\zeta_a \exp(kz_m \;-\; i\omega t)\left[J_0(kR) \;+\; \sum_{m=1} 2i^m J_m(kR)\ cos(m\beta) \right] \end{aligned} \tag{A.30}$$

and

$$\begin{aligned} a_{3\zeta} \;&=\; \frac{\partial^2 \varphi_0}{\partial z \partial t} = i\omega^2\zeta_a \exp(kz_m \;+\; ikx_{CL} \;-\; i\omega t) \\ &= i\omega^2\zeta_a \exp(kz_m \;-\; i\omega t)\left[J_0(kR) \;+\; \sum_{m=1} 2i^m J_m(kR)\ cos(m\beta) \right] \end{aligned} \tag{A.31}$$

The vertical diffraction force per unit length are thus given as

$$\begin{aligned} f_3^D \quad &= \zeta_a \exp(z_m \; - \; i\omega t) \left[J_0(kR) \left(-i\omega^2 a_{33}^{(0)} \; + \; \omega b_{33}^{(0)} \right) \right. \\ &+ \sum_{m=1}^{\infty} \; 2i^m J_m(kR) \left(-i\omega^2 a_{33}^{(m)} \; + \; \omega b_{33}^{(m)} \right) \; cos(m\beta)] \end{aligned} \tag{A.32}$$

A.1.5 Curved beam equation with axial stiffness

The generalized Euler-Bernoulli beam equation can be used to predict the vertical motion w of the torus. Accounting for curvature and axial stiffness and inserting the restoring coefficient, wave excitation forces and forces due to added mass and damping , the equation can be expressed as

$$\begin{aligned} &m\frac{\partial^2 w}{\partial t^2} + \rho g b_w + EI\frac{\partial^4 w}{\partial s^4} + \frac{EI}{R^2}\frac{\partial^2 w}{\partial s^2} - \frac{\partial}{\partial s}\left(T_{as}\frac{\partial w}{\partial s} \right) \\ &= f_3(s)^{addedmass+damping} + f_3(s)^{waveexcit} + f_3^{moorings} \end{aligned} \tag{A.33}$$

where the vertical velocity and acceleration are $\frac{\partial^2 w}{\partial t^2}$ and $\frac{\partial^2 w}{\partial s^2}$, respectively. The unit for each term in the equation is N/m. m is the mass of the torus per unit length, EI is the bending stiffness, t is the time and s is the spatial coordinate that goes along the center line of the torus. The term $\rho g b_w$, where $b_w = 2c$, is the general 2D hydrodynamic restoring term for one torus and is caused by the change of the buoyancy force due to the motion w. The bending stiffness term $\frac{EI}{R^2}\frac{\partial^2 w}{\partial s^2}$ is a consequence of curvature effect of the torus, and is needed in addition to $EI\frac{\partial^4 w}{4}$ in order to describe a rigid torus when $EI \to \infty$. $f_3^{waveexcit} = f_3^{FK} + f_3^D$ is the vertical wave excitation force on the torus per unit length of the torus. $f_3^{addedmass+damping}$ is the vertical added mass and damping force because of vertical acceleration of the torus. $f_3^{moorings}$ denotes the vertical component of the mooring line forces that formally must be expressed in terms of Dirac delta functions since it is not uniformly distributed along the torus and T_{as} is the axial stiffness following from a static analysis of the moored torus.

The solution w is assumed to be a Fourier-series with orthogonal shape functions defined by $cos\ n\beta$, where $n = 1, 2, 3, ..\infty$.

$$w(\beta, t) = a_0(t) + \sum_{n=1}^{\infty} a_n(t) cos\ n\beta = \left(a_{0,a} + \sum_{n=1}^{\infty} a_{n,a} cos\ n\beta \right) e^{-i\omega t} \tag{A.34}$$

$$\dot{w} = \dot{a}_0 + \sum_{n=1}^{\infty} \dot{a}_n cos\ n\beta \tag{A.35}$$

$$\ddot{w} = \ddot{a}_0 + \sum_{n=1}^{\infty} \ddot{a}_n cos\ n\beta \tag{A.36}$$

since $\frac{\partial}{\partial s} = \frac{\partial}{R\partial\beta}$ we can rewrite and find

$$\frac{\partial^2 w}{\partial s^2} = \frac{1}{c^2}\frac{\partial^2 w}{\partial \beta^2} = \sum_{n=1}^{\infty} \frac{n^2}{c^2} a_{n,a} cos\ n\beta \tag{A.37}$$

$$\frac{\partial^4 w}{\partial s^4} = \frac{1}{c^4}\frac{\partial^4 w}{\partial \beta^4} = \sum_{n=1}^{\infty} \frac{n^4}{c^4} a_{n,a} cos\ n\beta \tag{A.38}$$

Here, $a_0(t)$ and $a_n(t)$ are the time dependent Fourier coefficients, and $a_{0,a}(t)$ and $a_{n,a}(t)$ are the amplitudes of the Fourier coefficients which can be complex numbers, thus taking care of the phase angle between the load and the response. By substituting the expressions for the derivatives into the beam equation, and multiplying each term with the orthogonal function $cos\ m\beta$ where $m = 1, 2, ..\infty$, and then integrating the equation around the center line of the torus, which is done by multiplying the equation with the torus radius R and integrating from $\beta = 0$ to $\beta = 2\pi$, we now obtain the following expression

$$\begin{aligned}
&\int_0^{2\pi} m_{2D} \left(\ddot{a}_0 + \sum_{n=1}^{\infty} \ddot{a}_n cos\ n\beta \right) cos(m\beta)R \\
&+ \rho g b_w \left(a_0 + \sum_{n=1}^{\infty} a_n cos\ n\beta \right) cos(m\beta)R \\
&+ \frac{EI}{R^4} \left(\sum_{n=1}^{\infty} (n^4 - n^2) a_{n,a} cos\ n\beta \right) cos(m\beta)R \\
&+ \frac{T_{as}}{R^2} \left(\sum_{n=1}^{\infty} n^2 a_{n,a} cos\ n\beta \right) cos(m\beta)Rd\ d\beta \\
&= \int_0^{2\pi} \left(f_3^{FK} + f_3^{D} + f_3^{addedmass+damping} + \sum_{i=1}^{8} T_{p,3}\delta(\beta - \beta_i) \right) cos(m\beta)Rd\beta
\end{aligned} \tag{A.39}$$

$$\int_0^{2\pi} cos\ n\beta\ cos\ m\beta d\beta \begin{cases} = 0, & n \neq m \\ = 2\pi, & n = m = 0 \\ = \pi, & n = m = 1, 2, .. \end{cases} \tag{A.40}$$

$T_{p,3}$ is the vertical component of pre-tension of the mooring lines, β_i describes the attachment positions between the mooring lines and torus and δ is the Dirac-delta function. The modal equations for the first mode, n = 0 and the n-th mode then have to be described to be able to find the vertical motion w of the torus, leading to the following expressions

$$\begin{aligned}&\Big(m + a_{33}^{(0)}\Big)\ddot{a}_0 + b_{33}^{(0)}\dot{a}_0 + \rho g b_w a_0 = \frac{1}{2\pi}\int_0^{2\pi}\sum_{i=1}^{8} T_{p,3}\delta(\beta-\beta_i)d\beta + \\ &\Bigg[\bigg(1-\frac{\pi kc}{4}\bigg)\rho g b_w - (\omega^2 a_{33}^{(0)} + i\omega b_{33}^{(0)}\bigg)\exp(kz_m)\zeta_a J_0(kR) i \exp(-i\omega t)\end{aligned} \tag{A.41}$$

$$\begin{aligned}&(m + a_{33}^{(m)}\ddot{a}_m + b_{33}^{(m)}\dot{a}_m + \left[\rho g b_w + \frac{EI}{R^4}(m^4 - m^2)\right] a_m \\ &\quad + \frac{1}{\pi R^2}\sum_{n=1}^{\infty}\sum_{i=1}^{8} n^2 T_{as}^{(i)}\int_{\beta_i}^{\beta_{i+1}} cos(n\beta)cos(m\beta)d\beta a_n = \\ &\quad \frac{1}{\pi}\int_0^{2\pi}\sum_{i=1}^{8} T_{p,3}\delta(\beta-\beta_i)cos(m\beta)d\beta \\ &\quad + \left[\left(1-\frac{\pi kc}{4}\right)\rho g b_w - \left(\omega^2 a_{33}^{(m)} + i\omega b_{33}^{(m)}\right)\exp(kz_m)\right] \\ &\quad \times \zeta_a 2 J_m(kR) i^{m+1}\exp(i\omega t), m = 1, 2,\end{aligned} \tag{A.42}$$

$$\begin{aligned}&\int_{\beta_i}^{\beta_{i+1}} cos(n\beta)cos(m\beta)d\beta \\ &\begin{cases} = \dfrac{(\beta_{i+1}-\beta_i)[m\ sin(m)cos(n) - n\ cos(m)\ sin(n)]}{m^2-n^2}, & n \neq m \\ = \dfrac{sin(2m\beta_{i+1} - sin(2m\beta_i) + 2m(\beta_{i+1}-\beta_i)}{4m}, & m = n\end{cases}\end{aligned} \tag{A.43}$$

The vertical displacements can now be obtained by inserting the solutions for a_0 and a_n in Eq. A.34. To solve the equations the solutions of a_0 and a_n are assumed to be harmonic with the same circular frequency ω as the incident waves

$$a_0 = a_{0,a}e^{i\omega t} \tag{A.44}$$

$$a_n = a_{n,a}e^{i\omega t} \tag{A.45}$$

The expressions for a_0 and a_n are then substituted into Eq. A.41 and A.42, and the equations are solved with respect to $a_{0,a}$ and $a_{n,a}$, that are complex values taking the phase angle between the waves and the response into account. Thus, when finding the response w by inserting the expressions for a_0 and a_n into equationA.34, the phase angle between the total response w and the waves will be accounted for. The expressions for the linear transfer functions for each mode is found by taking the absolute value of $a_{0,a}/\zeta_a$ and $a_{n,a}\zeta_a$. The transfer functions, giving the normalized response amplitudes for each wave circular frequency ω are

$$\left|\frac{a_{0,a}}{\zeta_a}\right| = \left|\frac{\left[\left(1-\frac{\pi kc}{4}\right)\rho g b_w - \left(\omega^2 a_{33}^{(0)} + i\omega b_{33}^{(0)}\right)\exp(kz_m\right] iJ_0(kR) + T_A}{-\omega^2\left(m + a_{33}^{(0)}\right) - i\omega b_{33}^{(0)} + \rho g b_w}\right| \tag{A.46}$$

$$\left|\frac{a_{n,a}}{\zeta_a}\right| = \left|\frac{\left[\left(1-\frac{\pi kc}{4}\right)\rho g b_w - \left(\omega^2 a_{33}^{(n)} + i\omega b_{33}^{(n)}\right)\exp(kz_m\right] 2i^{n+1}J_n(kR) + T_B}{-\omega^2\left(m + a_{33}^{(n)}\right) - i\omega b_{33}^{(n)} + \rho g b_w + \frac{EI}{R^4}(n^4 - n^2 + T_C}\right| \tag{A.47}$$

where the expressions of T_A, T_B and T_C are as seen below

$$\begin{aligned} T_A &= \frac{1}{2\pi}\int_0^{2\pi}\sum_{-=1}^{8} T_{p,3}\partial(\beta \ - \ \beta_i)\ d\beta \\ T_B &= \frac{1}{\pi}\int_0^{2\pi}\sum_{-=1}^{8} T_{p,3}\partial(\beta \ - \ \beta_i) cos(m\beta)\ d\beta \\ T_C &= \frac{1}{\pi R^2}\sum_{n=1}^{\infty}\sum_{i=1}^{8}\ n^2 T_{as}^{(i)}\int_{\beta_i}^{\beta_{i+1}}\ cos(n\beta)cos(m\beta)\ d\beta \end{aligned} \tag{A.48}$$

Appendix B

JONSWAP Spectrum

The equation for the JONSWAP spectrum $S_j(\omega)$ is given by DNV (2011)

$$S_j(\omega) = \frac{5}{16} A_\gamma H_s^2 \omega_p^4 \exp\left(-\frac{5}{4}\left(\frac{\omega}{\omega_p}\right)^{-4}\right) \gamma^{\exp\left(-0.5\left(\frac{\omega-\omega_p}{\sigma\omega_p}\right)^2\right)} \tag{B.1}$$

The deciding variables are the significant wave height H_s and the peak wave period T_p, from which the rest of the variables are found as follows

A_γ = $1 - 0.287 ln(\gamma)$ normalizing factor
γ = non-dimensional peak shape parameter
  $\gamma = 5$ for $T_p/\sqrt{H_s} \leq 3.6$
  $\gamma = \exp\left(5.75 - 1.15 T_p/\sqrt{H_s}\right)$ for 3.6 ¡ $T_p/\sqrt{H_s} \leq 5$
  $\gamma = 1$ for $5 \leq T_p/\sqrt{H_s}$
H_s = significant wave height
ω_p = $2\pi/T_p$ angular spectral peak frequency
σ = spectral width parameter
  $\sigma = \sigma_a$ for $\omega \leq \omega_p$
  $\sigma = \sigma_b$ for $\omega > \omega_p$

where average values for the JONSWAP experiment data are $\sigma_a = 0.07$, $\sigma_b = 0.09$ can be used as average values

Appendix C

Wave-Series in Model Scale

Table C.1: Test conditions for regular waves in model scale

T [s]	$\lambda [m]$	$H/\lambda = 1/60$ H [m]	$H/\lambda = 1/40$ H [m]	$H/\lambda = 1/30$ H [m]	$H/\lambda = 1/20$ H [m]
0.2828	0.1249	0.0021	0.0031	0.0042	0.0062
0.3536	0.1952	0.0033	0.0049	0.0065	0.0098
0.4243	0.2810	0.0047	0.0070	0.0094	0.0141
0.4950	0.3825	0.0064	0.0096	0.0128	0.0191
0.5657	0.4996	0.0083	0.0125	0.0167	0.0250
0.6364	0.6323	0.0105	0.0158	0.0211	0.0316
0.7071	0.7806	0.0130	0.0195	0.0260	0.0390
0.7778	0.9444	0.0157	0.0236	0.0315	0.0472
0.8485	1.1233	0.0187	0.0281	0.0374	0.0562
0.9192	1.3163	0.0219	0.0329	0.0439	0.0658
0.9899	1.5214	0.0254	0.0380	0.0507	0.0761
1.0607	1.7360	0.0289	0.0434	0.0579	0.0868
1.1314	1.9571	0.0326	0.0489	0.0652	0.0979
1.2021	2.1818	0.0364	0.0545	0.0727	0.1091
1.2728	2.4079	0.0401	0.0602	0.0803	0.1204
1.3435	2.6339	0.0439	0.0658	0.0878	0.1317
1.4142	2.8588	0.0476	0.0715	0.0953	0.1429
1.4849	3.0819	0.0514	0.0770	0.1027	0.1541
1.5556	3.3030	0.0551	0.0826	0.1101	0.1652
1.6263	3.5221	0.0587	0.0881	0.1174	0.1761
1.6971	3.7391	0.0623	0.0935	0.1246	0.1870
1.7678	3.9541	0.0659	0.0989	0.1318	0.1977
1.8385	4.1672	0.0695	0.1042	0.1389	0.2084
1.9092	4.3786	0.0730	0.1095	0.1460	0.2189
1.9799	4.5884	0.0765	0.1147	0.1529	0.2294

Table C.2: Test conditions for irregular waves in model scale

	$T_p = 1.679s$	$T_p = 1.4142s$	$T_p = 1.2728s$	$T_p = 1.1314s$
$H_s[m]$	0.02	0.04	0.04	0.01
	0.04	0.08	0.08	0.02
	0.06	0.10	0.10	0.03
	0.08	-	-	0.04
	0.10	-	-	0.05
	0.12	-	-	0.06
	0.14	-	-	0.07
	0.16	-	-	0.08

Appendix D

Regular Waves - RAO

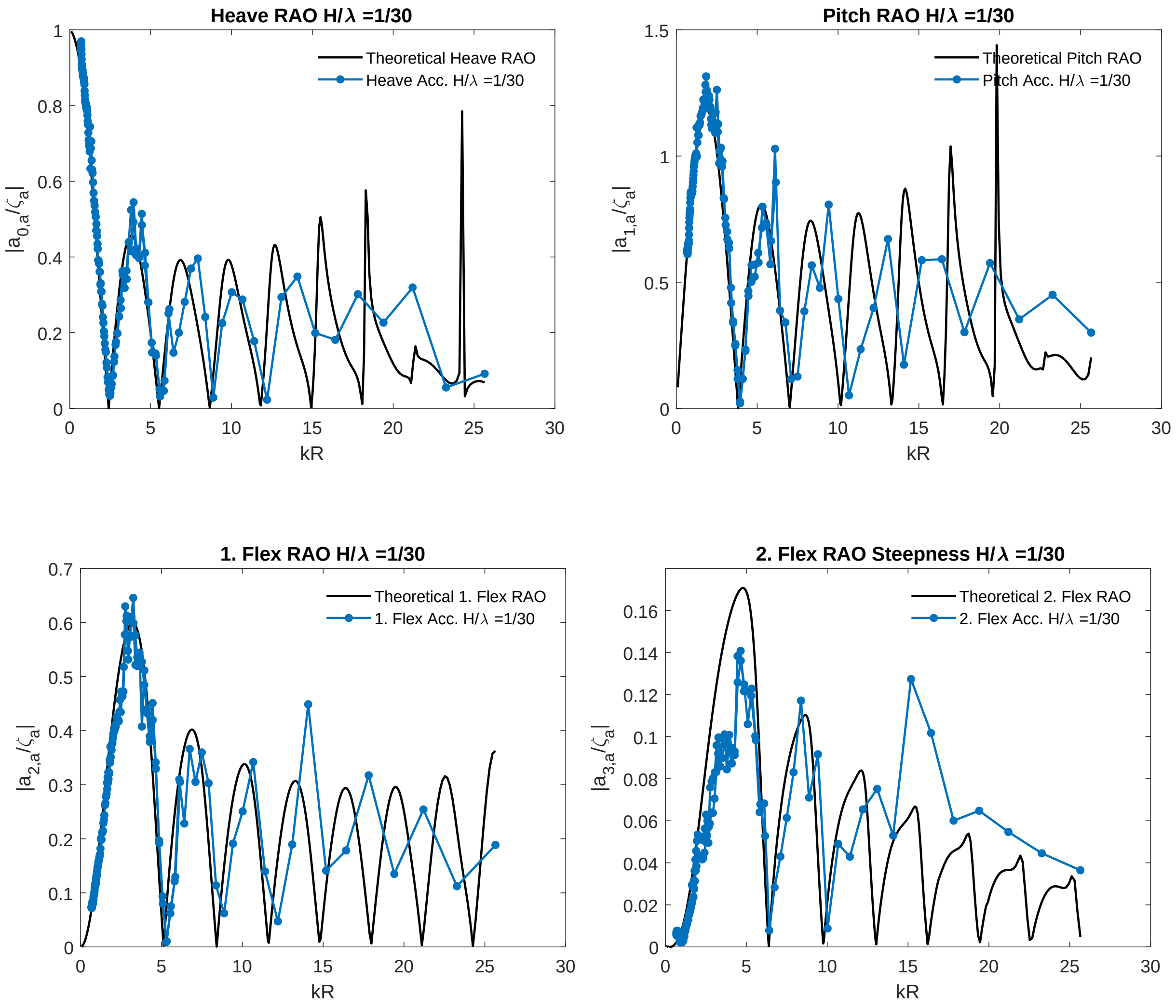

Figure D.1: Numerical RAO for the Linear-Slender Body theory compared to the experimental RAO for the single-torus, in heave, pitch, first flexible mode and second flexible mode for wave steepness $H/\lambda = 1/30$.

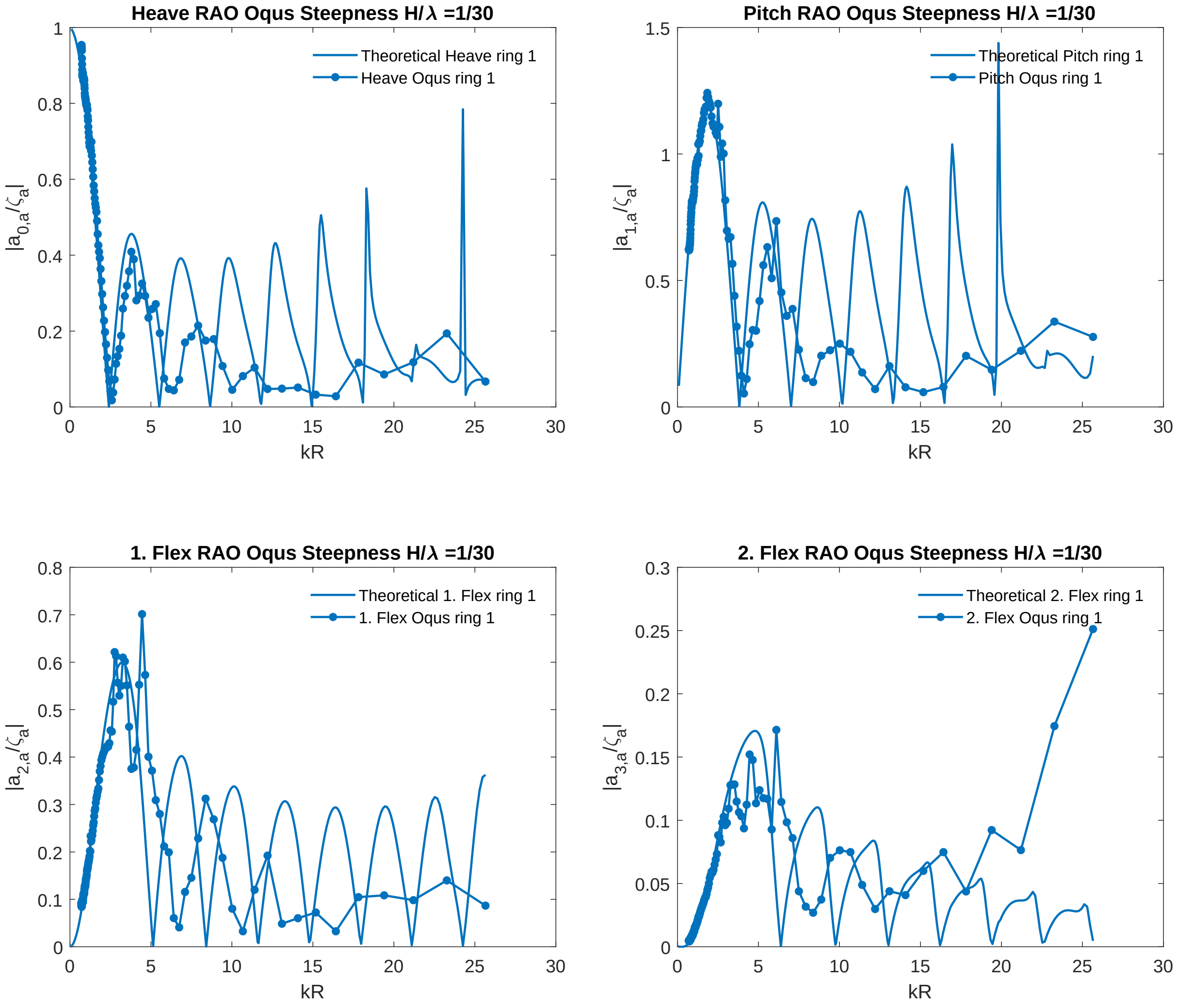

Figure D.2: Numerical RAO for a single torus using the Linear-Slender Body theory, compared to the experimental RAO for ring 1 of the multi-torus, in heave, pitch, first flexible mode and second flexible mode for wave steepness $H/\lambda = 1/30$

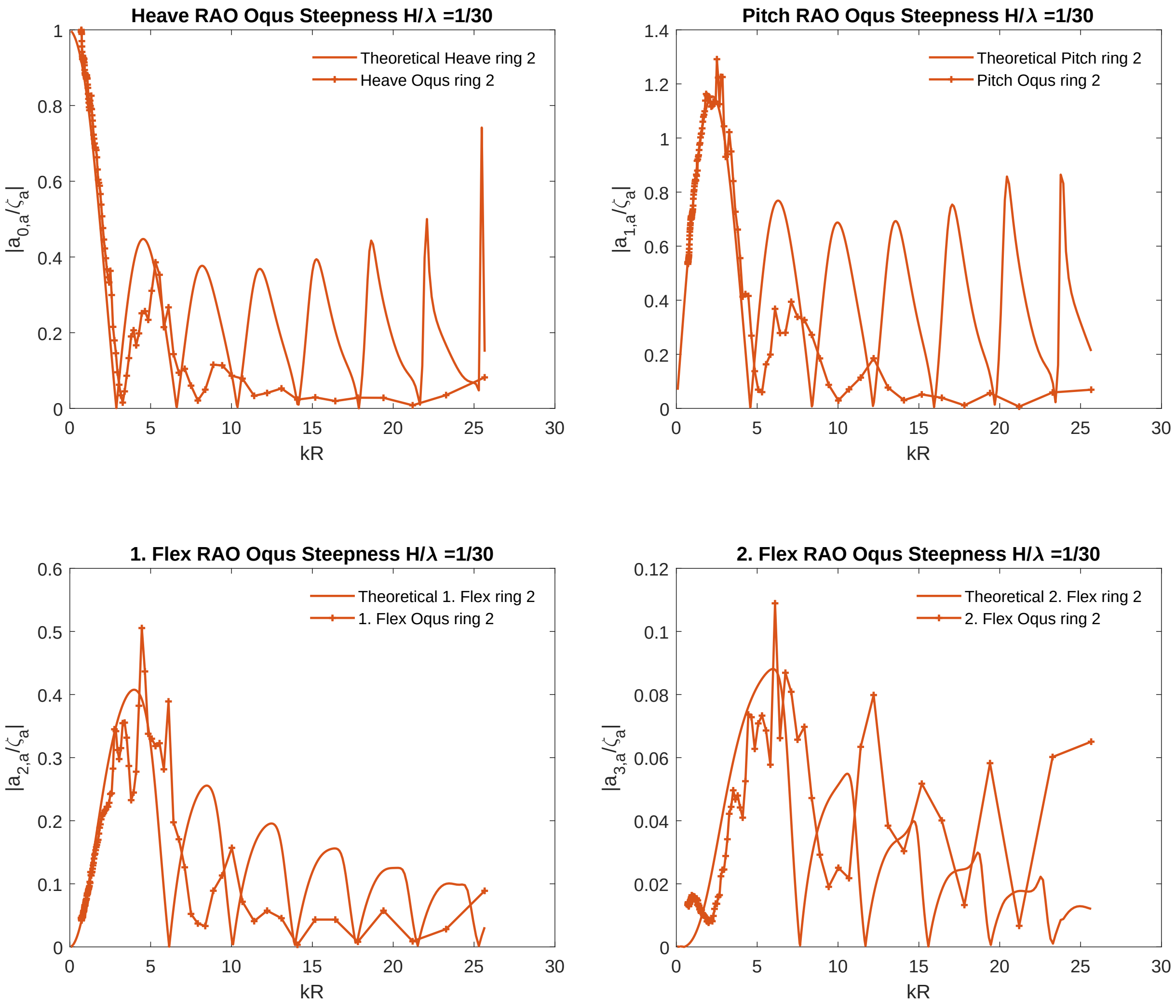

Figure D.3: Numerical RAO for a single torus using the Linear-Slender Body theory, compared to the experimental RAO for ring 2 of the multi-torus, in heave, pitch, first flexible mode and second flexible mode for wave steepness $H/\lambda = 1/30$

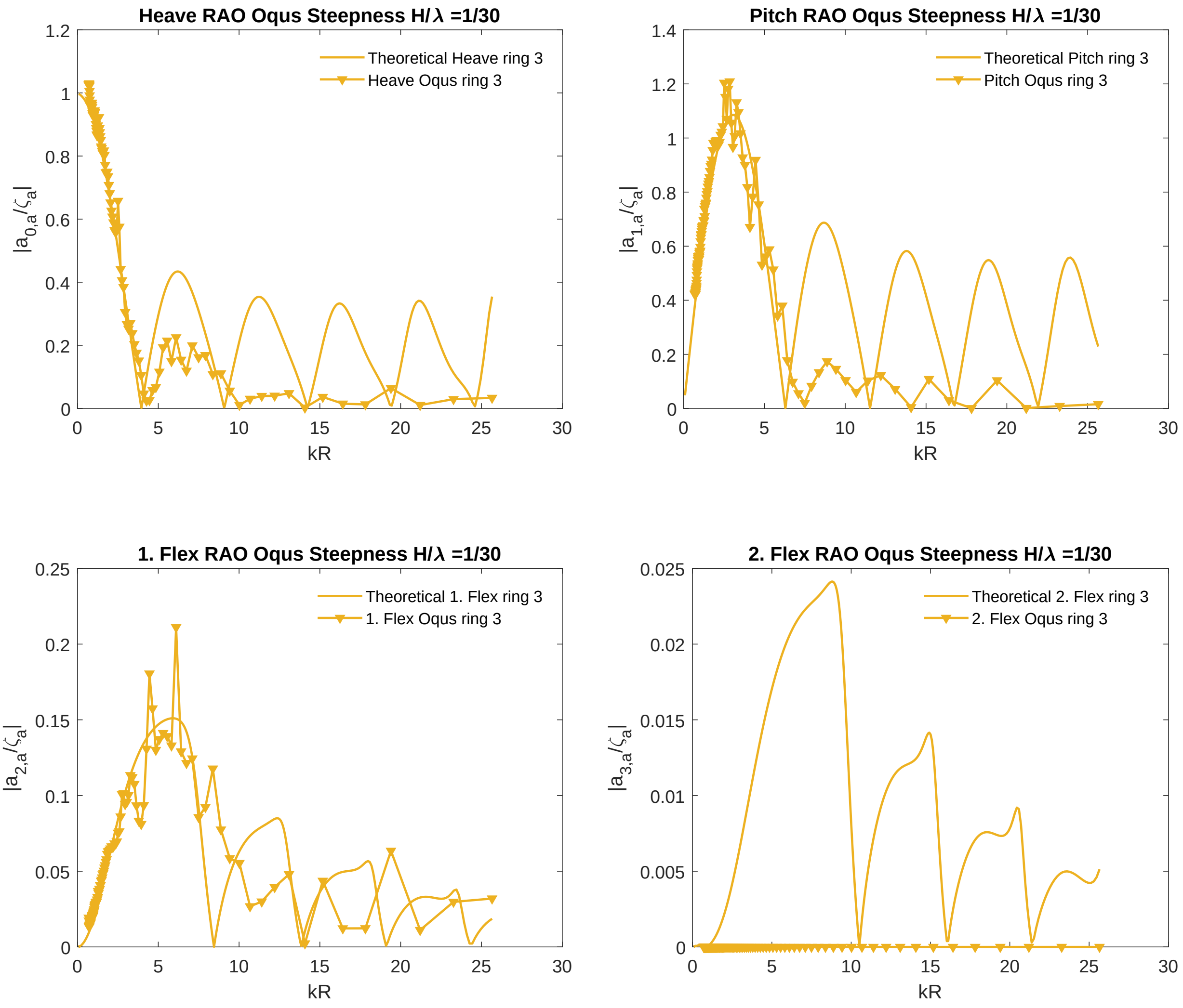

Figure D.4: Numerical RAO for a single torus using the Linear-Slender Body theory, compared to the experimental RAO for ring 3 of the multi-torus, in heave, pitch, first flexible mode and second flexible mode for wave steepness $H/\lambda = 1/30$

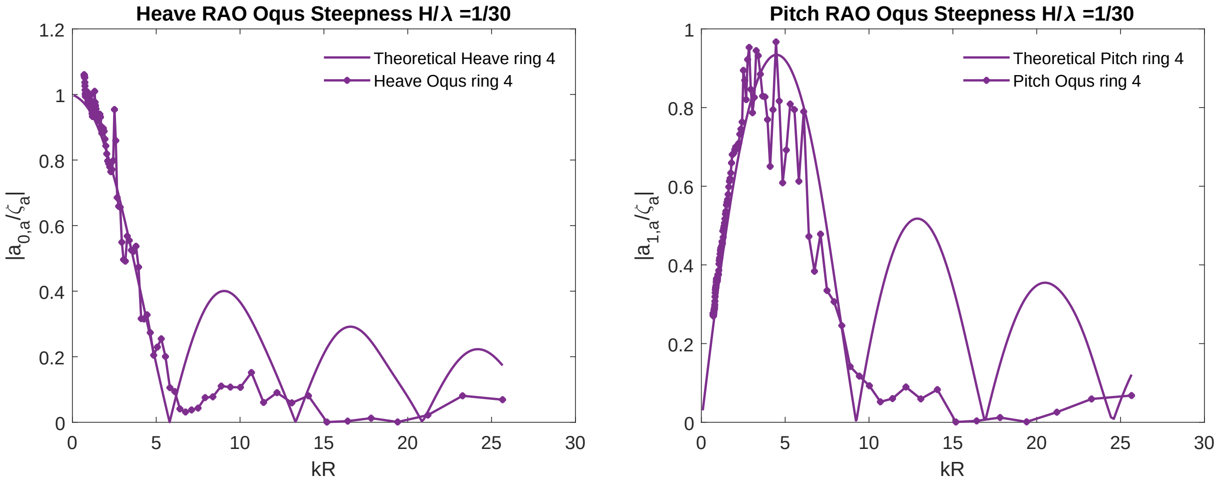

Figure D.5: Numerical RAO for a single torus using the Linear-Slender Body theory, compared to the experimental RAO for ring 4 of the multi-torus, in heave and pitch for wave steepness $H/\lambda = 1/30$

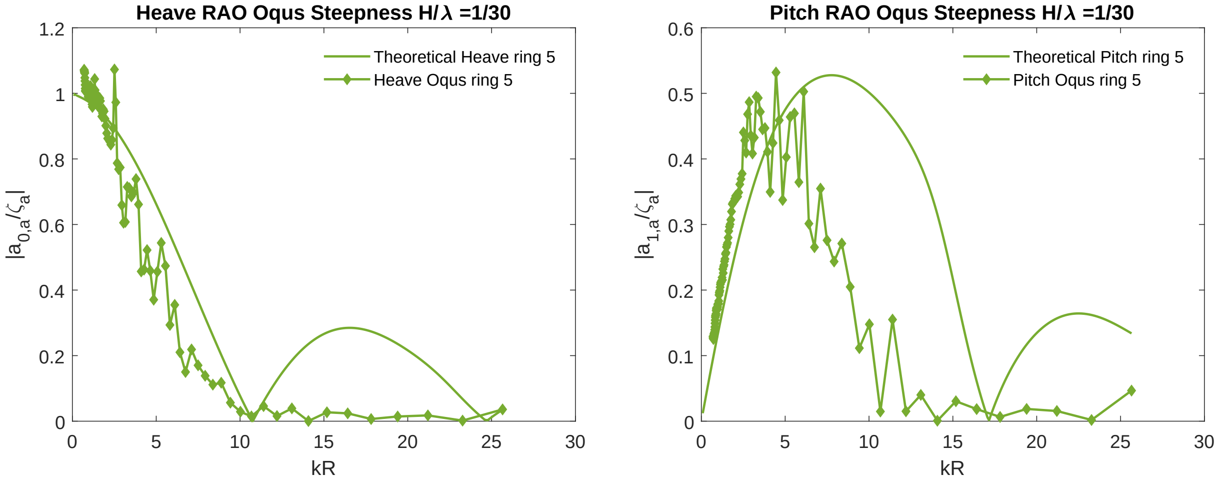

Figure D.6: Numerical RAO for a single torus using the Linear-Slender Body theory, compared to the experimental RAO for ring 1 of the multi-torus, in heave and pitch for wave steepness $H/\lambda = 1/30$

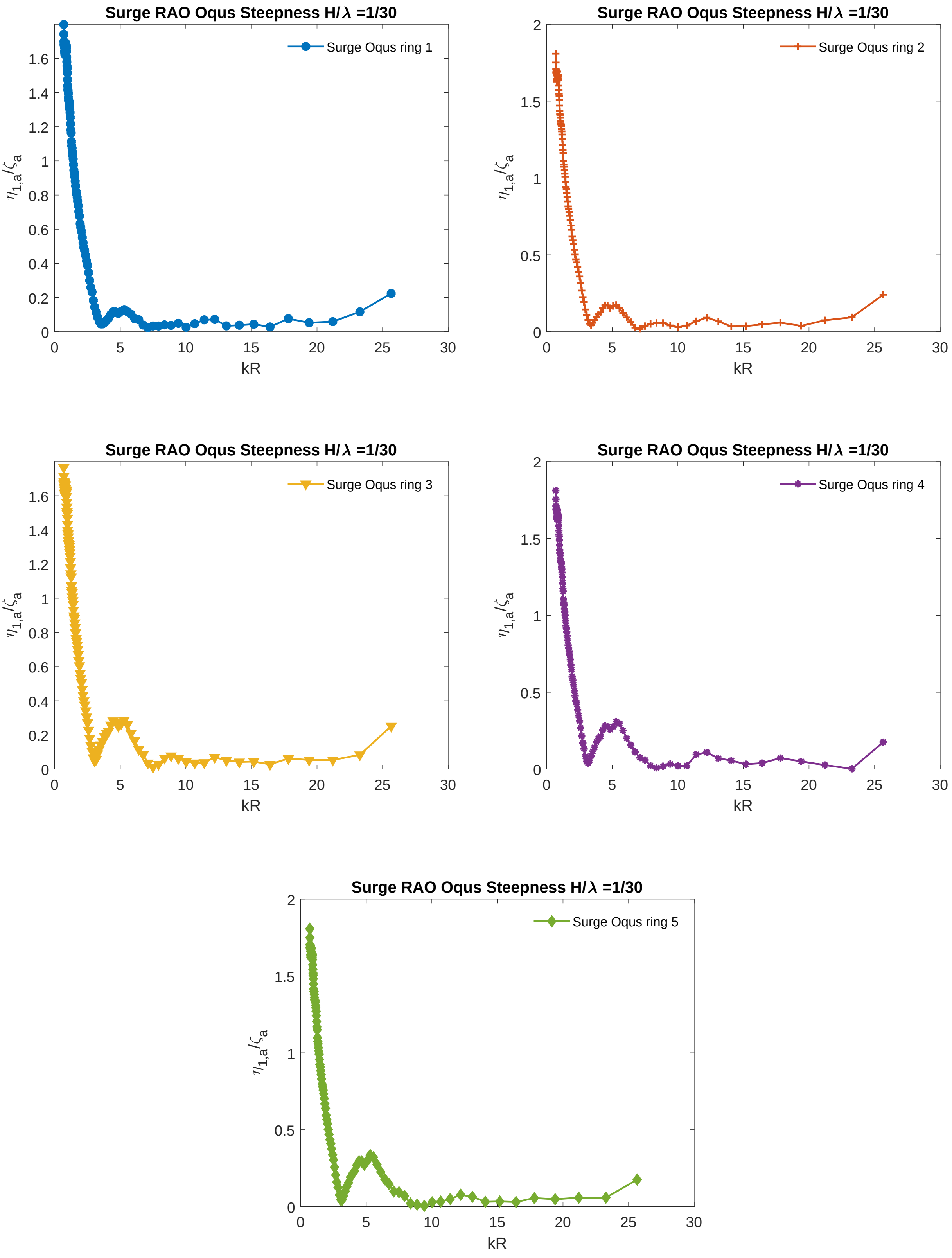

Figure D.7: Experimental RAO in surge for ring 1,2,3,4 and 5 of the multi-torus for wave steepness $H/\lambda = 1/30$

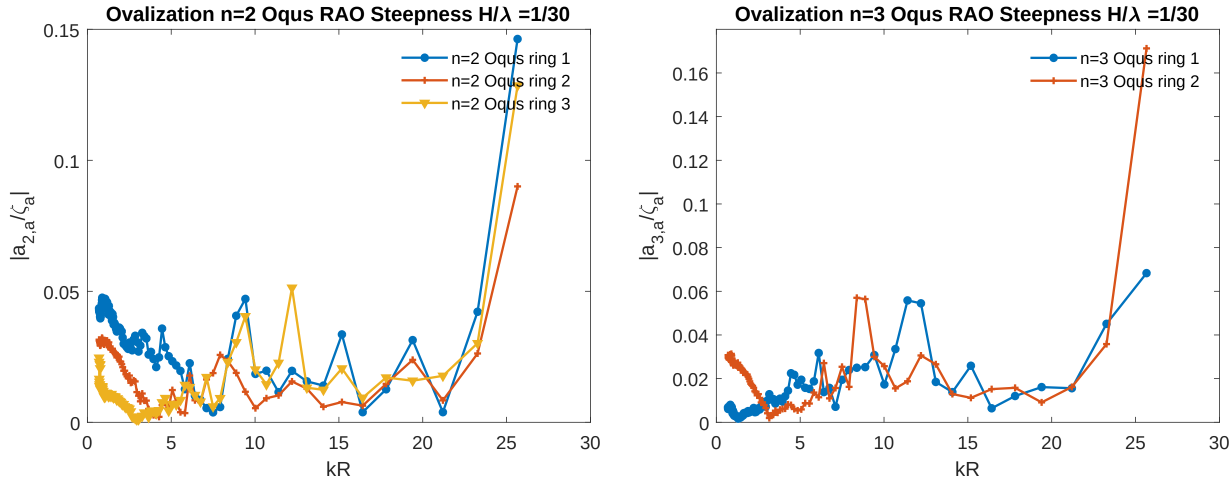

Figure D.8: Horizontal ovalization RAO of multi-tori for ring 1, 2 and 3 when $n = 2$ in the left figure, and for ring 1 and 2 when $n = 3$ in the right figure. Wave steepness is $H/\lambda = 1/30$.

Appendix E

Irregular Waves - RAO

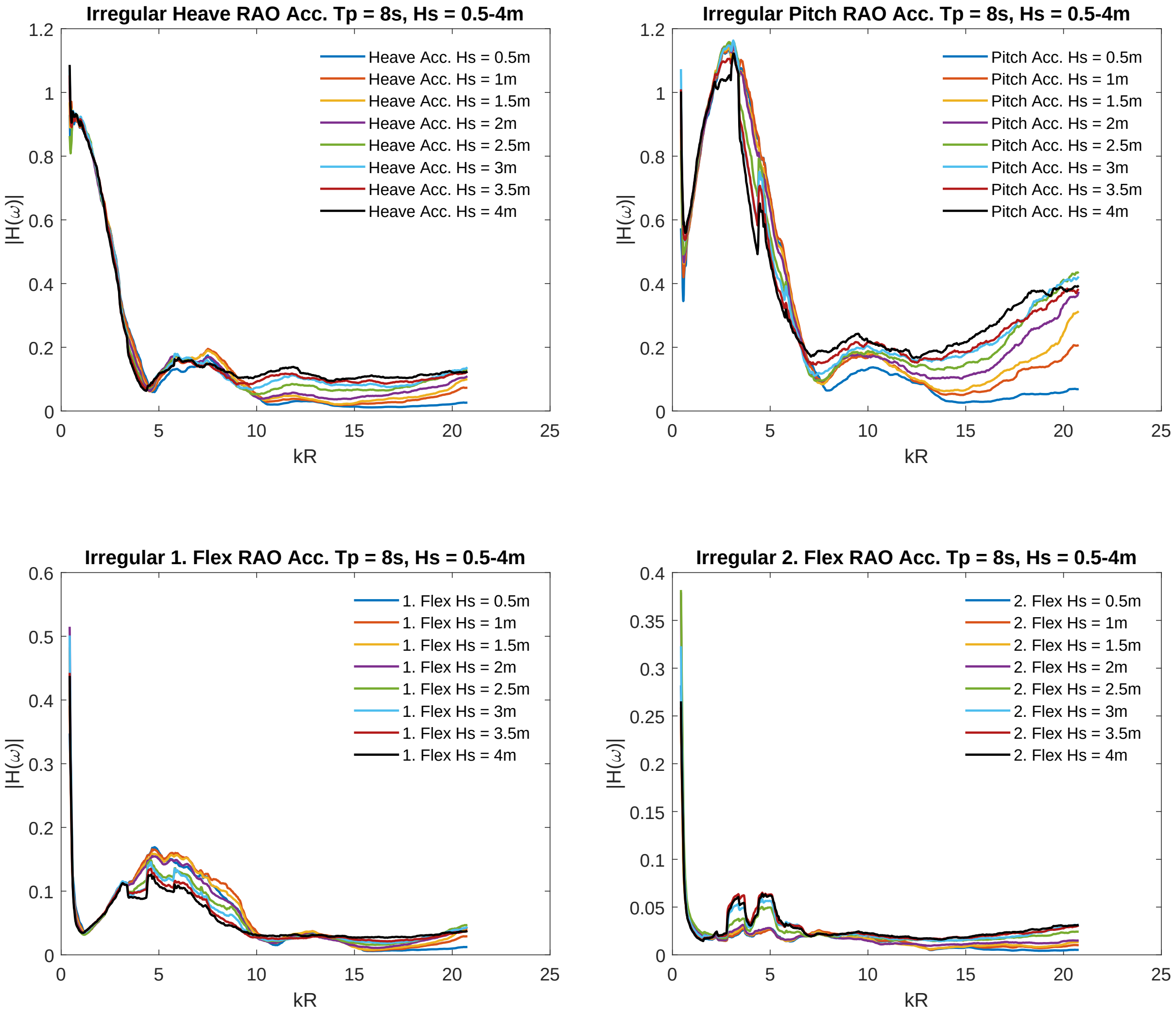

Figure E.1: Experimental RAO for ring 3 of the multi-torus, in heave, pitch, first flexible mode and second flexible mode with peak wave period $T_p = 8s$ and $H_s = 0.5, 1, 1.5, 2, 2.5, 3, 3.5, 4m$

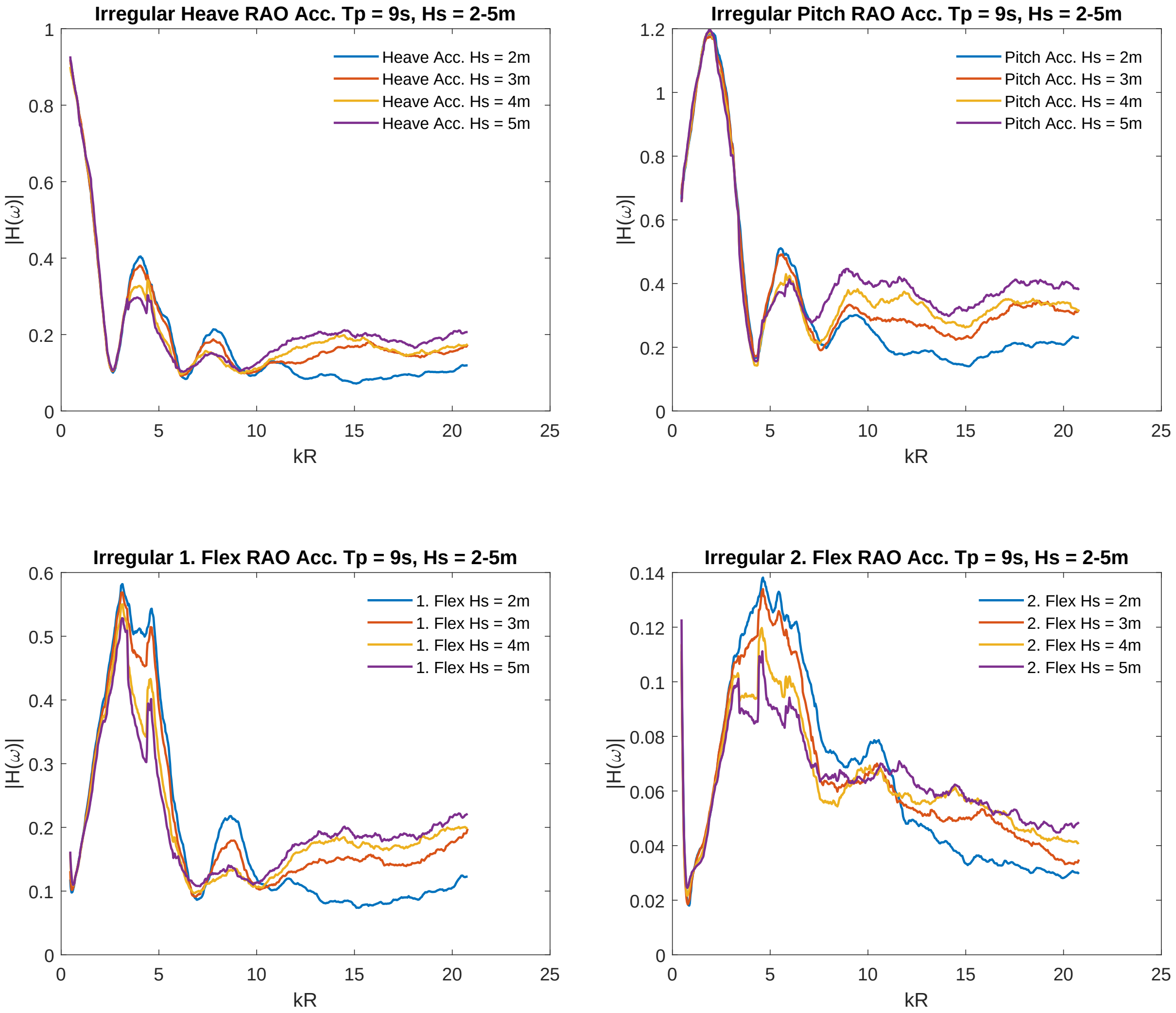

Figure E.2: Experimental RAO for ring 1 of the multi-torus, in heave, pitch, first flexible mode and second flexible mode with peak wave period $T_p = 9s$ and $H_s = 2, 3, 4, 5m$

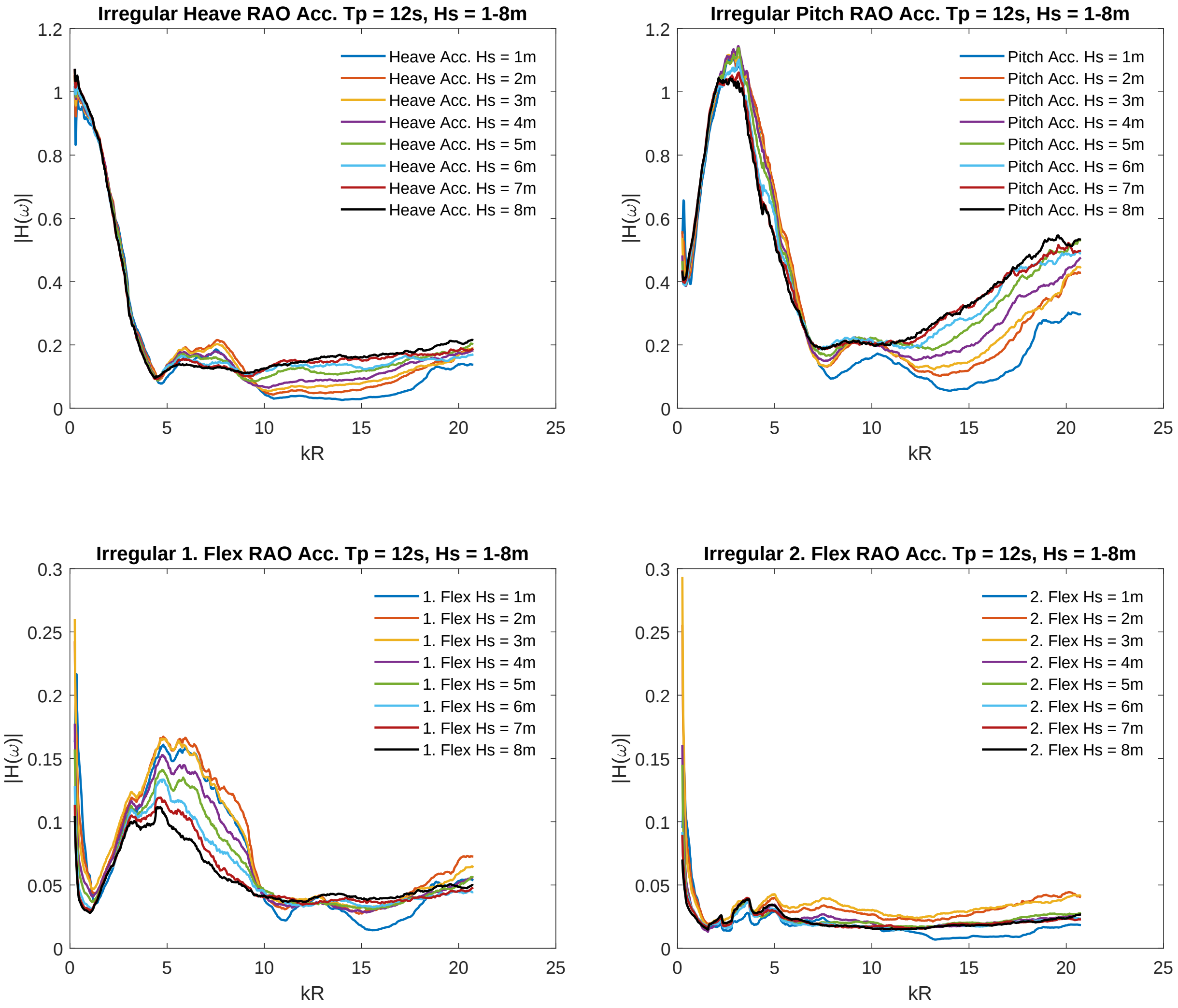

Irregular Heave RAO Acc. Tp = 12s, Hs = 1-8m

Irregular Pitch RAO Acc. Tp = 12s, Hs = 1-8m

Irregular 1. Flex RAO Acc. Tp = 12s, Hs = 1-8m

Irregular 2. Flex RAO Acc. Tp = 12s, Hs = 1-8m

Figure E.3: Experimental RAO for ring 3 of the multi-torus, in heave, pitch, first flexible mode and second flexible mode with peak wave period $T_p = 12s$ and $H_s = 1, 2, 3, 4, 5, 6, 7, 8m$

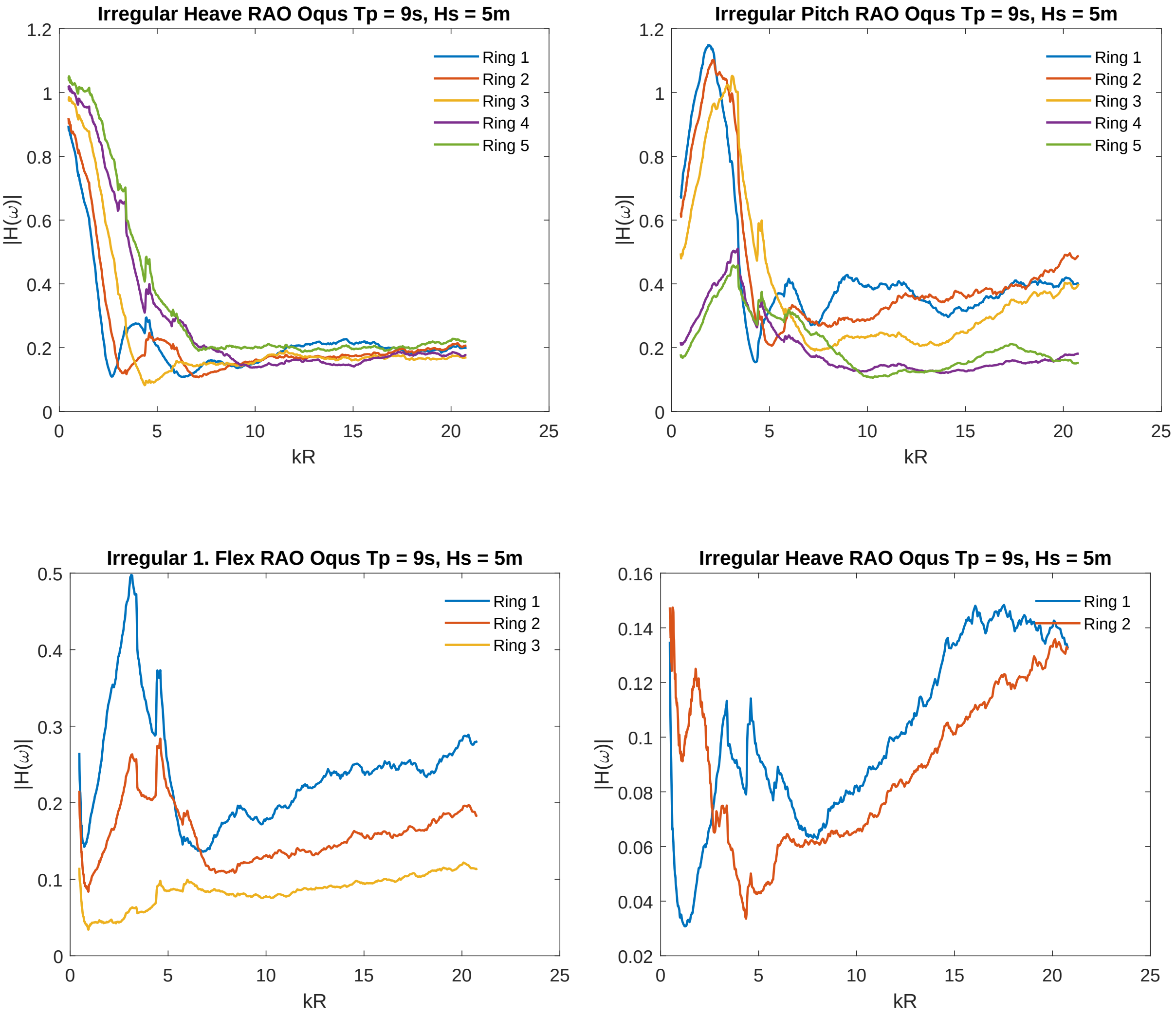

Figure E.4: Experimental RAO for ring 1,2,3 of the multi-torus, in heave, pitch, first flexible mode and second flexible mode with peak wave period $T_p = 9s$ and $H_s = 5m$

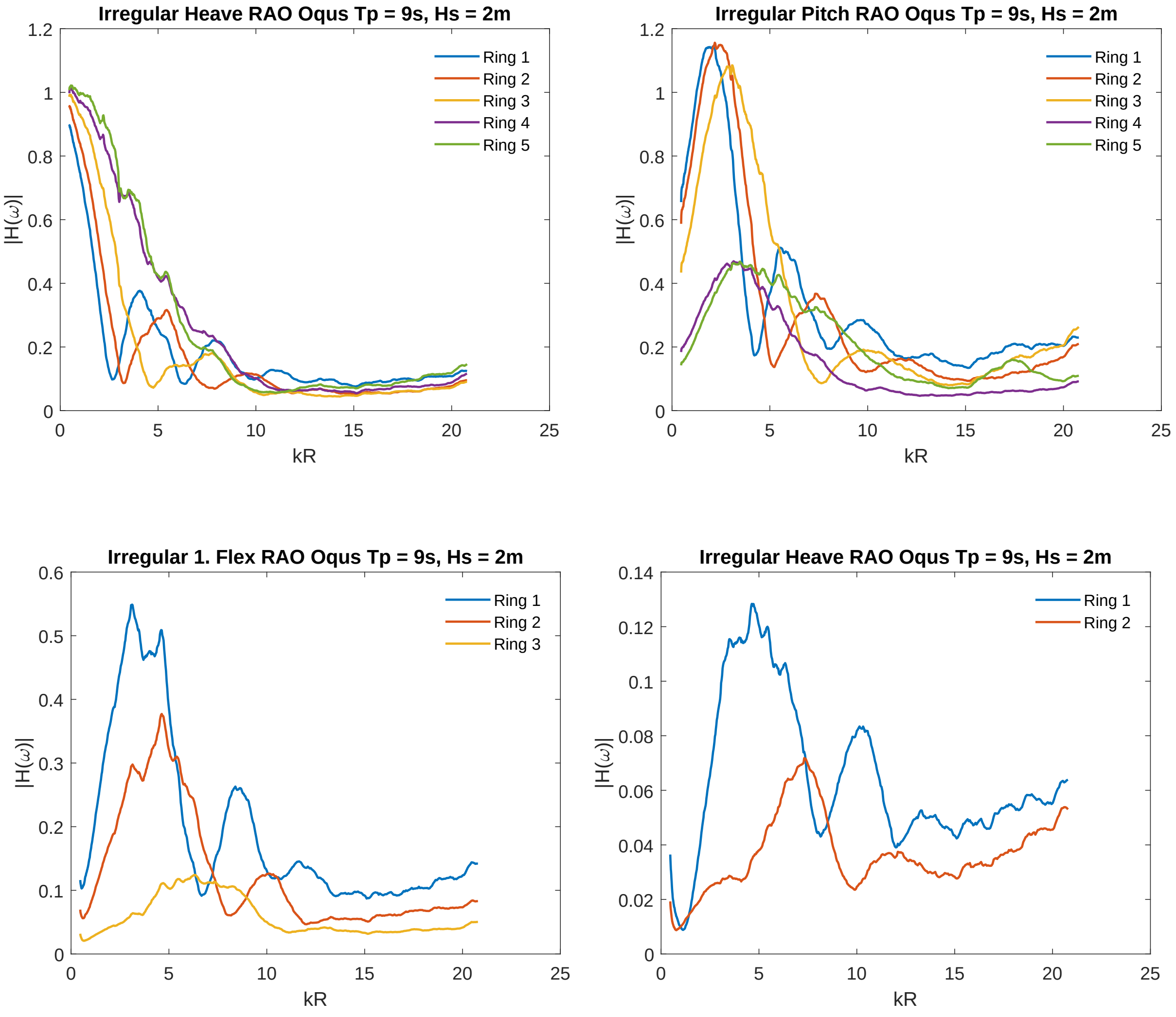

Figure E.5: Experimental RAO for ring 1,2,3 of the multi-torus, in heave, pitch, first flexible mode and second flexible mode with peak wave period $T_p = 9s$ and $H_s = 2m$

Appendix F

Time-Series

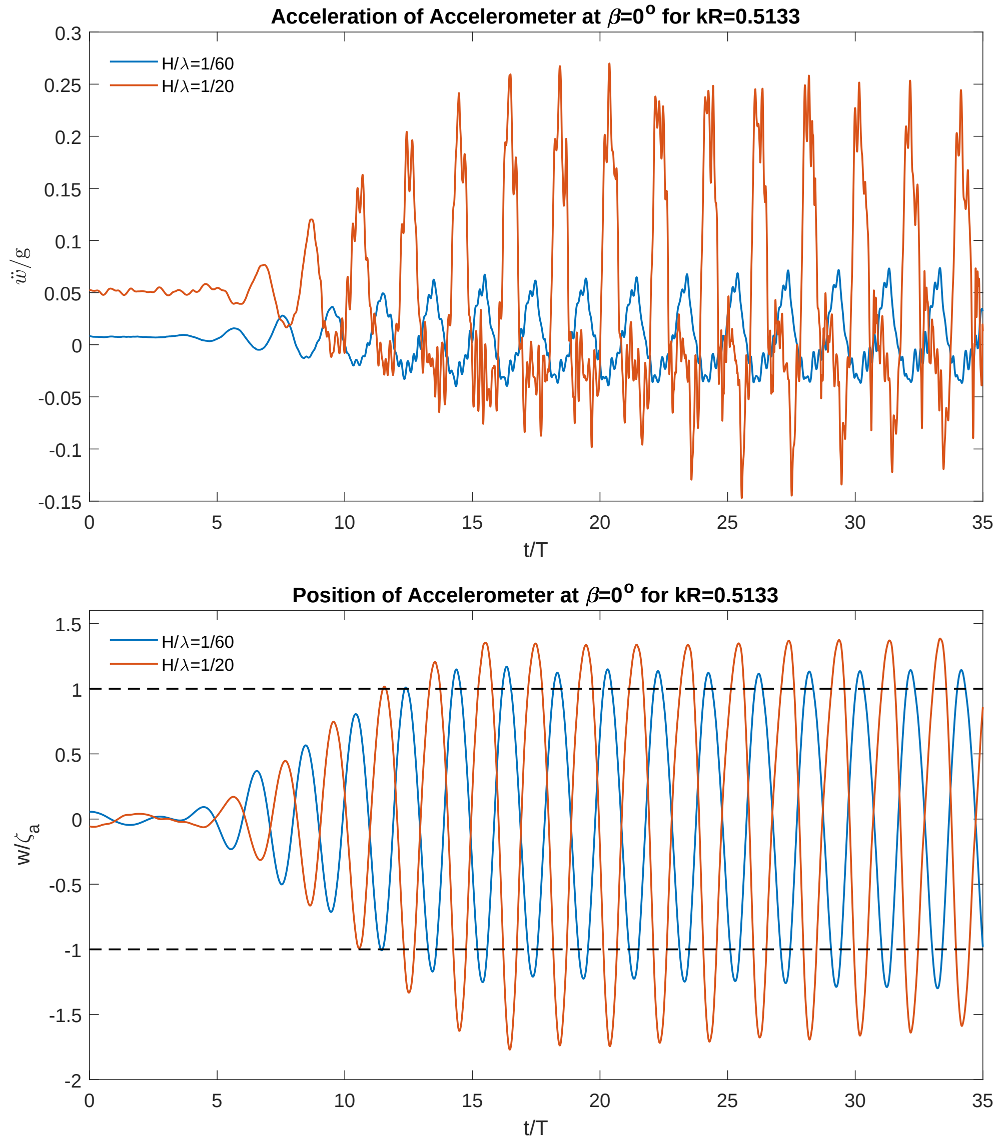

Figure F.1: Multi-torus: Both figures show time-series examples of experimental results from a wave series with $H/\lambda = 1/60$ and $H/\lambda = 1/20$ with $kR = 0.5133$. Upper figure shows the non-dimensional acceleration $\ddot{w}$ at $\beta = 0^o$. Lower figure shows a time-series example of the non-dimensional motion w of the accelerometer at $\beta = 0^o$ relative to the incident wave ζ_a.

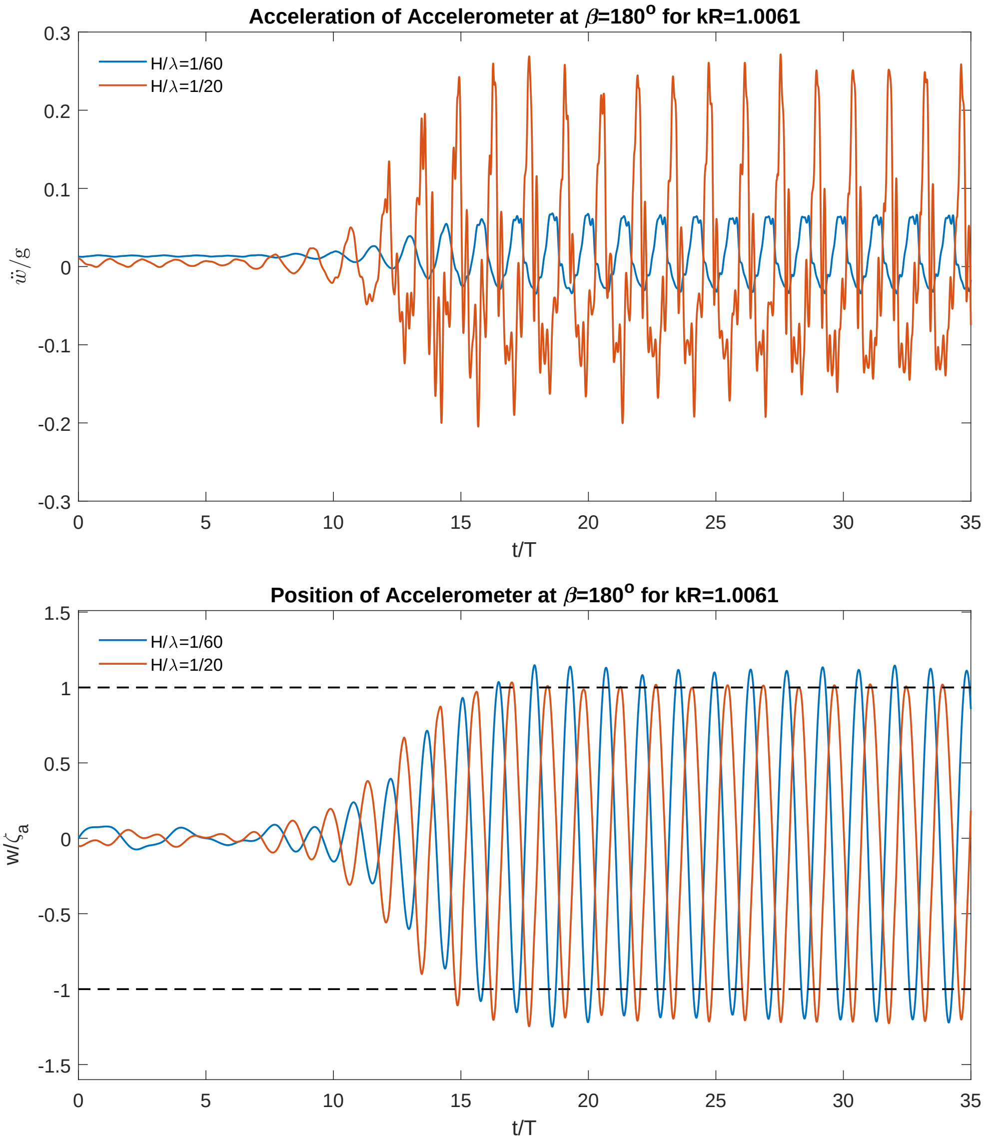

Figure F.2: Multi-torus: Both figures show time-series examples of experimental results from a wave series with $H/\lambda = 1/60$ and $H/\lambda = 1/20$ with $kR = 1.0061$. Upper figure shows the non-dimensional acceleration $\ddot{w}$ at $\beta = 180^o$. Lower figure shows a time-series example of the non-dimensional motion w of the accelerometer at $\beta = 180$ relative to the incident wave ζ_a.

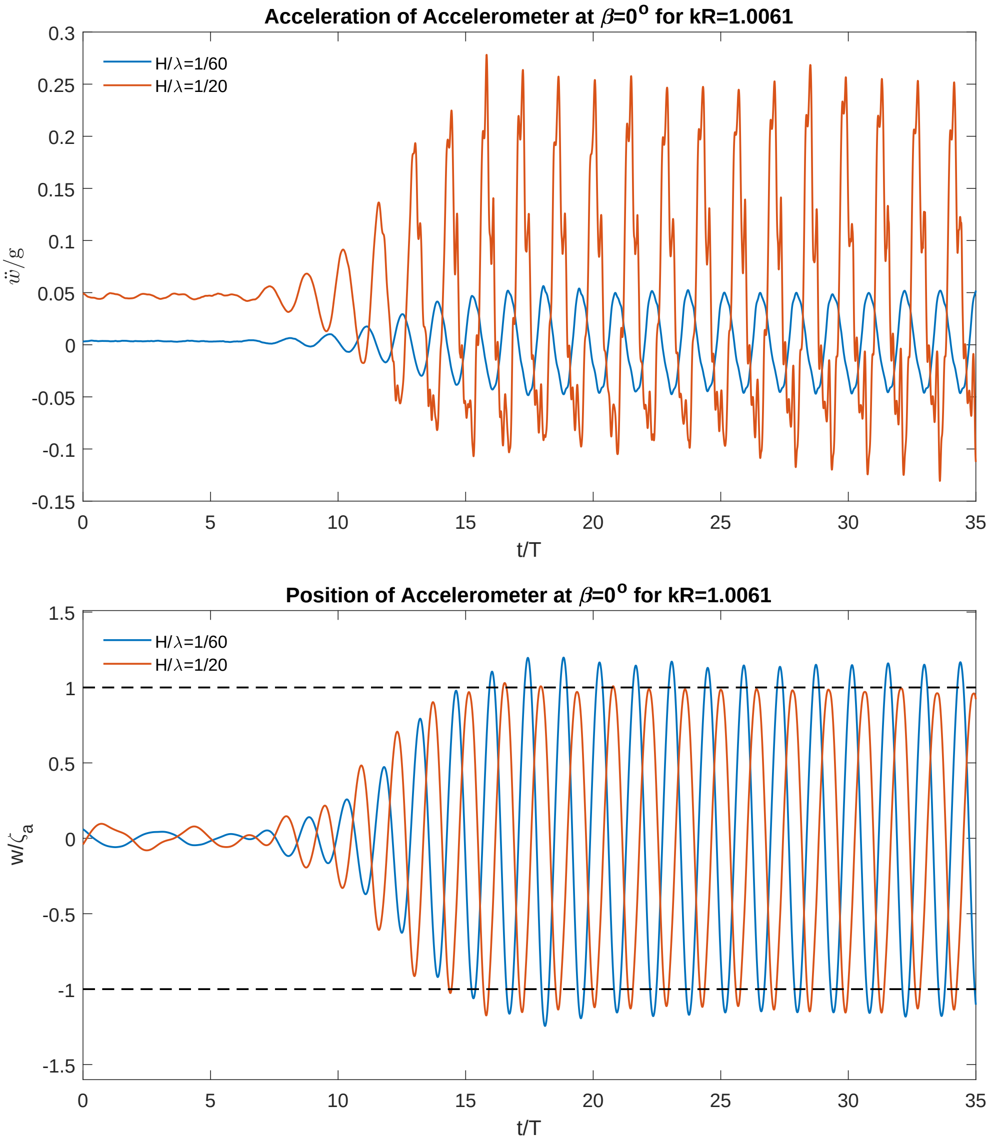

Figure F.3: Multi-torus: Both figures show time-series examples of experimental results from a wave series with $H/\lambda = 1/60$ and $H/\lambda = 1/20$ with $kR = 1.0061$. Upper figure shows the non-dimensional acceleration $\ddot{w}$ at $\beta = 0^o$. Lower figure shows a time-series example of the non-dimensional motion w of the accelerometer at $\beta = 0^o$ relative to the incident wave ζ_a.

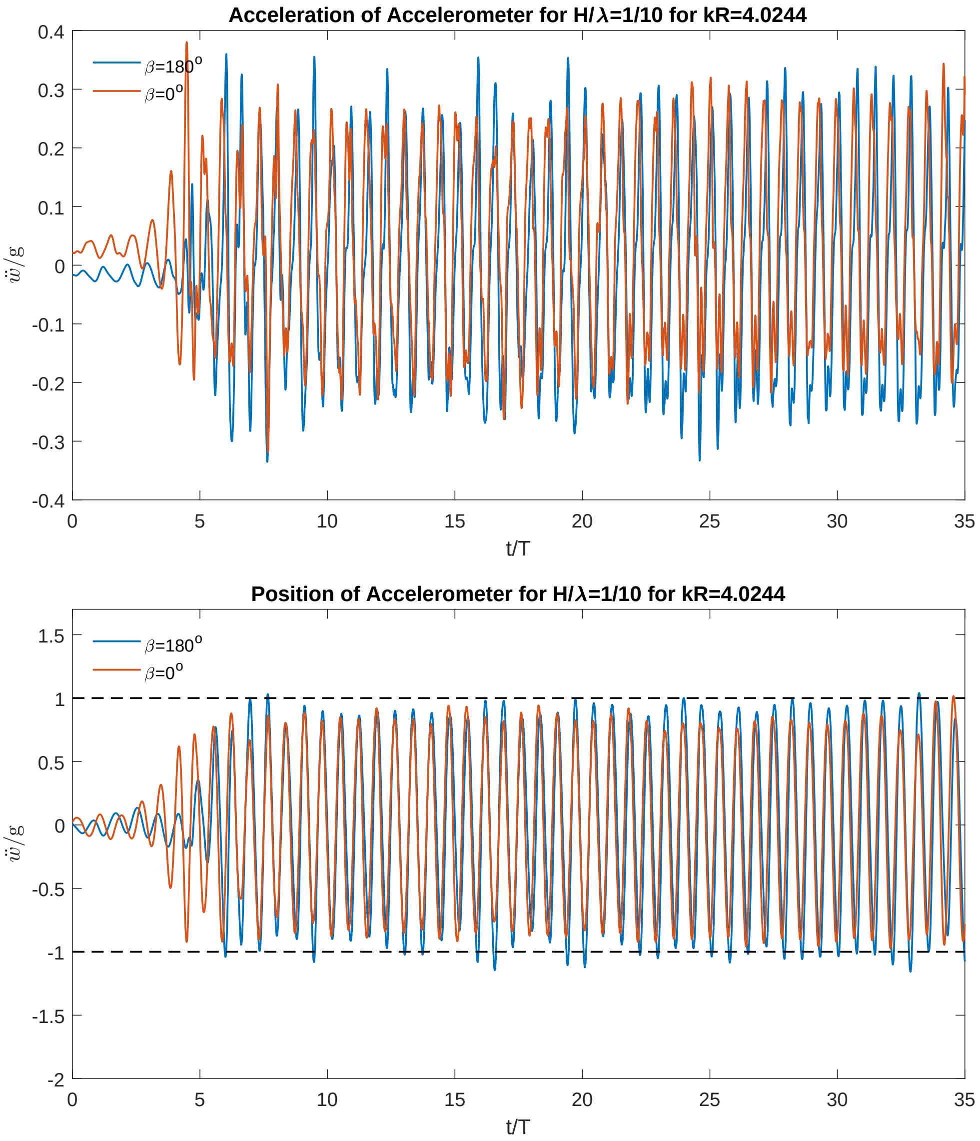

Figure F.4: Multi-torus: Both figures show time-series examples of experimental results from a wave series with $H/\lambda = 1/10$ with $kR = 4.0244$. Upper figure shows the non-dimensional acceleration $\ddot{w}$ at $\beta = 180^o$ and $\beta = 0^o$. Lower figure shows a time-series example of the non-dimensional motion w of the accelerometer at $\beta = 180$ and $\beta = 0^o$ relative to the incident wave ζ_a. ORIGINAL

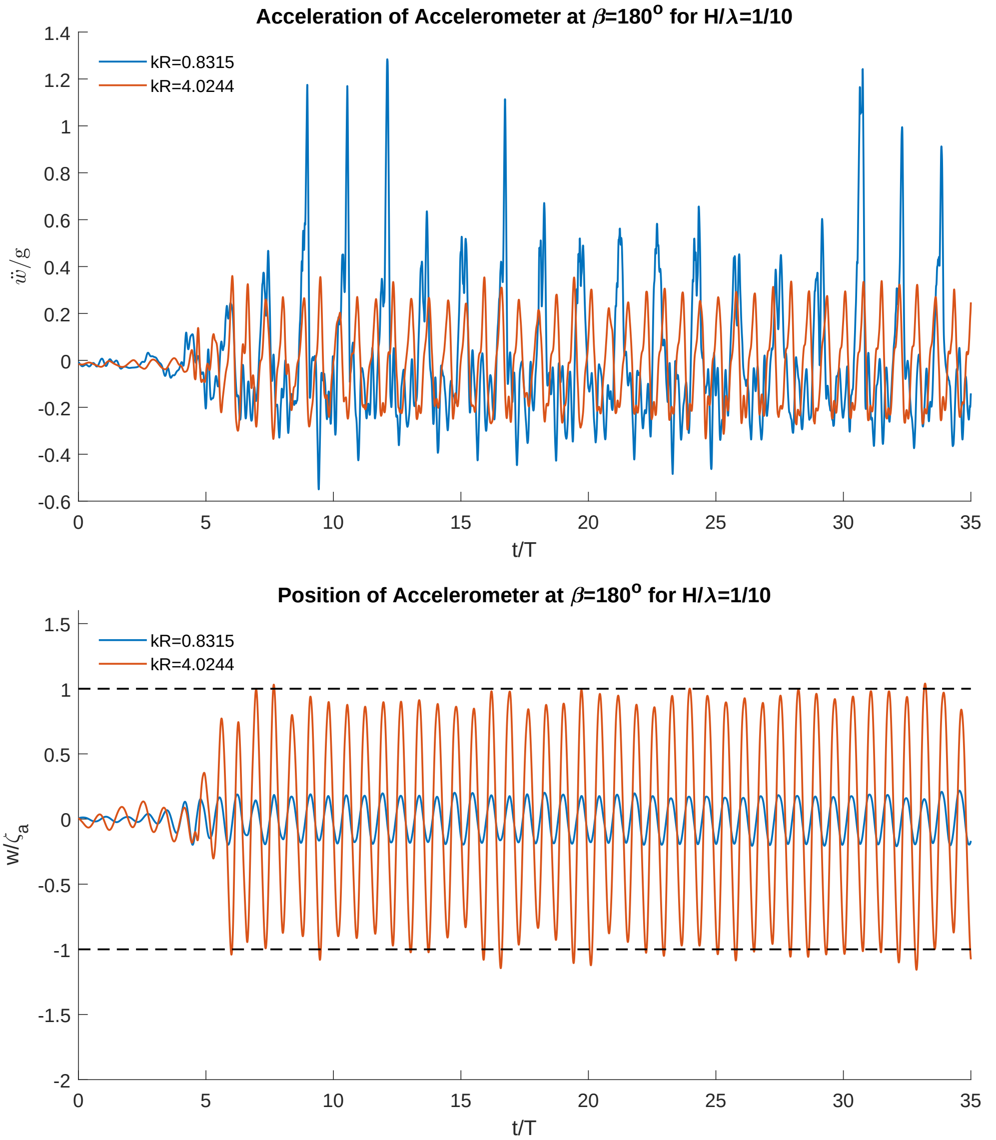

Figure F.5: Multi-torus: Both figures show time-series examples of experimental results at $\beta = 180$ from a wave series with $H/\lambda = 1/10$. Upper figure shows the non-dimensional acceleration $\ddot{w}$ with $kR = 0.8315$ and $kR = 4.0244. Lowerfigureshowsatime - seriesexampleofthenon - dimensionalmotionwoftheaccelerometerrelativetotheincidentwave\zeta_a$.

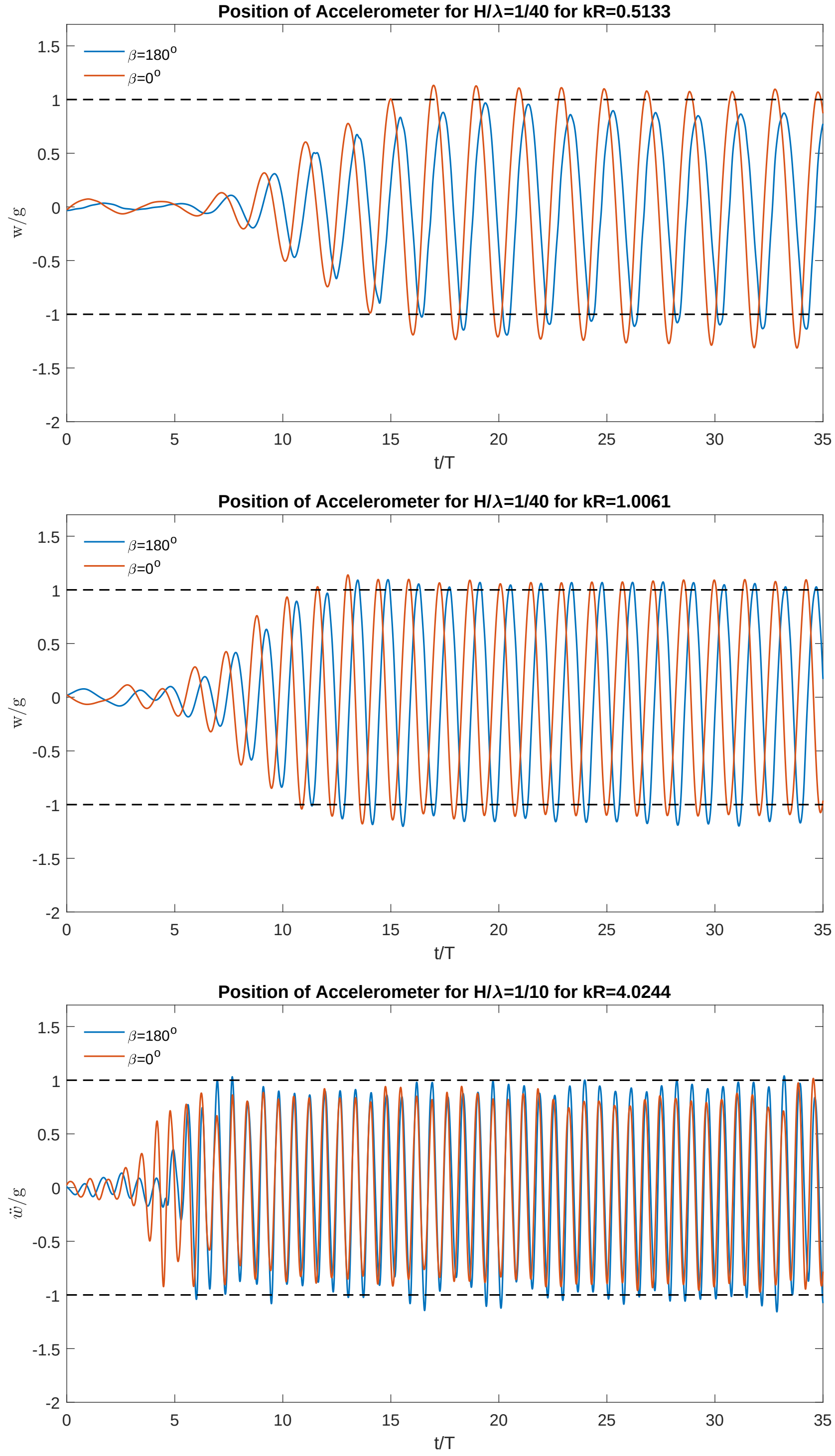

Figure F.6: Multi-torus: All figures show time-series examples of experimental results of the non-dimensional motion w of the accelerometer relative to the incident wave ζ_a at $\beta = 180^o$ and $\beta = 0^o$. Upper figure shows a time-series example from a wave series with $H/\lambda = 1/40$ with $kR = 0.5133$. Middle figure shows a time-series example from a wave series with $H/\lambda = 1/40$ with $kR = 1.0061$. Lower figure shows a time-series example from a wave series with $H/\lambda = 1/10$ with $kR = 4.0244$

Appendix G

Harmonics

G.1 Single torus

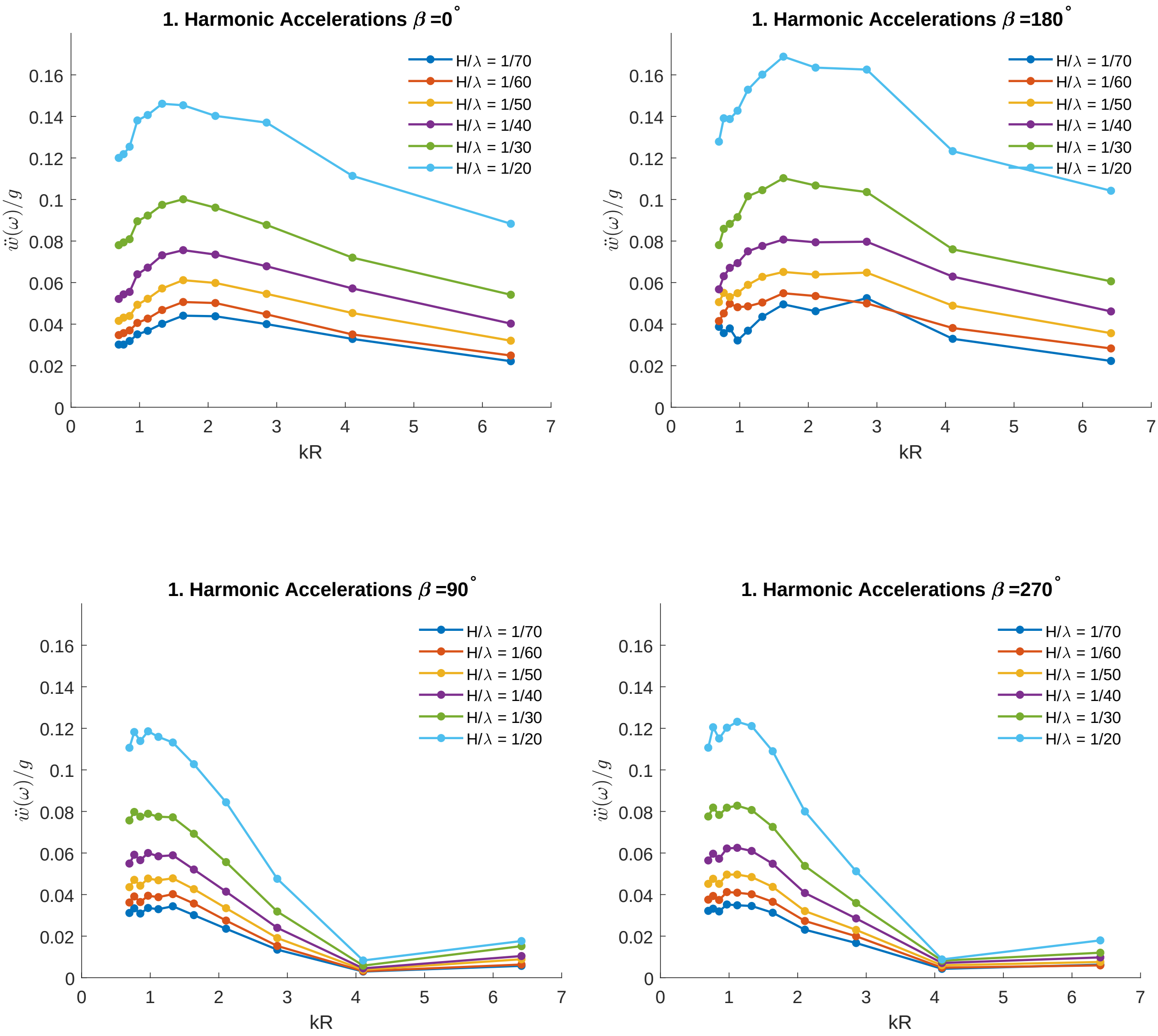

Figure G.1: Single-torus: Experimental first harmonic accelerations at $\beta = 0^o$, $\beta = 180^o$, $\beta = 90^o$ and $\beta = 270^o$ in waves with steepness $H/\lambda = 1/70$, $H/\lambda = 1/60$, $H/\lambda = 1/50$, $H/\lambda = 1/40$, $H/\lambda = 1/30$, $H/\lambda = 1/20$.

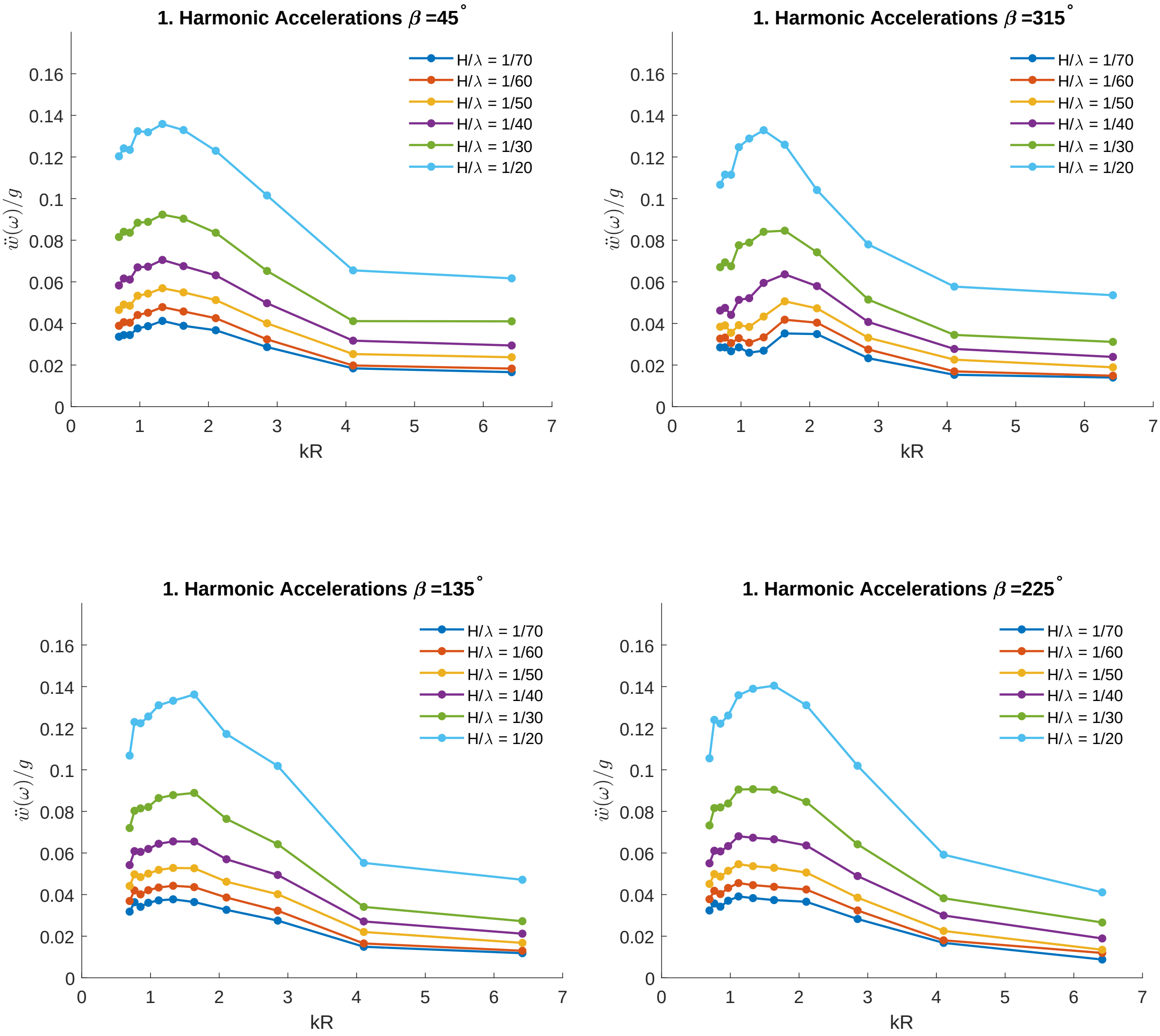

Figure G.2: Single-torus: Experimental first harmonic accelerations at $\beta = 45^o$, $\beta = 315^o$, $\beta = 135^o$ and $\beta = 225^o$ in waves with steepness $H/\lambda = 1/70$, $H/\lambda = 1/60$, $H/\lambda = 1/50$, $H/\lambda = 1/40$, $H/\lambda = 1/30$, $H/\lambda = 1/20$.

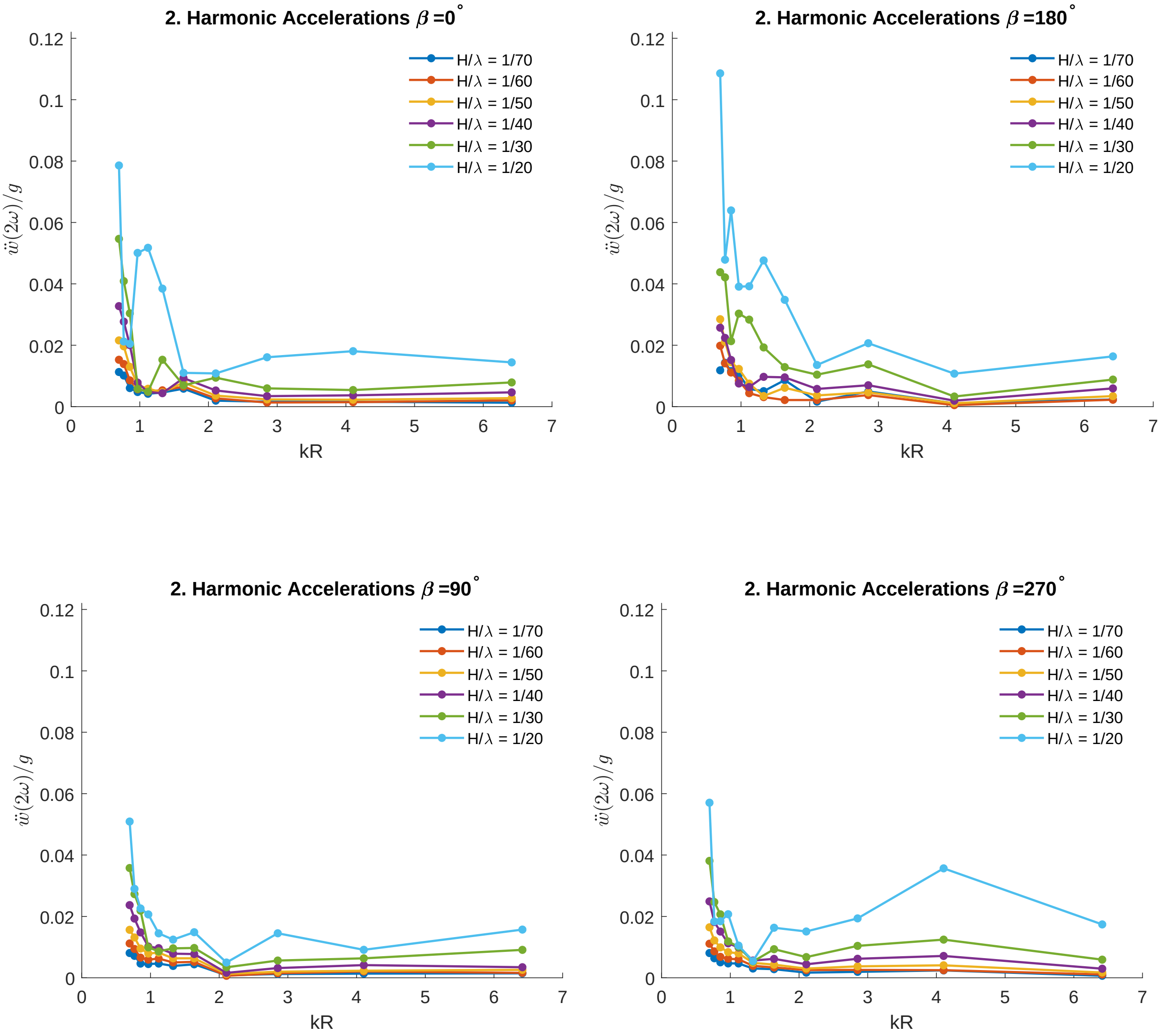

Figure G.3: Single-torus: Experimental second harmonic accelerations at $\beta = 0^o$, $\beta = 180^o$, $\beta = 90^o$ and $\beta = 270^o$ in waves with steepness $H/\lambda = 1/70$, $H/\lambda = 1/60$, $H/\lambda = 1/50$, $H/\lambda = 1/40$, $H/\lambda = 1/30$, $H/\lambda = 1/20$.

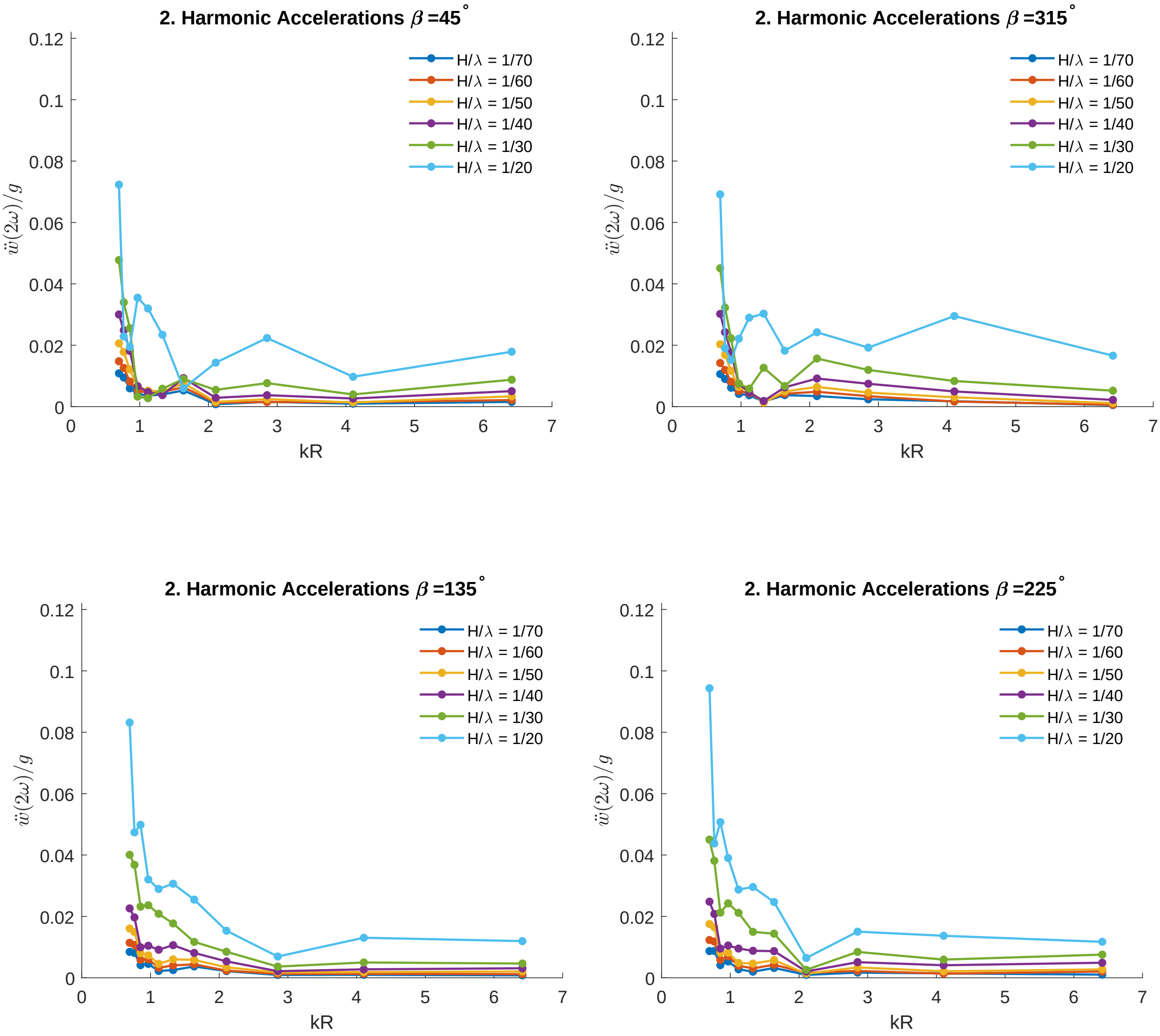

Figure G.4: Single-torus: Experimental second harmonic accelerations at $\beta = 45^o$, $\beta = 315^o$, $\beta = 135^o$ and $\beta = 225^o$ in waves with steepness $H/\lambda = 1/70$, $H/\lambda = 1/60$, $H/\lambda = 1/50$, $H/\lambda = 1/40$, $H/\lambda = 1/30$, $H/\lambda = 1/20$.

G.2 Multi-torus

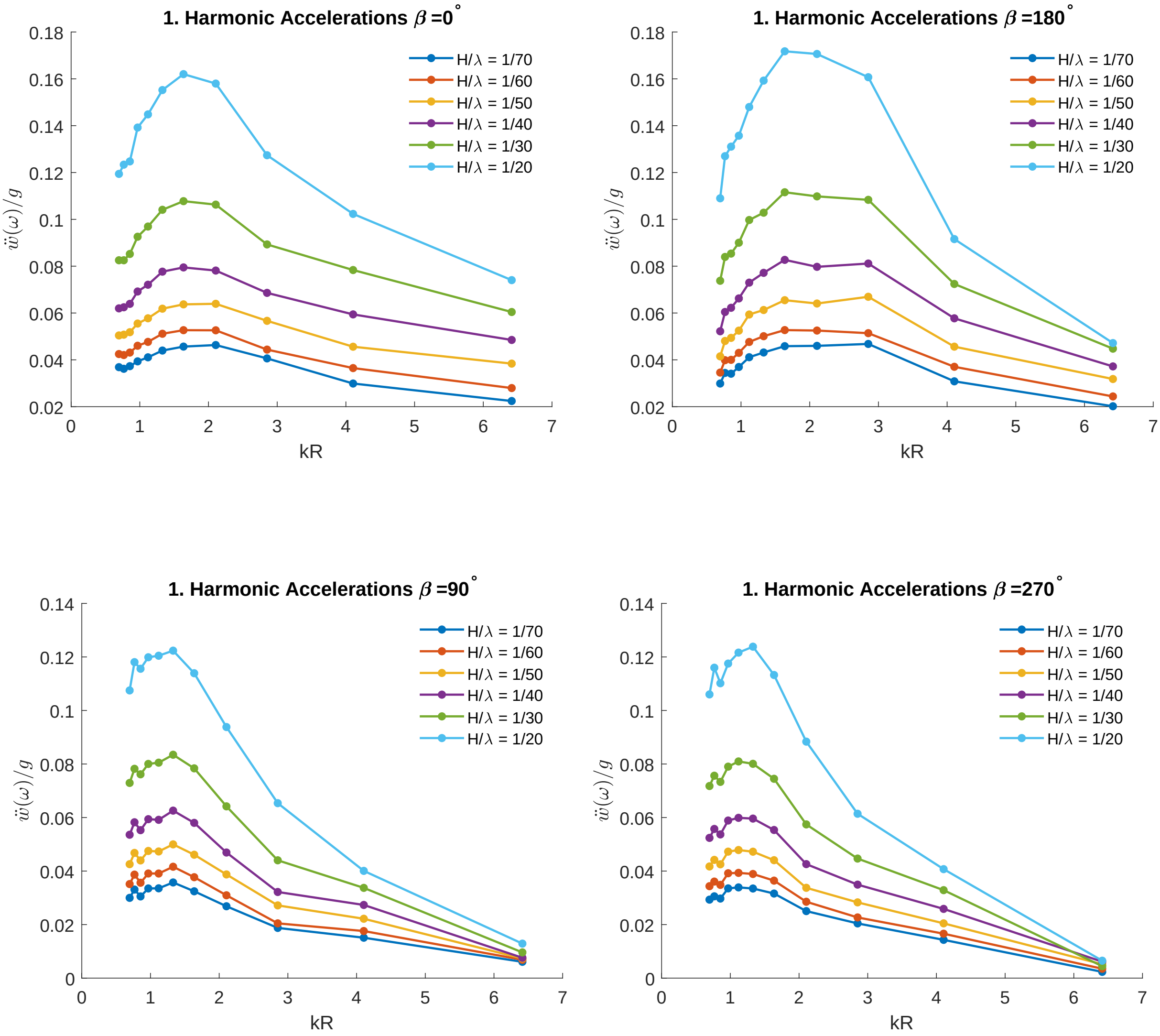

Figure G.5: Multi-torus: Experimental first harmonic accelerations at $\beta = 0^o$, $\beta = 180^o$, $\beta = 90^o$ and $\beta = 270^o$ in waves with steepness $H/\lambda = 1/70$, $H/\lambda = 1/60$, $H/\lambda = 1/50$, $H/\lambda = 1/40$, $H/\lambda = 1/30$, $H/\lambda = 1/20$.

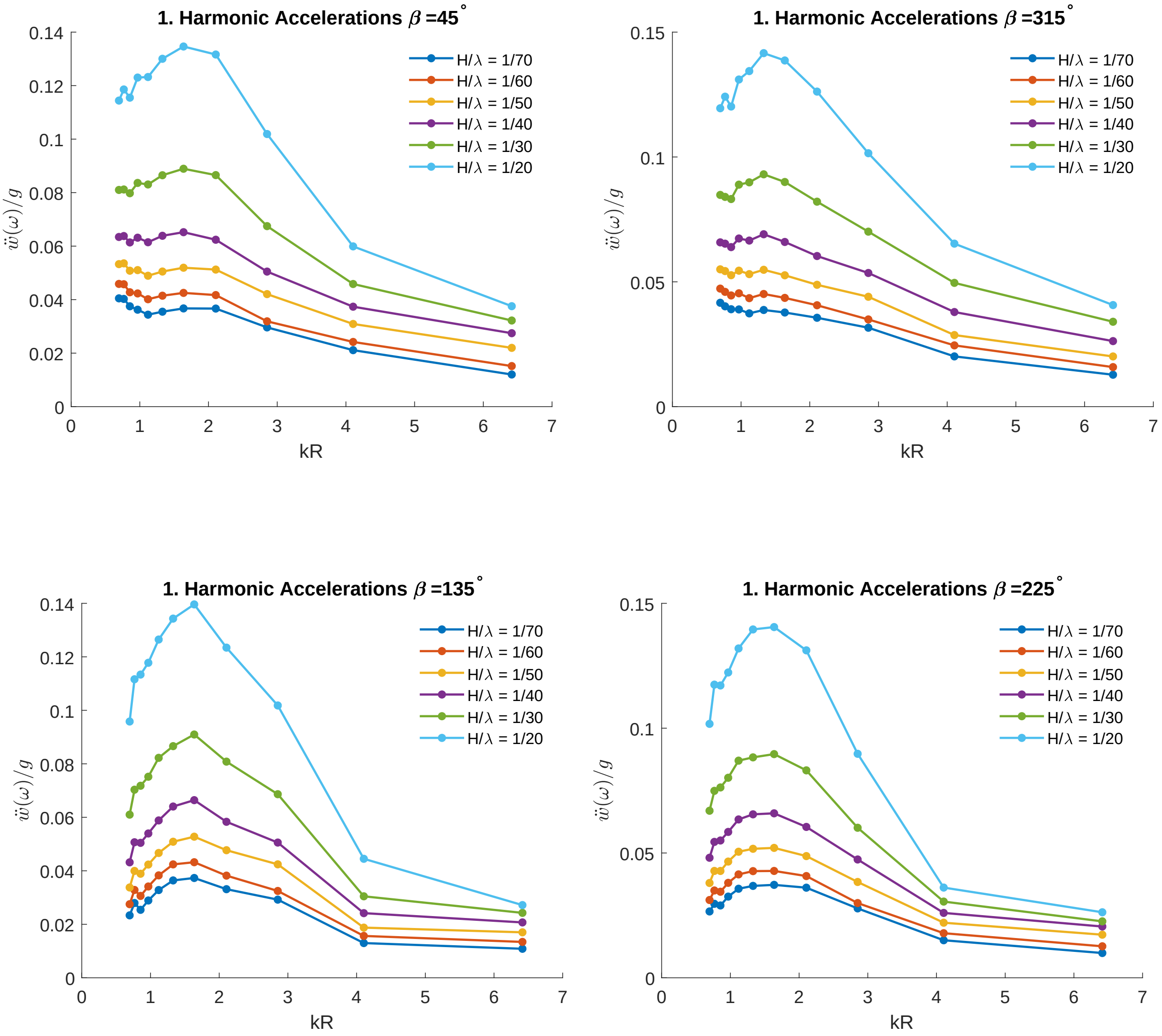

Figure G.6: Multi-torus: Experimental first harmonic accelerations at $\beta = 45^o$, $\beta = 315^o$, $\beta = 135^o$ and $\beta = 225^o$ in waves with steepness $H/\lambda = 1/70$, $H/\lambda = 1/60$, $H/\lambda = 1/50$, $H/\lambda = 1/40$, $H/\lambda = 1/30$, $H/\lambda = 1/20$.

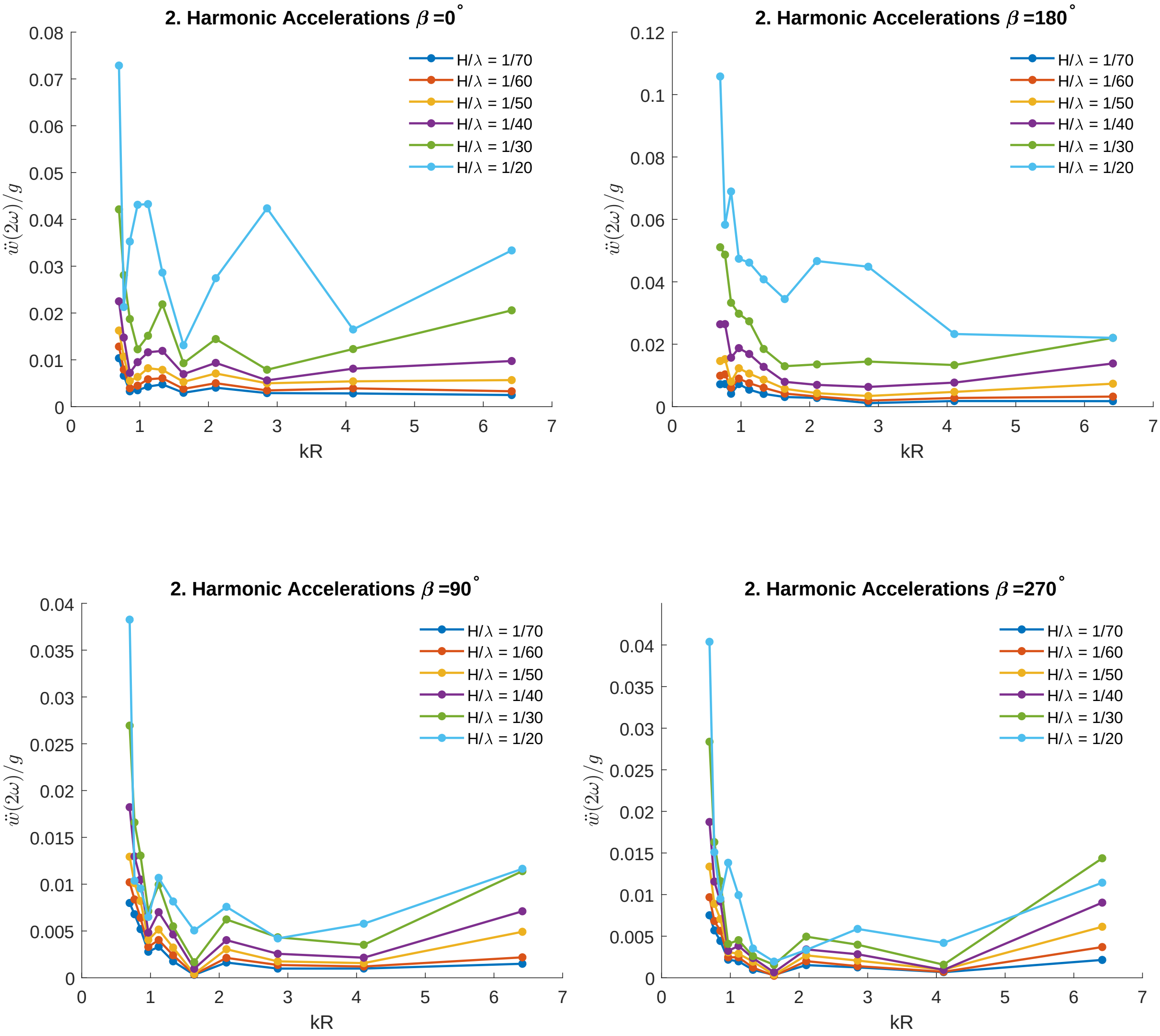

Figure G.7: Multi-torus: Experimental second harmonic accelerations at $\beta = 0^o$, $\beta = 180^o$, $\beta = 90^o$ and $\beta = 270^o$ in waves with steepness $H/\lambda = 1/70$, $H/\lambda = 1/60$, $H/\lambda = 1/50$, $H/\lambda = 1/40$, $H/\lambda = 1/30$, $H/\lambda = 1/20$.

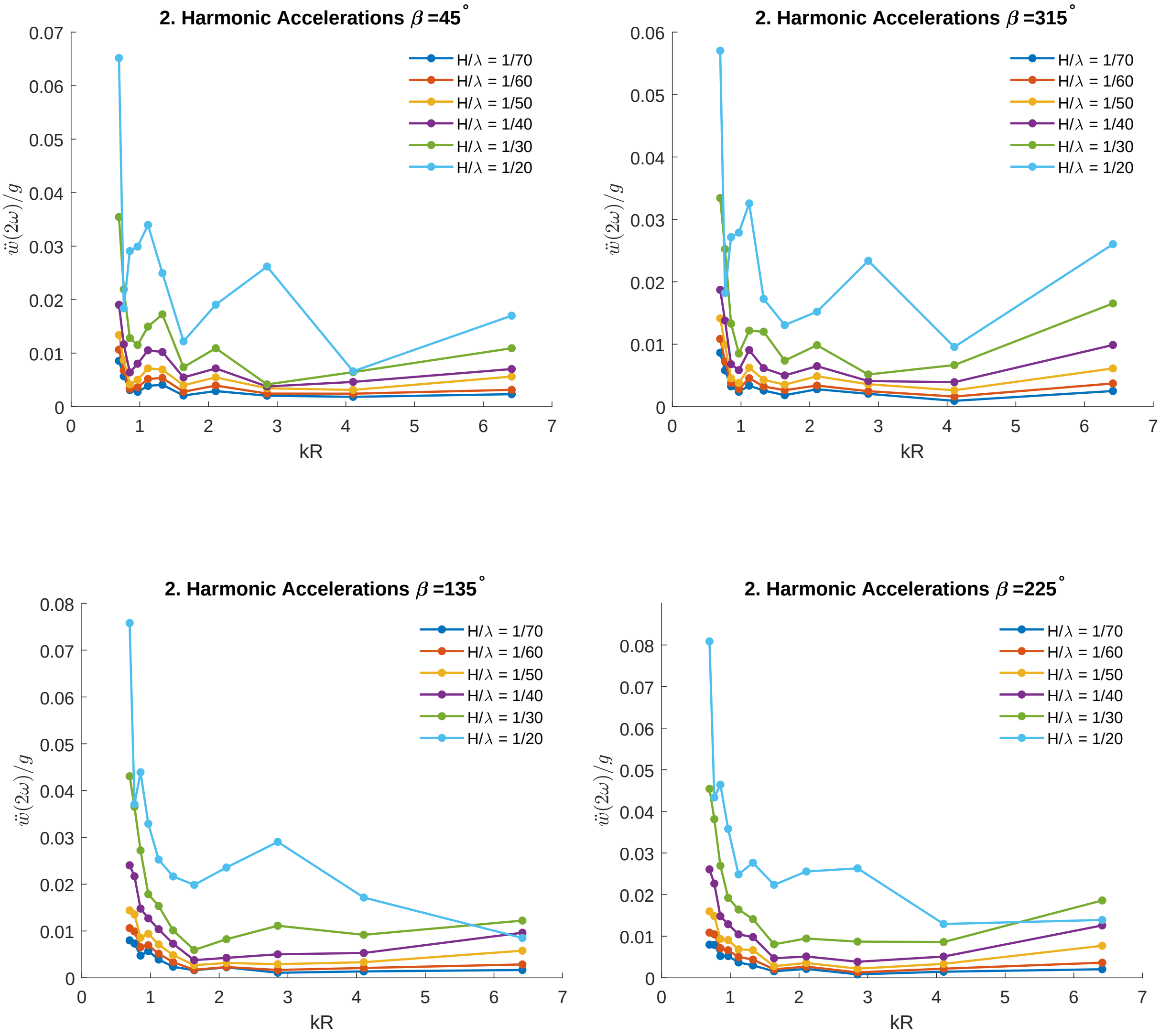

Figure G.8: Multi-torus: Experimental second harmonic accelerations at $\beta = 45^o$, $\beta = 315^o$, $\beta = 135^o$ and $\beta = 225^o$ in waves with steepness $H/\lambda = 1/70$, $H/\lambda = 1/60$, $H/\lambda = 1/50$, $H/\lambda = 1/40$, $H/\lambda = 1/30$, $H/\lambda = 1/20$.